MIRA AND CEPHEID VARIABLES AS EXTRAGALACTIC DISTANCE INDICATORS IN THE OPTICAL AND THE NEAR-INFRARED

A Dissertation

by

TARINI KONCHADY

Submitted to the Graduate and Professional School of
Texas A&M University
in partial fulfillment of the requirements for the degree of

DOCTOR OF PHILOSOPHY

Chair of Committee,	Lucas M. Macri
Committee Members,	Darren L. DePoy
	Jianhua Z. Huang
	Nicholas B. Suntzeff
Head of Department,	Grigory V. Rogachev

May 2022

Major Subject: Astronomy

ABSTRACT

Local measurements of the Hubble constant rely on extragalactic distance measurements, which are made using observations of Type Ia supernovae and certain variable stars. This dissertation focuses on two classes of variable star that are used to make distance measurements: Classical Cepheids and Mira variables.

The Legacy Survey of Space and Time (LSST), which will be conducted at the Vera C. Rubin Observatory, will return time-series data that have an ideal cadence for Mira studies. In anticipation of these data, we perform a search for Miras in the LSST photometric bands. We use archival optical and near-infrared observations of the galaxy M33 taken with the Canada-France-Hawaii Telescope's MegaCam and WIRCam instruments. We use machine learning classifiers to efficiently identify strong Mira candidates, which are visually confirmed. We also use period-luminosity relations for Miras in the Large Magellanic Cloud to identify Mira candidates in M33. We present the first empirical characterization of Miras in the LSST bands. We also recover approximately 70 percent of a sample of previously identified Miras and identify 2,916 new Mira candidates. For the first time, we find evidence for a first-overtone pulsation sequence in M33's Miras.

We also present H-band Milky Way Cepheid light curves extracted via difference imaging from observations taken with the United Kingdom InfraRed Telecope's Wide-Field Infrared Camera. The crowded nature of the Cepheid fields renders traditional photometric methods less effective, so we adapt and deploy a difference imaging pipeline originally written for data from the *Transiting Exoplanet Survey Satellite*. The light curves are used to derive corrections to "mean light" for random-phase *Hubble Space Telescope* observations. The phase corrections obtained from the H-band light curves are in good agreement with similar corrections obtained from VI light curves from the literature.

DEDICATION

To my family, who supported me unconditionally as I careened into places unfamiliar to all of us, and to the memory of Kalpana Chawla, who showed me it was possible for someone who looked like me to touch the stars.

ACKNOWLEDGMENTS

My first thanks is to my advisor, Lucas Macri. It feels like a very long time ago that you pulled my application out of the pile for the Texas A&M astronomy REU program, and I'll be forever grateful for it. Thank you for showing me how to be a better scientist (especially when it comes to an eye for detail) and supporting me as I realized I wanted to use my skills outside of academia.

I would not be getting this Ph.D. without the support of the department's graduate student community; from the bottom of my heart, thank you for keeping my spirits up and never letting me forget what I am capable of. To name a few names, thank you to Derek Anderson, Lauren Aldoroty, Sarah Cantu, Taylor Hutchison, Peter Ferguson, Jonathan Cohn, Katelyn Stringer, Dan Nagasawa, Alex Riley, Yaswant Devarakonda, Leo Alcorn, and Jessica O'Brien (honorary grad).

Thank you to Nicholas Suntzeff and Kim Vy-Tran for timely, fortifying conversations at a pivotal point of my Ph.D. I'm so appreciative that you believed I could go into science policy before I believed it myself. I also want to thank my counselors, Robert Carter and Pat Nation, for guiding and supporting me through the difficult, transitory phase that is graduate school.

A big thank you to the administrative staff of the Texas A&M Department of Physics and Astronomy and the Munnerlyn Instrumentation Lab for too many things to name, from helping me troubleshoot scantron grading to doing so much behind-the-scenes work when we hosted a site for the Conferences for Undergraduate Women in Physics.

And finally, Amma, Daddy, thank you for nurturing my dream of being an astronomer right from when I was in second standard. I'll always remember the astronomy books, the trips to the planetarium, and the earth-shattering talk about the Big Bang at the Indian Institute of Science (I was never more frustrated to have to go back to school the next day and learn about long division, when the universe was apparently so marvelous).

CONTRIBUTORS AND FUNDING SOURCES

Contributors

This work was supported by my dissertation committee consisting of my advisor, Professor Lucas Macri, and Professors Darren DePoy and Nicholas Suntzeff of the Department of Physics and Astronomy and Professor Jianhua Huang of the Department of Statistics.

The analysis done in Chapter 2 was led by the author (Tarini Konchady), with contributions from Professor Lucas Macri of the Department of Physics and Astronomy, and Xiaomeng Yan and Professor Jianhua Huang of the Department of Statistics. We thank Wenlong Yuan, Sarah Cantu, Caroline Huang, and Adam Riess for helpful feedback that improved this analysis. The author acknowledges the Texas A&M University Brazos High Performance Computing cluster that contributed to the research reported here.

The analysis done in Chapter 3 was led by the author (Tarini Konchady), with contributions from Professor Lucas Macri and Ryan Oelkers of the Department of Physics and Astronomy, David Jones, Wenlong Yuan, and Erik Peterson. We thank Adam Riess for helpful feedback that improved this analysis. The analysis was published in 2022 in an article listed in the Astrophysical Journal Supplement Series.

All other work conducted for the dissertation was completed independently by the author.

Funding Sources

Graduate study was supported by the Dr. Dionel Avilés '53 and Dr. James Johnson '67 Graduate Fellowship from Texas A&M University; the *Hubble Space Telescope* Observing Program 15879 that was supported by by NASA through a grant from the Space Telescope Science Institute, which is operated by the Association of Universities for Research in Astronomy, Inc., under NASA contract NAS 5–26555; and the Mitchell Institute for Fundamental Physics and Astronomy at Texas A&M University.

NOMENCLATURE

2MASS	Two-Micron All Sky Survey
2MASS PSC	2MASS Point Source Catalog
AGB	Asymptotic Giant Branch
CMB	Cosmic Microwave Background
DEHVILS	Dark Energy, H_0, and peculiar Velocities using Infrared Light from Supernovae
DIA	Difference Imaging Analysis
FFI	Full-Frame Image
HST	*Hubble Space Telescope*
IRAF	Image Reduction and Analysis Facility
ΛCDM	Lambda Cold Dark Matter
MW	Milky Way
Mpc	One megaparsec, or one million parsecs
Myr	One million years
NIR	Near-infrared
OGLE	Optical Gravitational Lensing Experiment
PLR	Period-Luminosity Relation
PSF	Point Spread Function
TESS	*Transiting Exoplanet Survey Satellite*
TIC	TESS Input Catalog
UKIRT	United Kingdom Infrared Telescope
WCS	World Coordinate System
WFCAM	Wide-Field Infrared Camera

TABLE OF CONTENTS

Page

LIST OF FIGURES

FIGURE Page

LIST OF TABLES

TABLE Page

1. INTRODUCTION

In 1922, Alexander Friedmann published an interpretation of Albert Einstein's theory of General Relativity that allowed for a dynamic universe (Friedmann, 1922). By assuming a low density of stars and omitting the cosmological constant Einstein inserted to keep the universe static, Friedmann came up with a universe that could expand indefinitely. But with his death in 1925, Friendmann could not promote his controversial (at the time) idea. Fortunately, the idea still wove its way through the scientific community (Trimble, 2013). For instance, Georges Lemaître independently arrived at the same idea of an expanding universe a few years after Friedmann's death. However, Lemaître went a step further than Friedmann and hypothesized that the universe began with the fracturing of a "primeval atom," which contained all the contents of the universe (Lemaître, 1927). This was the broad outline of what we now call the Big Bang theory. Like Friedmann, Lemaître was initially decried by most of his contemporaries, with Einstein telling Lemaître , "Your calculations are correct, but your physics is abominable" (Singh, 2004).

But the idea of an expanding universe began to be supported by a variety of astronomical observations. The most famous of these observations include the galaxy distances and apparent recessional velocities measured by Vesto Slipher, Edwin Hubble and Milton Humason at Mount Wilson Observatory (Hubble, 1929; Hubble and Humason, 1931). Some of the vital galaxy distances were derived using variable stars called Cepheids, which have a relation between their brightness and variability period that was first recorded by Henrietta Swan Leavitt (Leavitt, 1908; Leavitt and Pickering, 1912).

Hubble noted that there was a definite linear relation between a galaxy's apparent recessional velocity (v; km s^{-1}) and its distance from the observer (d; Mpc), which could be written as

$$v \;=\; K \;\times\; d. \tag{1.1}$$

Nowadays, K has been changed to H_0 and it is referred to as the Hubble constant, while the equation is known as the Hubble-Lemaître law. H_0 is a keystone of cosmological models (Weinberg et al., 2013).

Curiously, local measurements of H_0 based on Type Ia supernovae and Classical Cepheid variable stars (Riess et al., 2021b) differ at the $5\sigma <$ level from expectations based on the Lambda Cold Dark Matter (ΛCDM) cosmological model, which are anchored by observations of the Cosmic Microwave Background (Planck Collaboration, 2020) and Baryon Acoustic Oscillations (Alam et al., 2021).

Understanding this significant discrepancy – known as the Hubble tension – involves more precisely characterizing the objects used to make local measurements of H_0. This stable of objects includes two types of variable stars: Classical Cepheids ("Cepehids") and Mira variables ("Miras"). Both types of star are known to follow period-luminosity relations (PLRs) at certain wavelengths, which allows us to reliably estimate their average magnitudes from the periods with which they vary in brightness. Miras and Cepheids are also extremely luminous, so in conjunction with their PLRs we can use these stars as extragalactic distance indicators.

Two ongoing astronomical endeavors have notable potential in expanding the reach of Cepheids and Miras: the European Space Agency's *Gaia* satellite (Gaia Collaboration et al., 2016), and the Legacy Survey of Space and Time (LSST), which will be carried out by the Vera C. Rubin Observatory (Rubin Observatory; Ivezić et al. 2019) over the current decade.

Gaia is the successor of the *Hipparcos* satellite, which provided parallax measurements for $> 100,000$ stars at the milliarcsecond (mas) level (ESA, 1997). As of its early third data release, *Gaia* has returned 5-parameter astrometric solutions – positions, proper motions, and parallaxes – for nearly 1.5 billion objects in the Milky Way (MW) and the Magellanic Clouds, with uncertainties within $0.01 - 0.02$ mas for $G < 15$ mags (Gaia Collaboration et al., 2021). With expected Cepheid parallaxes pushing down to the microarcsecond level, *Gaia* can enable us to calibrate the Cepheid-based Extragalactic Distance Scale to within

$\sim 1\%$.

However, *Gaia* parallaxes alone cannot complete this calibration; *Hubble Space Telescope* (HST) observations of Cepheids with *Gaia* parallaxes are also required (Riess et al., 2018b, 2021a). This is because the Cepheid-based distance scale is based on HST observations of extragalactic Cepheids. Observations of MW Cepheids in the same HST bands will circumvent the systematic uncertainty that would arise from using observations in different bands to incorporate the *Gaia* parallaxes into the Extragalactic Distance Scale. Additionally, intermediate *Gaia* data products require parallax offsets that depend on magnitude, color, and ecliptic latitude (Lindegren et al., 2018, 2021a,b). So, HST observations of MW Cepheids with *Gaia* parallaxes could be used to both calibrate the Extragalactic Distance Scale and determine the relevant parallax offsets.

Now to Rubin Observatory: with its sensitive, wide field-of-view, it is capable of performing faint, high cadence time-domain surveys across large swathes of the sky. The decade-long LSST will cover $18,000$ deg^2 of the southern sky in the *ugrizy* bands, reaching between $22.1-25.0$ mags for stationary sources in single exposures. The ten-year coadds are expected to reach $24.9-27.5$ mags for similar sources, and each survey region will be visited ~ 800 times (Ivezić et al., 2019).

LSST will contain a treasure trove of faint, time-series data, ideal for studying extragalactic Miras. Yuan (2017) transformed PLRs of Large Magellanic Cloud (LMC) Miras (*VI* to *griz*) to demonstrate that Rubin Observatory would be able to recover ∼200,000 Miras across roughly 200 galaxies within 15 megaparsecs (Mpc). Approximately 75 galaxies within 14 Mpc could yield upwards of 100 Miras apiece. However, to efficiently recover Miras in LSST data, we need to empirically characterize Miras in the Rubin Observatory filters.

This dissertation focuses on developing techniques to better identify and characterize Miras and Cepheids for use as distance indicators, a critical task as we move through the domains of *Gaia* and Rubin Observatory.

1.1 Classical Cepheid Variables

Classical Cepheids ("Cepheids") are radially pulsating variable stars that occupy part of the "instability strip" on the Hertzsprung-Russell diagram, where most pulsating variables reside. They are young, yellow, supergiant stars; their high mass progenitors ($> 4M_{\odot}$; Turner, 1996, 2012) and young ages ($20 - 150$ Myr; Bono et al., 2005) make Cepheids fairly rare. Cepheids have periods ranging from $\sim 1 - 100$ days and tend to pulsate in the fundamental and first overtone modes (Percy, 2007; Soszyński et al., 2008, 2011a). The archetypal Cepheid is δ Cephei, which was identified by John Goodricke in October 1784 (Goodricke, 1786). However, the first identification of a Cepheid was made a month earlier by Edward Pigott, who observed the variability of η Aquilae (Percy, 1984).

Cepheid light curves have a signature sawtooth shape that is nearly identical from cycle to cycle, though Cepheids with different periods have slightly different light curve shapes. This change in light curve shape with period is known as the Hertzsprung progression (Hertzsprung, 1926). Cepheid amplitudes range from $\sim 0.5 - 1$ mag in the optical (Percy, 2007; Klagyivik and Szabados, 2009) and $\sim 0.1 - 0.3$ mag in the infrared (Monson and Pierce, 2011) and show weak but not significant dependence on metallicity (Majaess et al., 2013; Szabados and Klagyivik, 2012; Mancino et al., 2021).

Cepheid variability is driven by the κ-mechanism, since opacity, represented by κ, is key to this process. The κ-mechanism arises due to "partial ionization zones," which are regions within a star where a significant fraction of the material is ionized. Opacity typically scales with density (ρ) and temperature (T) as $\rho/T^{3.5}$. However, when a partial ionization zone is compressed, energy goes not just into heating the zone, but also into ionizing more material. So, the inverse effect of temperature on opacity is decreased (Zhevakin, 1959a,c,b; Baker and Kippenhahn, 1961; Baker, 1963). This results in an increase in opacity, which in turn leads to increased absorption of radiation and consequent heating and expansion. As the star expands and the partial ionization zone becomes less dense, it also becomes less opaque as the recently ionized material recombines. This allows the star to cool and contract. Typical

partial ionization zones which drive variablity are based in hydrogen (H I → H II) and helium (He I → He II).

The existence of partial ionization zones does not guarantee pulsation. In hot, blue stars, the zone can be too close to the surface of the star to have sufficient mass above to drive the pulsations. In cool, red stars, convection can dilute the effect of the partial ionization zone.

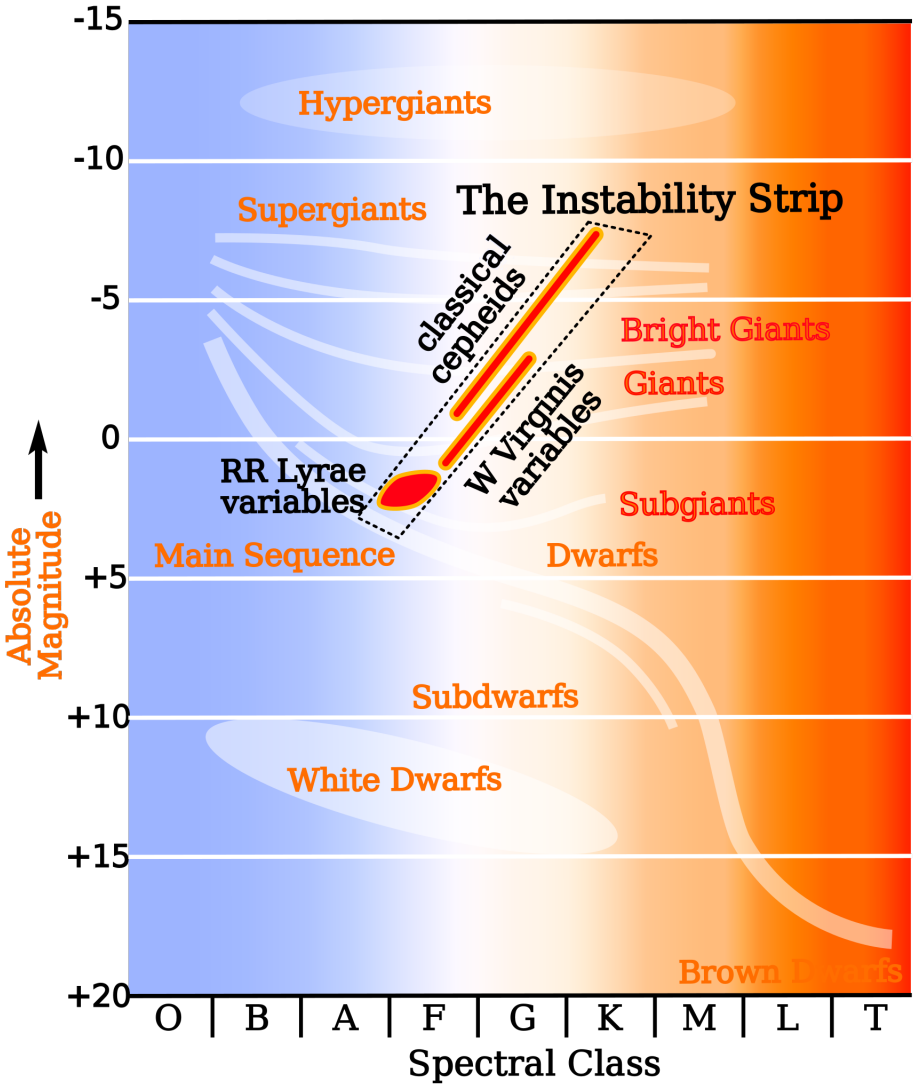

Figure 1.1 A Hertzsprung-Russell diagram highlighting different stages of stellar evolution along with the regions occupied by different classes of variable stars. The instability strip is also shown. Reprinted with appropriate citation from Rursus (https://commons.wikimedia.org/wiki/File:HR-diag-instability-strip.svg).

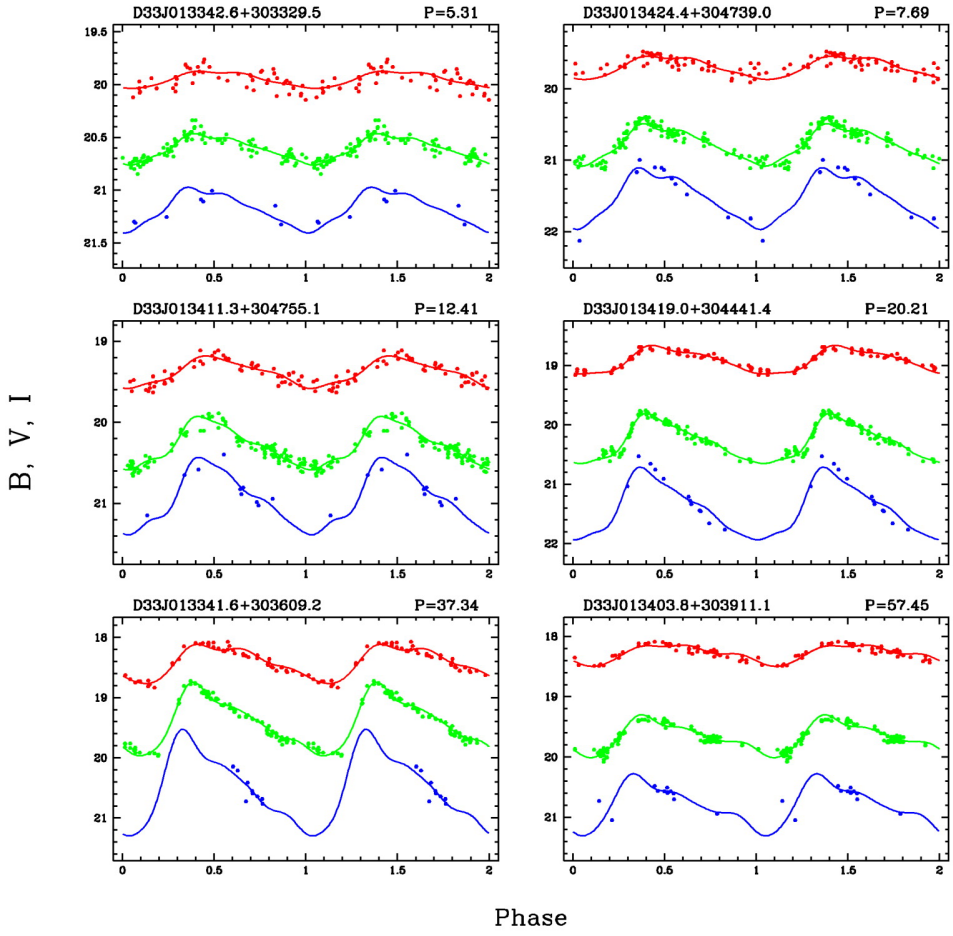

Figure 1.2 Light curves of six Cepheid variables identified in M33, with periods ranging from 5.31 to 57.45 days. The B-, V-, and I-band data are represented by the blue, green, and red circles respectively, while the best fit models are shown by the solid lines. The subtle change in light curve shape with period, known as the Hertzsprung progression (Hertzsprung, 1926), can be seen. Reprinted from Lucas M. Macri et al. (2001), *The Astronomical Journal* **121** 870. doi:10.1086/318773. ©AAS. Reproduced with permission.

These two limitations delineate the "blue edge" and "red edge" respectively of the instability strip (Carroll and Ostlie, 1996; Percy, 2007). The location of the red edge depends on a variety of factors relating to internal stellar processes, while the blue edge shows some dependence on metallicity (Bono et al., 1999).

For over a hundred years, Cepheids have been known to follow PLRs (Leavitt, 1908; Leavitt and Pickering, 1912). This property has made Cepheids crucial for establishing the

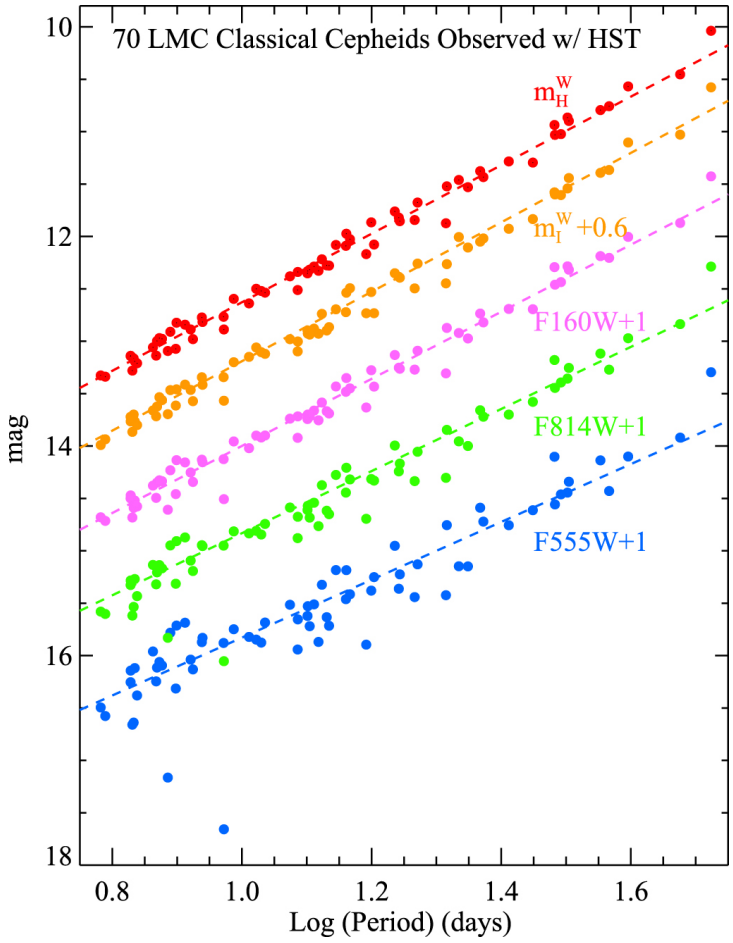

Figure 1.3 Period-luminosity relations of 70 Classical Cepheids in the Large Magellanic Cloud observed by the *Hubble Space Telescope*. From top to bottom, the bands/indices and their offsets are: the Wesenheit index m_H^W; the Wesenheit index $m_H^W + 0.6$; $F160W + 1$; $F814W + 1$; and $F555W + 1$. Reprinted with appropriate citation from Adam G. Riess et al. (2019), *The Astrophysical Journal* **876** 85.

Extragalactic Distance Scale and measuring H_0. NIR observations of Cepheids have proven especially useful as the intrinsic width of the PLR is only ~ 0.08 mag at those wavelengths (Persson et al., 2004; Macri et al., 2015; Riess et al., 2019, 2020), in addition to being less sensitive to dust and metallicity.

Cepheid-based measurements of H_0 have gained precision with time (Freedman et al., 2001; Riess et al., 2009, 2016, 2021b), increasing their discrepancy with early-universe measurements of H_0. The latest high precision measurement of H_0 based on Cepheids and Type

Ia supernovae ($H_0 = 73.04 \pm 1.04$ km s^{-1} Mpc^{-1}; Riess et al. 2021b) differs at the $5\sigma <$ level from expectations based on observations of the Cosmic Microwave Background and Baryon Acoustic Oscillations assuming ΛCDM ($H_0 = 67.4 \pm 0.5$ km s^{-1} Mpc^{-1}; Planck Collaboration 2020).

1.2 Mira Variables

Miras are Asymptotic Giant Branch (AGB) stars, whose variability is characterized by large amplitudes in the optical ($\Delta V > 2.5$ mag, $\Delta I > 0.8$ mag; Kholopov et al. 1985, Soszyński et al. 2009b) and long periods ($100 - 3000$ days; Riebel et al. 2010) with stochastic variations across variability cycles. They also vary in the infrared with smaller amplitudes than in the optical ($\Delta K_S > 0.4$ mag; Whitelock et al. 2008). With low mass progenitors ($0.8 - 8 M_\odot$, typically $3 M_\odot$; Whitelock 2013) Miras are relatively more common than Cepheids and can be found in all types of galaxies (Rejkuba, 2004; Whitelock, 2013; Boyer et al., 2017). The archetypal Mira, o Ceti, was identified as a variable star by David Fabricius in 1596, though it may also have been recorded as variable by ancient astronomers (Wilk, 1996; Hoffleit, 1997).

Like Cepheids, Miras are also pulsating variable stars, but the Mira pulsation mechanism is less understood. This is in no small part due to the dynamic phase of stellar evolution at which Miras occur: the Asymptotic Giant Branch (AGB) phase. The AGB phase occurs late in the life of low to intermediate mass stars ($\sim 0.8 - 10 M_\odot$) when they have ceased core helium burning.

To be very general, an AGB star would have an inert core of carbon and oxygen surrounded by a helium (He) burning shell, a hydrogen (H) burning shell, and a convective envelope of H and He. During the early-AGB phase, the star is offered waning support by the H burning shell as the outer layers of the star expand till H burning is extinguished. Then, the star contracts and the convective layer reaches deeper into the star till the He shell ignites in a He-flash to bring the star into the thermally-pulsing AGB (TP-AGB) phase.

During the TP-AGB phase, the now thicker He burning shell is convective almost all the

way to the bottom of the H burning shell, driven by the He burning. While the He burning shell accounts for the majority of the star's luminosity for a short time ($\sim 10^2$ years), it begins to burn less and less efficiently till convection ceases and the star expands to extinguish the H burning shell. The outer convective envelope reaches further into the star, transporting interior material to the surface. This process eventually ceases and the star contracts till the H burning shell reignites. The H burning shell is now the main source of energy for the star and serves in this role for much longer than the He shell did ($\sim 10^4 - 10^5$ years). This phase of H burning provides decreasing support till another He-flash occurs. The entire process forms

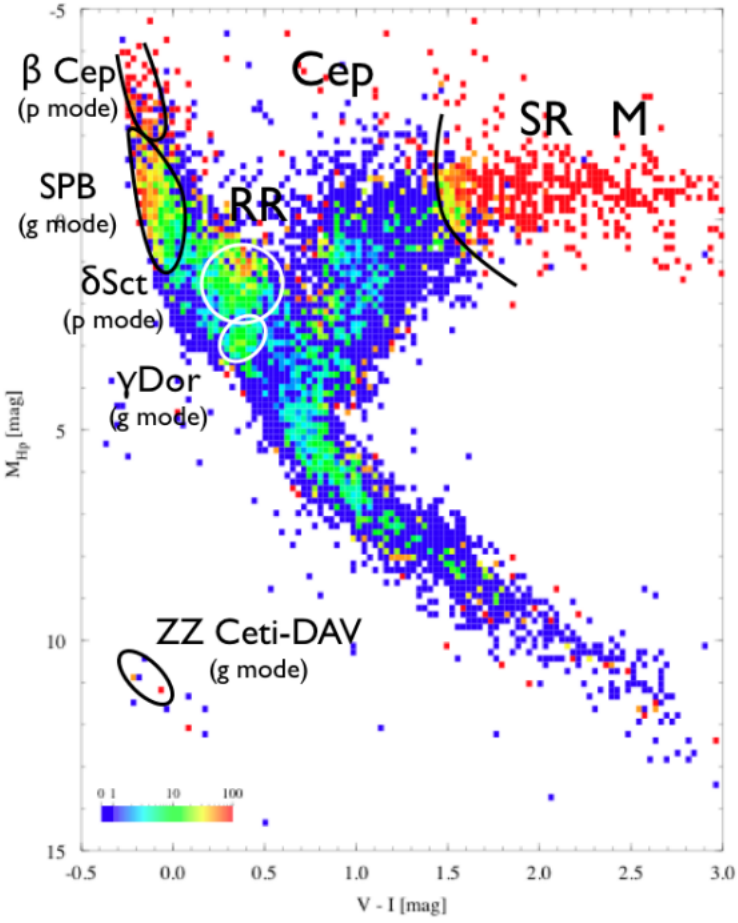

Figure 1.4 A Hertzsprung-Russell diagram constructed using data from the *Hipparcos* catalog. Miras ("M"), semi-regular variables ("SR"), and Classical Cepheids ("Cep") are highlighted. Reprinted with appropriate citation from Laurent Eyer and Nami Mowlavi (2008), *Journal of Physics Conference Series* **118** 012010.

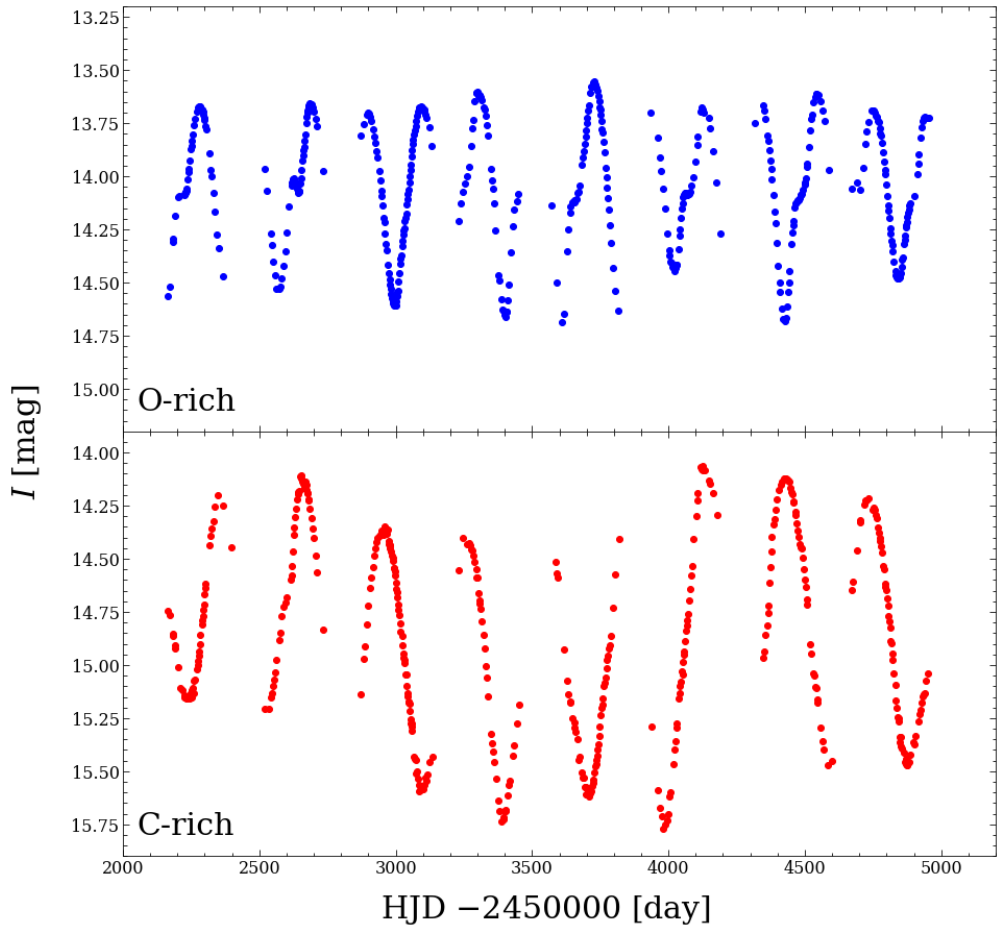

Figure 1.5 The light curves of an oxygen-rich Mira (OGLE-LMC-LPV-01752; upper panel) and a carbon-rich Mira (OGLE-LMC-LPV-02028; lower panel) located in the Large Magellanic Cloud. The y-axes of both plots span the same magnitude range (2 mags), showing the relatively larger amplitude of the carbon-rich Mira. The oxygen-rich Mira has a period of 205.8 days and the carbon-rich Mira has a period of 297.3 days. The measurements are reprinted from Soszyński et al. (2009a).

a thermal pulse, which is seen as a relatively sharp change in the star's luminosity. The star will experience multiple thermal pulses till the H burning shell is subsumed by convection or the star loses too much mass for shell burning to restart. Then, it will evolve to the white dwarf phase. The specific Mira pulsation mechanism is still an open question, but it likely depends on the convection and instability in the interiors of AGB stars. (Lattanzio, 2002; Karakas and Lattanzio, 2014; El Eid, 2016; Freytag et al., 2017; Xiong et al., 2018).

Pulsations in AGB stars can lift material from inner parts of the star to its outer layers,

where they condense into dust. The dust can absorb energy and gain enough momentum to stream away from the star, taking gas along with it. This process forms the signature mass loss of AGB stars (Höfner, 2008). The condensed dust is also partially responsible for why Miras appear to vary with large amplitudes in the optical: the dust preferentially absorbs at those wavelengths (Percy, 2007).

Miras generally pulsate radially in the fundamental mode, falling on the C sequence first presented in Wood et al. (1999) and expounded on since (Wood, 2000; Ita et al., 2004; Soszyński et al., 2004; Wood, 2015; Trabucchi et al., 2017). They may also fall on the C′ sequence, which can correspond to fundamental or first overtone pulsators or both (Trabucchi et al., 2017). Mass loss in AGB stars ($\dot{M} \gtrsim 10^{-8} M_{\odot}\mathrm{yr}^{-1}$) can cause them to transition between pulsation sequences, such as from the B sequence of first overtone pulsators to the C′ sequence (Trabucchi et al., 2017; McDonald and Trabucchi, 2019)).

Miras are typically classified as oxygen-rich (O-rich) or carbon-rich (C-rich) based on their surface chemistry, color, and light curves. The surface compositions of Miras are affected by the CNO cycle in the convective envelope, helium shell burning, and other internal stellar processes. ^{12}C and ^{18}O in particular can be "dredged up" and raised to the surface of the star (Iben and Renzini, 1983; Kobayashi et al., 2011; Karakas and Lattanzio, 2014). The occurrence of dredge-up events is dictated by stellar mass. In the case of stars with $M > 4\ M_{\odot}$, another phenomenon called "hot-bottom burning" (HBB) comes into play. During HBB, the bottom of the convective layer heats up to the point that the CNO cycle is activated with the rare appearance of the Na-Na and Mg-Al cycles. This can affect the transition from O-rich to C-rich for Miras, with some models allowing for C-rich Miras to be converted back to O-rich Miras (Frogel et al., 1980; Mould and Aaronson, 1980; Whitelock and Feast, 2000; Hinkle et al., 2016). The ratio of O-rich Miras to C-rich Miras shows some dependence on host galaxy metallicity, with galaxies of higher metallicity having larger ratios of O- to C-rich Miras (Cioni and Habing, 2003; Battinelli and Demers, 2004; Cioni et al., 2008; Battinelli and Demers, 2009; Hamren et al., 2015). C-rich Miras are redder

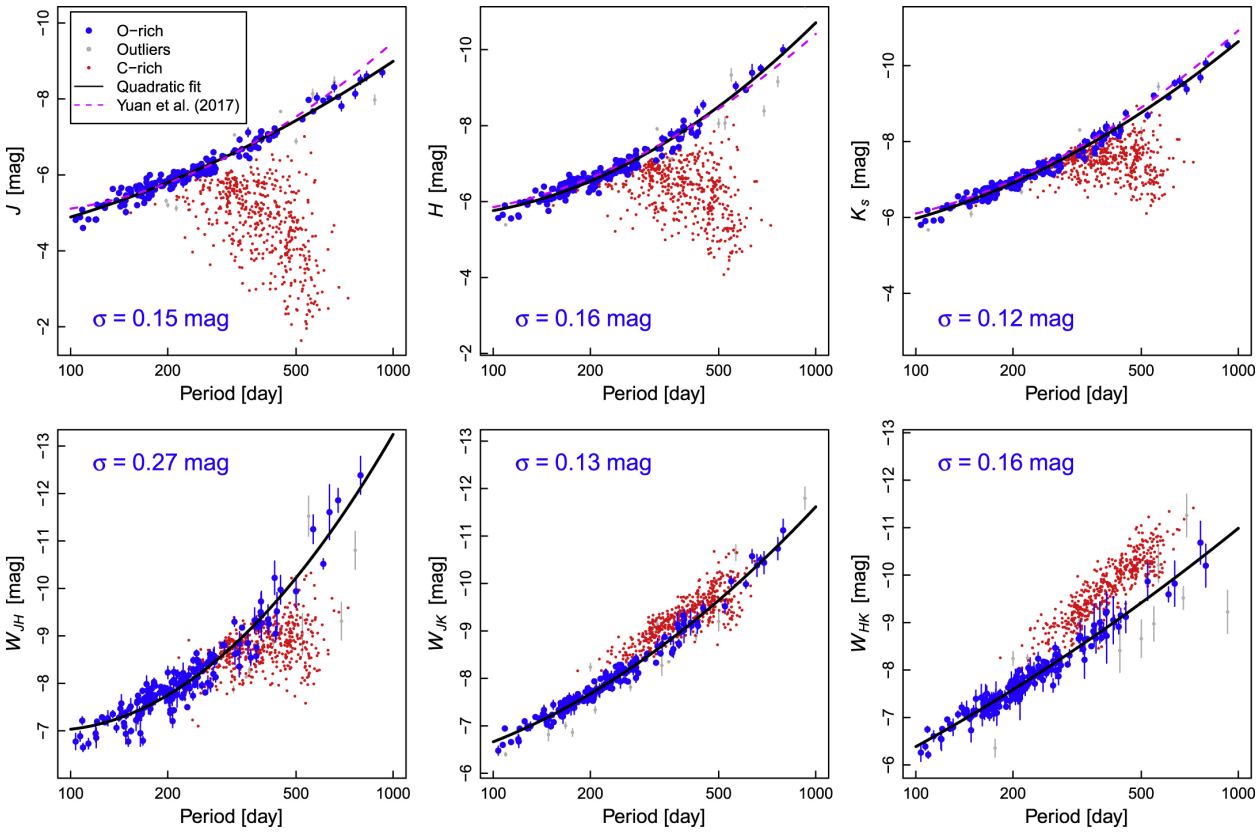

Figure 1.6 Period-luminosity (upper row) and period-Wesenheit (lower row) relations of Miras in the Large Magellanic Cloud (LMC). Oxygen-rich Miras are represented by filled blue circles and carbon-rich Miras are represented by red points. The oxygen-rich Miras are fit with quadratic relations. The solid black lines represent the relations fit using measurements from the LMC Near-infrared Synoptic Survey and the dashed magenta lines represent the relations fit using single-epoch 2MASS measurements. Reprinted from Wenlong Yuan et al. (2017b), *The Astronomical Journal* **154** 149. doi:10.3847/1538-3881/aa86f1. ©AAS. Reproduced with permission.

($J - K_S < 1.3 - 2.2$) and have longer periods than O-rich Miras (Yuan et al., 2017b; Ita and Matsunaga, 2011); they also exhibit more pronounced long-term changes to their mean magnitudes (Soszyński et al., 2009b, 2011b, 2013).

O-rich Miras follow tight PLRs in the NIR (Glass and Evans, 1981; Robertson and Feast, 1981), though O-rich Miras with periods greater than 400 days are susceptible to HBB, which causes them to appear brighter than expected based on linear PLRs (Whitelock et al., 2003). In the LMC, O-rich Miras have K-band PLRs with low scatter ($\sigma = 0.12$; Yuan et al.

2017b) that is comparable to the scatter of Cepheid PLRs in the same band ($\sigma = 0.09$; Macri et al. 2015). The NIR PLRs of Miras give them utility as extragalactic distance indicators (Whitelock et al., 2013; Menzies et al., 2015; Yuan et al., 2017a,b; Menzies et al., 2019) that can be used to measure H_0.

Huang et al. (2018) used NIR HST observations to identify a sample of 139 O-rich Mira candidates in NGC 4258, which they coupled with LMC Miras to obtain a relative distance modulus that was consistent with Cepheid-based measurements. Huang et al. (2020) also used NIR HST observations to identify 115 O-rich Mira candidates in NGC 1559. They coupled this sample with the maser distance to NGC 4258 and its sample of Miras to obtain a distance modulus for NGC 1559. Huang et al. (2020) also presented a Mira-based determination of H_0 ($= 73.3 \pm 4.0$ km s^{-1} Mpc^{-1}) within 1σ of the contemporaneous Cepheid-based value from Riess et al. (2019).

1.3 Outline of Dissertation

The outline of this dissertation is as follows: Chapter 2 describes a search for Mira variables in M33 using optical and NIR observations, Chapter 3 discusses the use of a novel data set to precisely identify the pulsation phase of seven Milky Way Cepheids, and Chapter 4 summarizes the work presented in this dissertation.

Chapter 2 details the third work in the M33 Synoptic Stellar Survey series. We use $grizJHK_S$ images of M33 taken from archival surveys of the galaxy to search for a known sample of Miras identified in Yuan et al. (2017a) and to also identify fainter Mira candidates. Empirical measurements of Miras in the LSST bands are lacking, and this work is the first step towards addressing that need. We use machine learning classifiers to efficiently identify Mira candidates based on their light curves and light curve models. We recovered a majority of the Yuan et al. (2017a) Miras and identified 2,916 new Mira candidates. For the first time, we find evidence for a first-overtone pulsation sequence in the M33 Mira candidates.

Chapter 3 describes the use of a novel data set to determine the pulsation phase of Cepheids when they were observed by HST. We use H-band images taken by the Wide-Field

Infrared Camera on the United Kingdom InfraRed Telescope as part of the DEHVILS survey to obtain the light curves of seven Milky Way Cepheids. Due to the crowded nature of these fields caused by defocusing the Camera, we performed difference-imaging photometry by modifying a pipeline originally developed to analyze images from the *Transiting Exoplanet Survey Satellite*. We achieved a photometric precision in line with expectations from photon statistics and used the resulting Cepheid light curves to derive corrections to "mean light" for random-phase HST observations in *F160W*. We find good agreement with previous phase corrections based on VI light curves from the literature.

2. PROPERTIES OF M33 MIRAS IN THE OPTICAL AND THE NEAR-INFRARED

We present the results of a search for Mira variables in M33 using archival $grizJHK_S$ observations obtained with the Canada-France-Hawai'i Telescope. We use multiband information and machine learning techniques to identify Mira candidates in M33. We recover ∼1,300 Mira candidates from Yuan et al. (2017a) and identify 2,916 new ones. For the first time, we find evidence for a first-overtone pulsation sequence in the M33 Mira candidates. We use oxygen-rich, fundamental-mode Miras from the Large Magellanic Cloud and M33 to derive a preliminary distance modulus for the latter of $\mu_{M33} = 24.52 - 24.58 \pm 0.04$ mags.*

2.1 Motivation

Local measurements of H_0 (Riess et al., 2021c) are primarily based on using Cepheids and Type Ia supernovae as primary and secondary distance indicators respectively. Additional independent primary distance indicators can increase the number of secondary distance indicators or enable new distance ladders to better characterize the H_0 tension. Miras can serve as one of these primary distance indicators.

Rubin Observatory will soon begin the LSST, a decade-long deep time domain survey of ∼20,000 sq. deg. in the *ugrizY* bands (Ivezić et al., 2019). Yuan (2017) transformed LMC Mira PLRs (from VI to *griz*) to estimate that the LSST data should yield ∼200,000 Miras across roughly 200 galaxies within 15 Mpc, with approximately 75 of these galaxies yielding upwards of 100 Miras each. In light of this, detailed characterization of Mira properties in *griz* would benefit searches for Miras in LSST data.

M33 is an ideal galaxy for the purposes of characterizing Miras, with faint, time-series imaging of the galaxy readily available. Also, we already know of a Mira presence in M33. Yuan et al. (2017a) used I-band observations from Macri et al. (2001) and Pellerin and Macri

*This chapter is a pre-copyedited, author-produced version of an article that will be submitted to the Astronomical Journal.

(2011) to identify 1,847 Mira candidates in M33. Their study was extended in Yuan et al. (2018) with sparsely-sampled JHK_S light curves. They obtained NIR PLRs for O-rich Miras and a distance modulus for M33 of 24.80 ± 0.06 mags.

The rest of this chapter is organized as follows: Section 2.2 describes our observations and photometry, Section 2.3 lays out our procedure for identifying Mira candidates using NIR information, Section 2.4 describes our attempts to use machine learning methods and LMC long-period variables (LPVs) to identify new Mira candidates, and Section 3.5 provides a summary of this work.

2.2 Observations and Data Reduction

2.2.1 MegaCam and WIRCam Observations

We used archival pipeline-processed optical observations of M33 taken with the MegaCam instrument (Boulade et al., 2003) on the Canada-France-Hawai'i Telescope (CFHT) as part of a survey for variable objects (Hartman et al., 2006). The data were obtained using the gS, rS, iS, and zS filters[1] (hereafter *griz*) with a baseline of roughly two years (October 2003 to July 2005).

MegaCam is a wide-field (1 deg. on a side) optical imager consisting of 36 CCDs with a plate scale of 0.187 arcsec per pixel. Each frame is a mosaic image as a result of the CCD array (see Figure 2.1). We split each frame into one image per individual CCD and then sorted the images by band. Each image was visually inspected and any unusable ones were discarded. This yielded an average of 47, 31 45 and 2 epochs in *griz* respectively, for any given location.

We also used pipeline-processed NIR observations of M33 obtained with the Wide-field InfraRed Camera (WIRCam; Puget et al. 2004) on CFHT. The observations were taken as part of three different programs (PIs: Beaulieu, JK_S, 2006-07; Ngeow, H, 2015; Lee, H, 2017-18) and covered different areas within the central disk of M33. The approximate time baselines of each program were 1, 2.5 and 1 year(s), respectively.

[1] https://www.cfht.hawaii.edu/Instruments/Imaging/Megacam/specsinformation.html

WIRCam consists of four detectors with a combined field of view of 20.5 arcmin on a side and a plate scale of 0.3 arcsec per pixel (Puget et al. 2004). Each WIRCam frame is effectively a "data cube" comprised of four to five 10-second exposures of the field of view at the time of observation. Each exposure is a mosaic of four images, which correspond to the four chips. We combined the multiple 10-second exposures of a given chip within each frame and only carried out photometry on these composite images. This yielded an average of 9, 6 and 3 epochs in JHK_S, respectively, for locations imaged in a given band.

The cadence of the MegaCam and WIRCam observations are shown in Figure 2.2, while Figure 2.3 shows the cumulative distribution of detected sources as a function of the number of the epochs available for that band. As we will show later, our typical Mira candidates had 4, 13, 43, 1, 6, 5 and 2 observations in $grizJHK_S$, respectively.

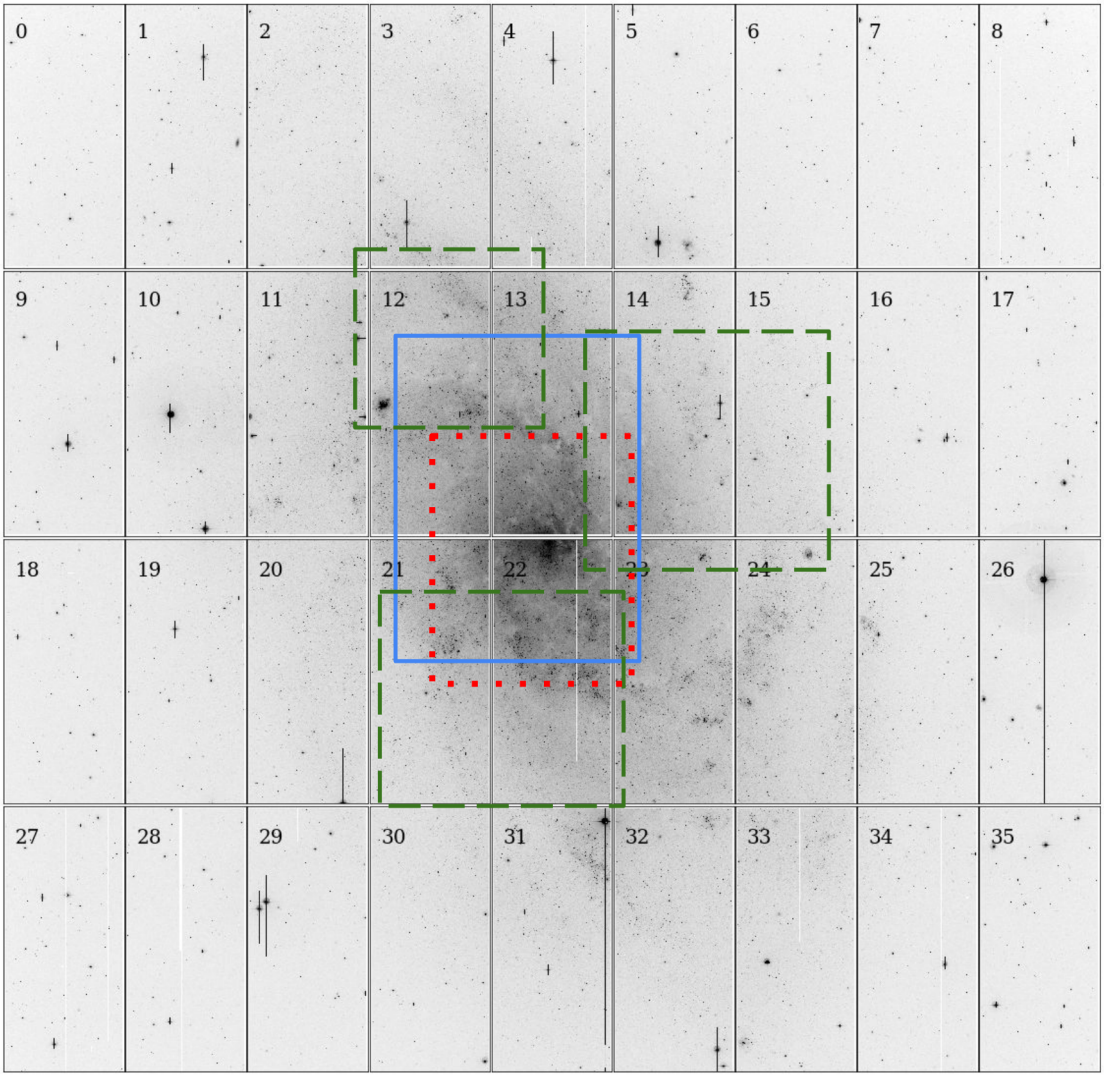

Figure 2.1 A representative mosaic of the CFHT MegaCam data with the CCD numbers marked. The mosaic is overlaid with the extents of the WIRCam J (blue, solid), H (green, dashed), and K_S (red, dotted) fields. North is up and east is to the left.

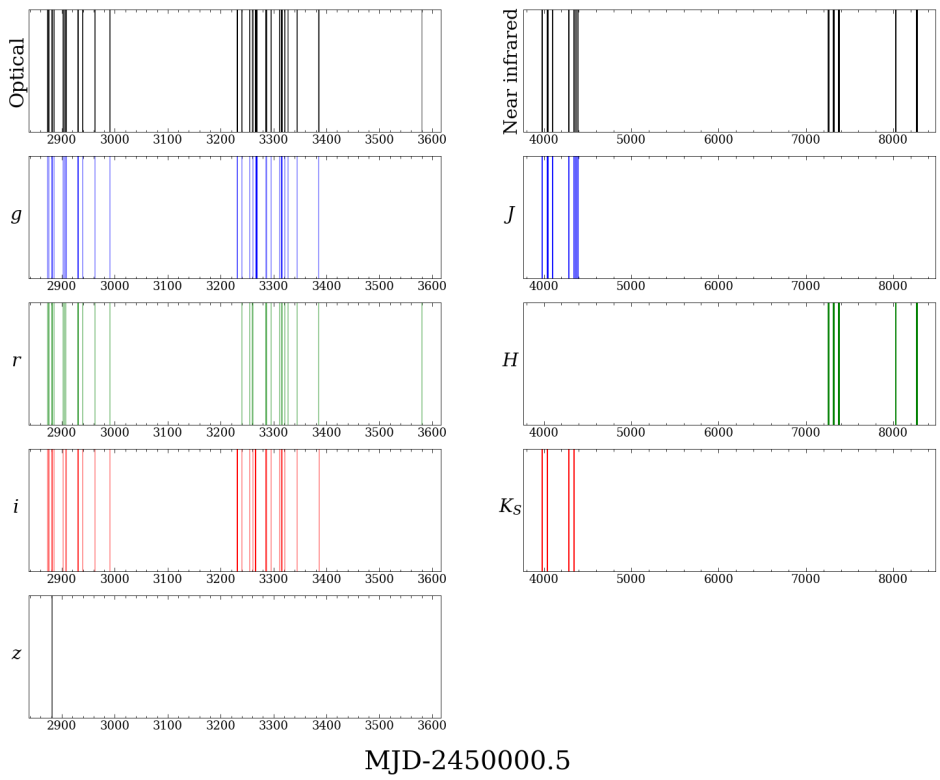

Figure 2.2 Cadence of observations across all optical bands (top left), all near-infrared bands (top right), *griz* (left, top to bottom), and JHK_S (right, top to bottom).

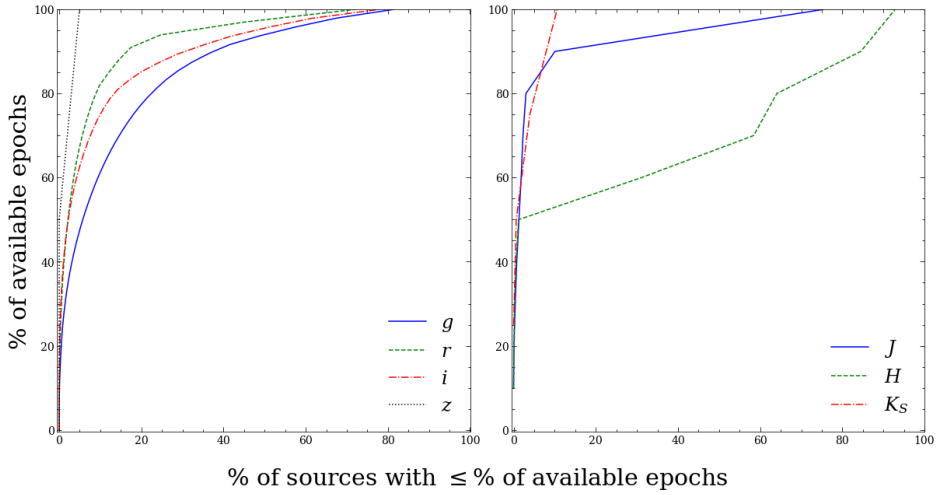

Figure 2.3 Availability of epochs for sources in *griz* (left), and JHK_S (right).

2.2.2 Photometry

To process the MegaCam images, we first identified a reference epoch for each band by examining the point-spread functions (PSFs) of stars in the images associated with CCD#11. We chose that detector because it partially covers the disk of M33 without overcrowding. None of the reference epochs had any unusable images.

We obtained aperture and PSF photometry for all images using `DAOPHOT`, `ALLSTAR`, `ALLFRAME` and related programs (Stetson, 1987, 1994) with a Python wrapper. A primary image for each CCD and band was constructed using `MONTAGE`. The primary images were then used to create source lists for `ALLFRAME`. `TRIAL` (Stetson, 1996) was used to perform frame-to-frame zeropoint corrections, calculate variability statistics, obtain mean instrumental magnitudes, and extract light curves. Sources were then matched across filters for each CCD. The photometric uncertainties versus magnitude for each band are shown in Figure 2.4.

We performed the astrometric and photometric calibration of the MegaCam sources using images from the Panoramic Survey Telescope and Rapid Response System (Pan-STARRS) Telescope #1 Data Release 1 (PS1 DR1; Chambers et al. 2016). We solved for the astrometric solution using `WCSTools` (Mink, 1999) with the primary image of each CCD and filter. Following this, we matched CFHT and PS1 DR1 sources with a tolerance of 2 arcsec. If multiple sources satisfied that criterion, the closest Pan-STARRS source was selected.

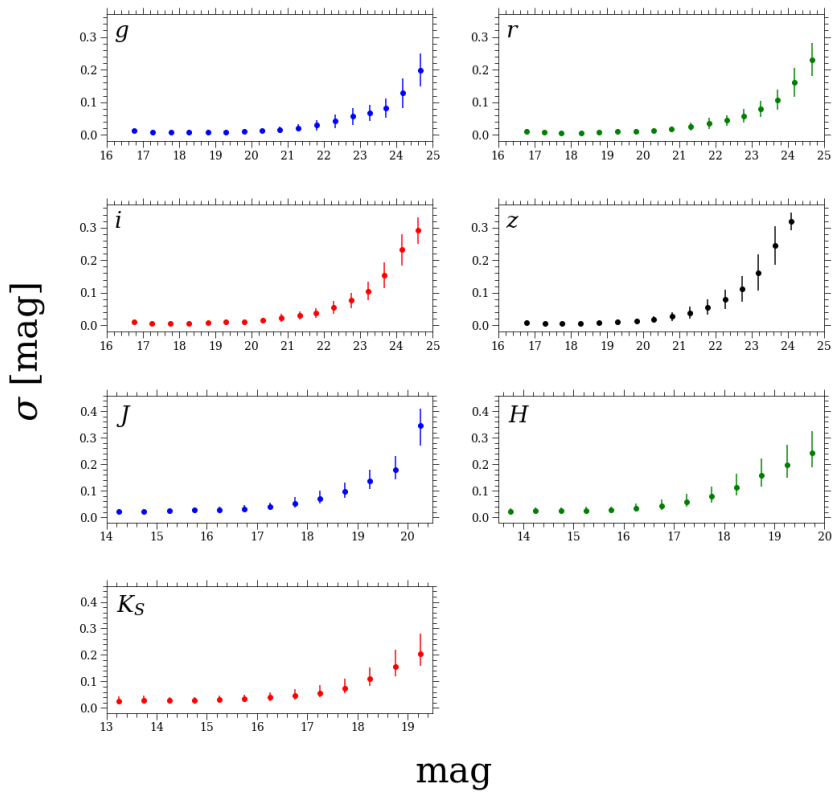

Figure 2.4 Photometric uncertainties as a function of magnitude, binned in 0.5 mag increments.

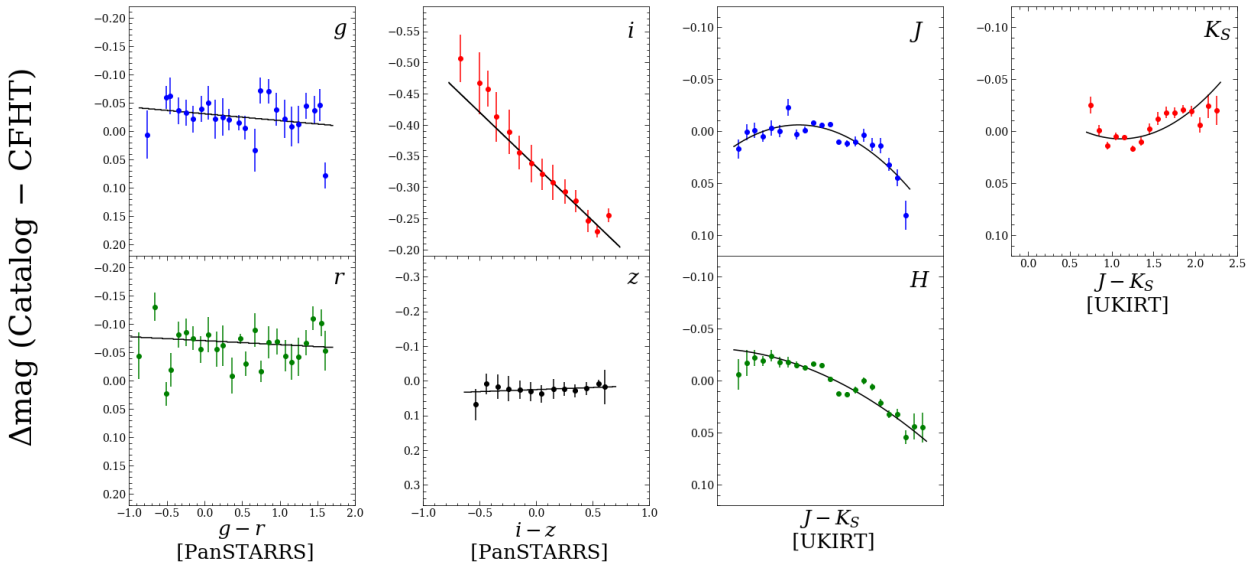

Figure 2.5 Typical photometric transformations in all bands used in this study, plotted in 0.1 mag increments. The lines represent the best-fit color terms.

Table 2.1. *griz* photometric transformations

Band	Color	χ	ξ	Pivot
g	$g-r$	-0.078 ± 0.001	0.012 ± 0.002	0.8
	$g-i$	-0.077 ± 0.001	0.006 ± 0.001	1.5
	$g-z$	-0.083 ± 0.001	0.005 ± 0.001	1.5
r	$g-r$	-0.010 ± 0.001	0.007 ± 0.002	0.8
	$r-i$	-0.007 ± 0.001	0.026 ± 0.002	0.8
	$r-z$	-0.012 ± 0.001	0.017 ± 0.002	1.0
i	$g-i$	-0.155 ± 0.001	0.023 ± 0.001	0.8
	$r-i$	-0.155 ± 0.001	0.051 ± 0.002	0.8
	$i-z$	-0.151 ± 0.001	0.174 ± 0.007	0.3
z	$g-z$	0.044 ± 0.001	0.011 ± 0.001	1.5
	$r-z$	0.041 ± 0.001	0.013 ± 0.002	1.0
	$i-z$	0.036 ± 0.001	-0.012 ± 0.006	0.3

We used our list of astrometrically-calibrated sources to solve the following photometric transformations, making iterative 2.5σ rejections:

$$m_C - m_I = \mathrm{ZP} + \chi + \xi(\mathrm{col} - \mathrm{piv}) \tag{2.1}$$

where m_C is the fully-calibrated PS1 magnitude, m_I is the instrumental magnitude reported by `DAOPHOT/ALLSTAR/ALLFRAME` (corrected for exposure time), ZP is the MegaCam default zeropoint for a given band[2], χ is the residual zeropoint, ξ is the color term, col is the PS1 color, and piv is a "pivot" color value typical of our target stars. We solved for chip-specific values of χ and a global value of ξ for a given transformation, using $\sim$150 stars per CCD and obtaining a typical scatter of 0.04 mag.

To process the WIRCam images, we first identified the fields associated with the various observing programs. There was no consistent overlap across all the frames and filters, as seen in Figure 2.1. So, before beginning photometry, we separated the images into groups

[2]https://www.cfht.hawaii.edu/Instruments/Imaging/MegaPrime/generalinformation.html

based on their location on the sky (4, 25 and 10 groups for JHK_S, respectively). Reference images for each group were chosen by visual inspection. We then obtained aperture and PSF photometry for the WIRCam images using the same method we did for the MegaCam images.

We performed the astrometric and photometric calibration of the WIRCam sources using the catalog from Javadi et al. (2015), based on observations with the UK InfraRed Telescope (UKIRT). We obtained WCS information from the WIRCam images to do preliminary position matching with the UKIRT catalog. After determining position residuals from this preliminary matching and applying the necessary offsets ($0.5 - 1.5$ arcsec depending on the band), quadratic/cubic-like trends were seen in the remaining WCS residuals based on pixel location. These are likely due to different geometrical distortions in the two cameras. These trends were fit and removed, leaving behind a final non-parametric trend in the position residuals. To correct this final trend, we divided each image in 100 pixel $\times$100 pixel cells and used the average residuals of the stars in each cell to fit a thin-plate spline and apply the necessary correction. This final correction resulted in a standard deviation of ~ 0.1 arcsec in the position residuals. All corrections done after the initial matching were based on the 5,000 brightest stars in a given image. We solved the following equation with iterative outlier cuts of 2.5σ to obtain the photometric transformations:

$$m_I - m_C \ = \chi \ + \xi(J - K_S - 1.0) \ + \xi^{'}(J - K_S - 1.0)^2 \tag{2.2}$$

where m_I is the instrumental magnitude, m_C is the calibrated UKIRT magnitude, χ is the residual zeropoint[3], ξ and $\xi^{'}$ are the first- and second-order color terms and $J - K_S$ is the UKIRT color. We solved for global parameters across the four detectors.

The mean values of all coefficients in the photometric transformations are presented in Tables 2.1 and 2.2, and representative solutions are shown in Figure 2.5.

[3]See link for official instrument zeropoints: https://www.cfht.hawaii.edu/Instruments/Imaging/WIRCam/WIRCamThroughput.html

Table 2.2. JHK_S photometric transformations

Band	χ	ξ	$\xi^{'}$	Measured Zeropoint
J	-0.032 ± 0.001	-0.016 ± 0.002	-0.035 ± 0.004	23.538 ± 0.012
H	-0.055 ± 0.001	-0.034 ± 0.002	-0.013 ± 0.003	23.685 ± 0.019
K_S	-0.059 ± 0.002	-0.008 ± 0.009	0.038 ± 0.009	22.942 ± 0.023

2.3 Identifying Preliminary Mira Candidates Using Optical and Near-Infrared Observations

We identified $\sim$ 1.15 million unique objects from our photometry, all of which had at least one detection in the i band. The Hess/color-magnitude diagrams for the optical and NIR bands are shown in Figures 2.6 and 2.7 respectively, with the recovered Miras from Yuan et al. (2017a) and Yuan et al. (2018) overplotted.

We began the selection of potential Mira candidates by making variability, color, and amplitude cuts based on the optical data. The variability cuts were based on the Stetson J index (Stetson, 1996) calculated from our i band measurements (J_i) as calculated by `TRIAL`. This index takes into account correlated deviations from a mean magnitude and their measurement quality; the higher its value, the more likely an object is genuinely variable. We excluded from further consideration all objects with $J_i < 0.75$ (see Figure 2.8 for the overall distribution of J_i and Figure 2.9 for J_i versus i for the entire sample). The J_i threshold was chosen because it retained the objects whose J_i values were at least 1σ greater than the mean J_i value of the entire sample. Since Miras are red, we only considered objects with either $r - i \geq 0$ or a non-detection in the r band. From the remaining objects, we selected those whose i-band light curves spanned a range (A_i) of at least 0.3 mag (see Figure 2.10 for the overall distribution of A_i for the entire sample).

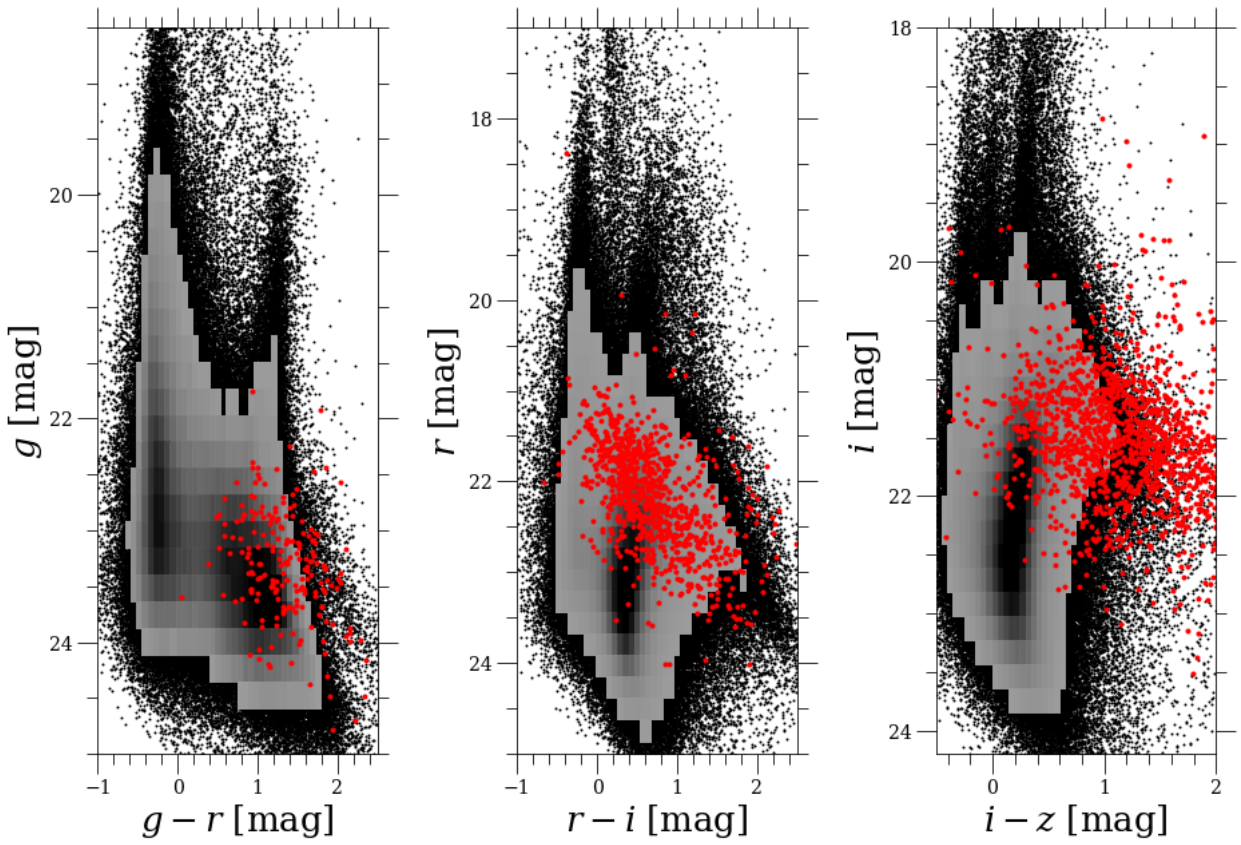

Figure 2.6 Color-magnitude/Hess diagrams for the optical bands, highlighthing the recovered Miras from Yuan et al. (2017a) (red points). The Hess diagram is used where the source density exceeds 200 objects per bin. Mira recovery varies across filters.

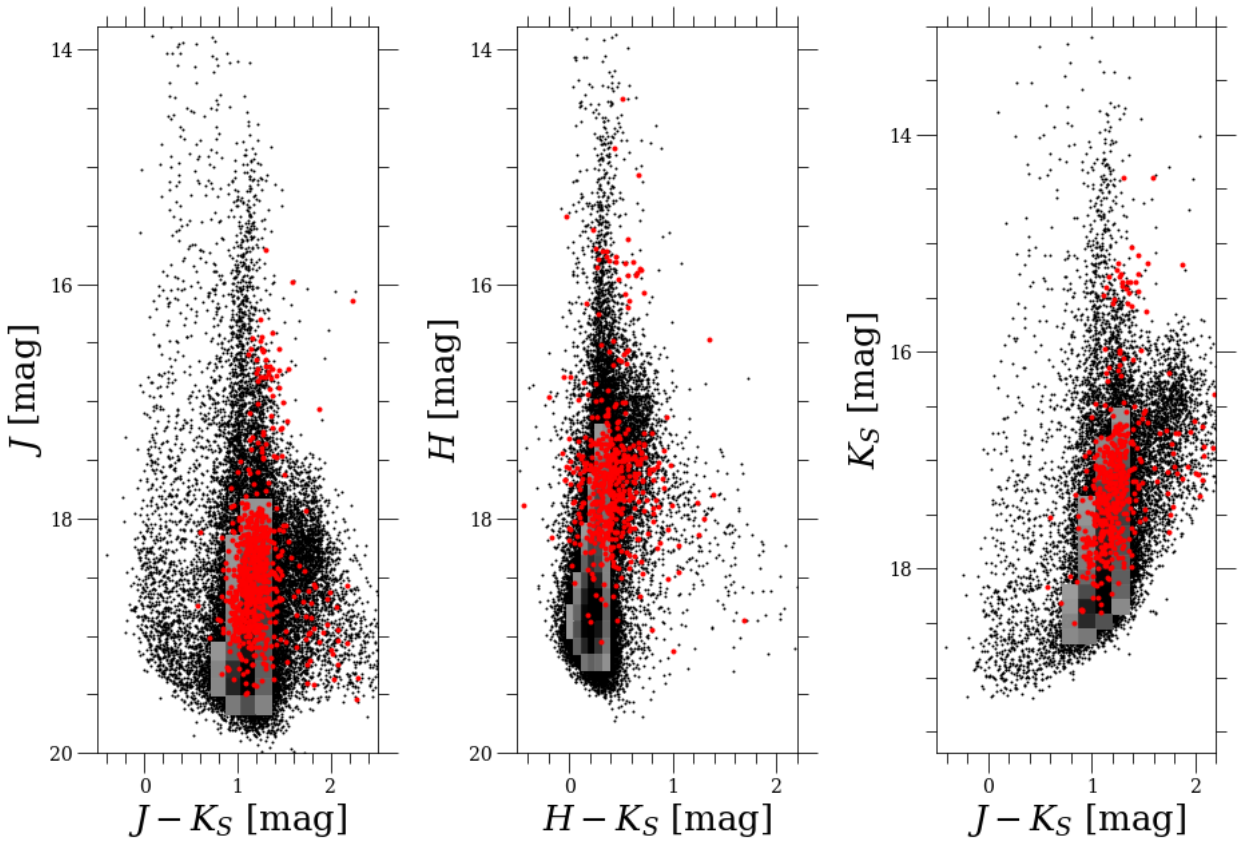

Figure 2.7 Same as Figure 2.6, but for the NIR bands.

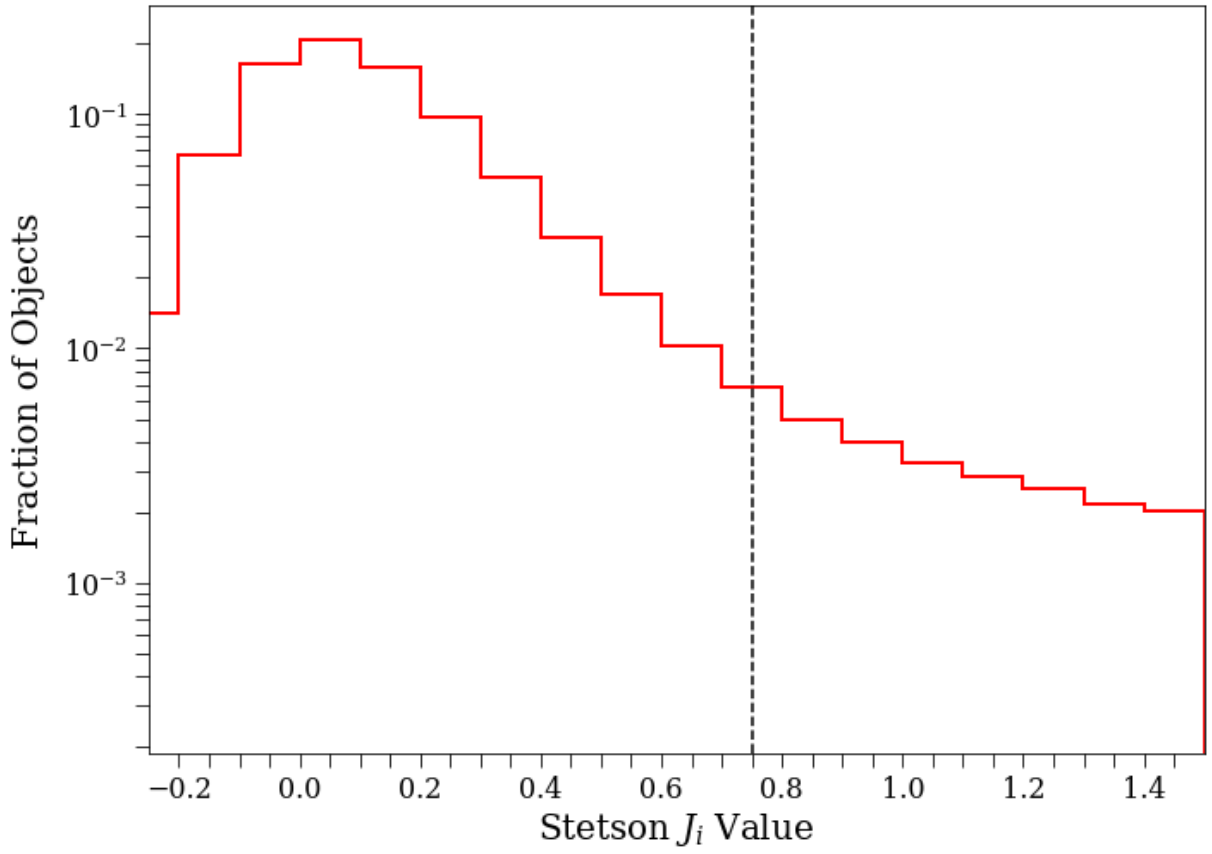

Figure 2.8 Histogram of Stetson J variability index for all detected sources in the i band. The vertical dashed line at $J_i = 0.75$ is the minimum threshold we assumed for Mira candidates.

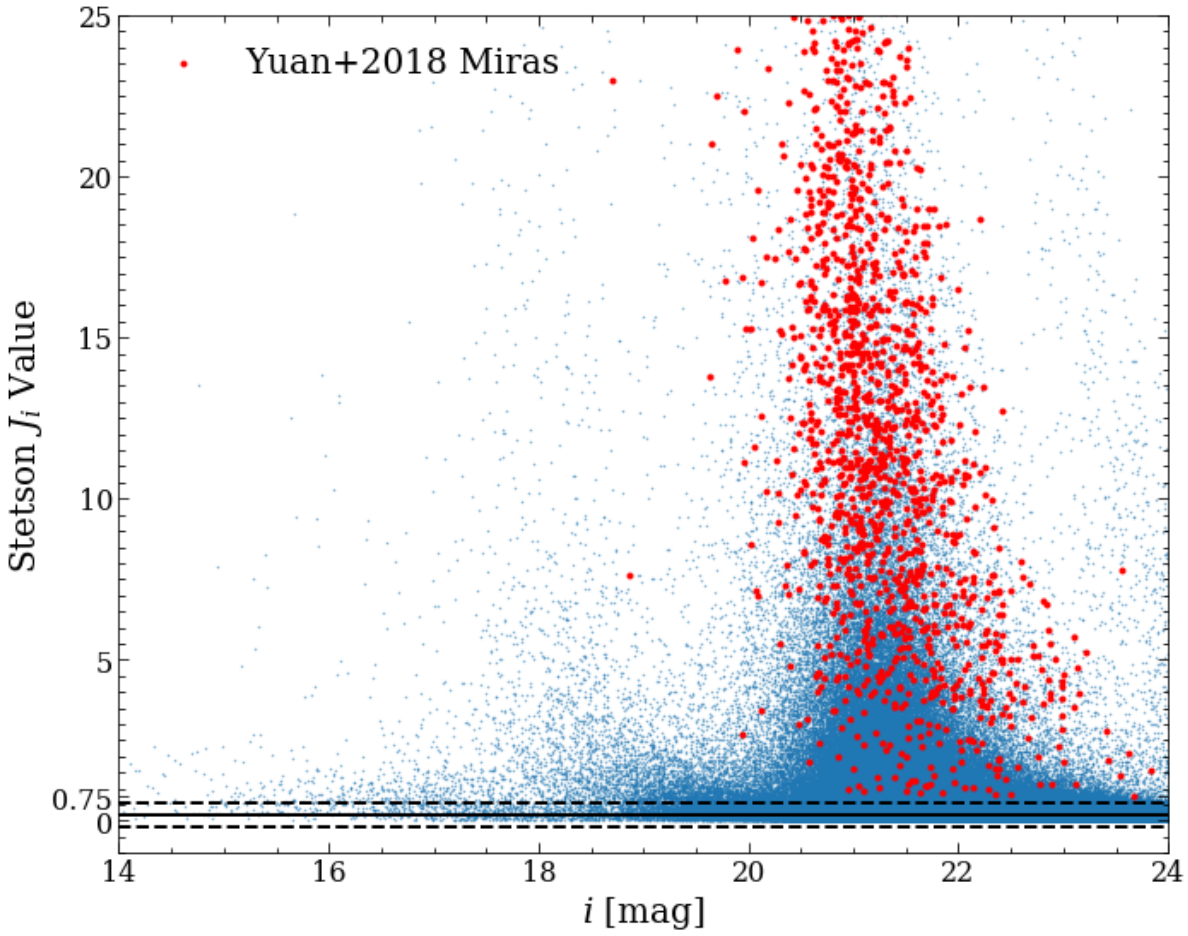

Figure 2.9 Values of J_i as a function of i magnitude for all detected sources. The horizontal solid line is the mean value after sigma clipping, with the dashed lines showing 1σ scatter. Our variability threshold of $J_i \geq 0.75$ is shown on the y axis, and Miras from Yuan et al. (2018) are overplotted in red.

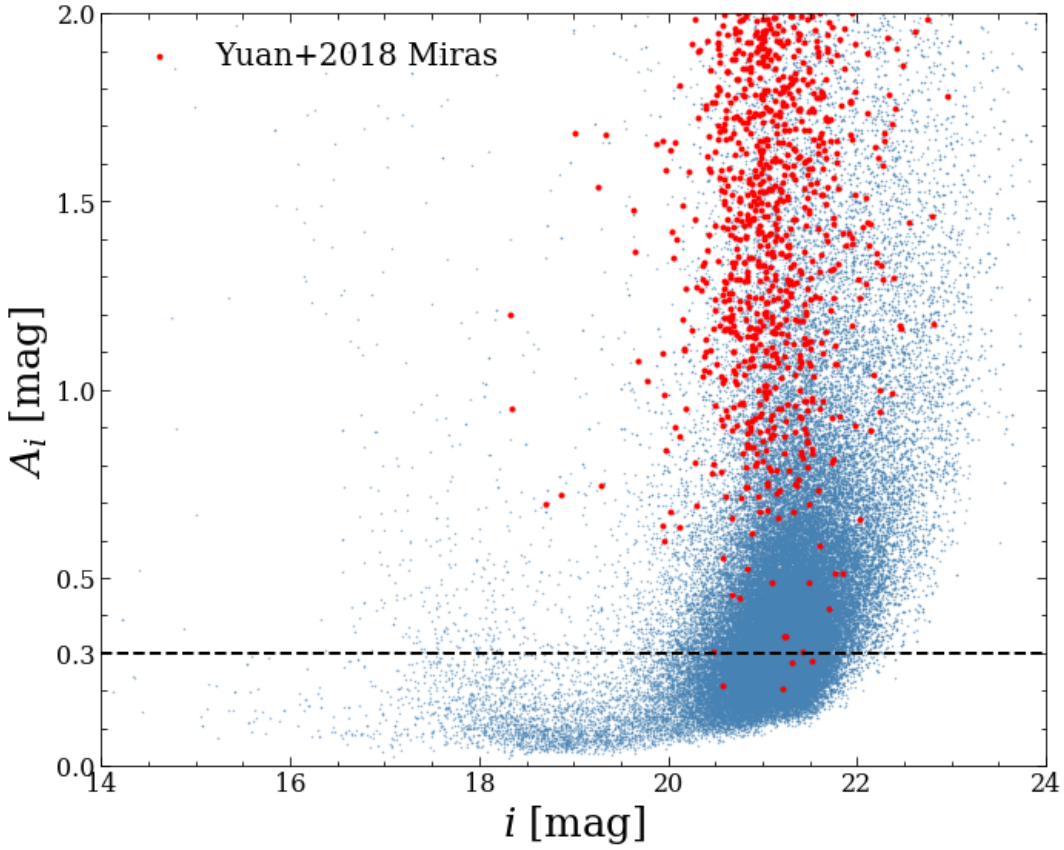

Figure 2.10 i-band light curve range (A_i) versus i magnitude for objects with: (i) $J_i \geq 0.75$, (ii) $r - i \geq 0$ or a non-detection in r , and (iii) a detection in any of the J, H, or K_S bands. The horizontal dashed line shows our amplitude threshold of $A_i \geq 0.3$. The Miras from Yuan et al. (2018) are overplotted in red.

We then selected the objects that were detected in at least one of the NIR bands, as that information is needed for our subsequent analysis. Following all the stated cuts (summarized in Table 2.3), we were left with ∼14,000 variables, which included ∼1,300 of the Miras characterized in Yuan et al. (2018).

We fit the $griJHK_S$ light curves of our ∼14,000 candidate objects using a simple sinusoidal model. Since the z measurements were obtained on a single night, they are not considered further in this analysis. We attempted to fit the light curves using a semi-parametric Gaussian Process model (Yuan et al., 2017a; He et al., 2016) and stochastic variational inference

Table 2.3. Selection of Mira candidates

Criterion	N remaining
1. Detected in i	1,150,000
2. $J_i \geq 0.75$	70,000
3. $r - i \geq 0$ or no r	60,000
4. $A_i \geq 0.3$ mag	40,000
5. Detected in NIR	14,000

models (He et al., 2021) that have recently been used on longer Mira time series. Unfortunately, the limited number of cycles covered by our data and the lack of time overlap between the optical and the NIR bands hampered the performance of these models.

The simpler sinusoidal model simultaneously fit all the light curves associated with a given object. The optical and NIR light curves were assumed to share a common period but the NIR bands were allowed to have a common phase offset with respect to the optical bands. The NIR bands were fit with a common amplitude while the g-, r-, and i-band light curves were assumed to have independent amplitudes. The model for a single band is defined by:

$$m(t_i) \;=\; \overline{m} \;-\; A\sin(\frac{2\pi}{P}t_i + \phi) \tag{2.3}$$

where m is the magnitude at some time t_i, $\overline{m}$ is the mean magnitude, A is the amplitude, P is the period, and ϕ is the phase. Figure 2.11 shows the light curves and best-fit model for one of the recovered Miras. Figure 2.12 compares the periods of the Miras identified in Yuan et al. (2017a) that were recovered in this work. Period uncertainties could not be estimated for all variables, but recovered variables whose periods were within 50 days of their Yuan et al. (2017a) values had a mean $\frac{\sigma(P)}{P}$ value of 0.03.

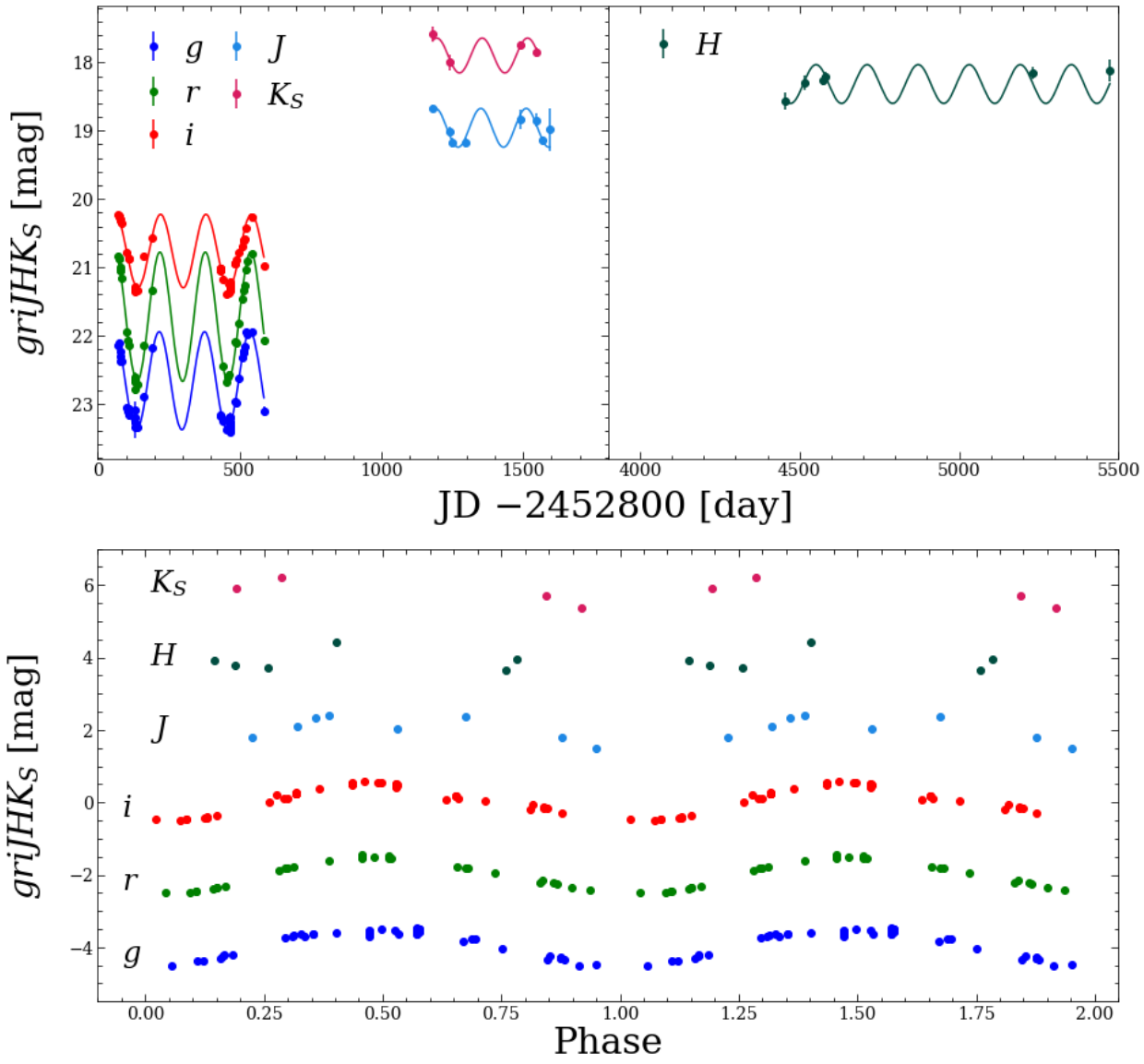

Figure 2.11 A representative Mira from our sample that was previously identified in Yuan et al. (2017a) and further characterized in Yuan et al. (2018). The upper panels show the observed light curves in $griJHK_S$ and the lower panel shows the phased light curves with offsets.

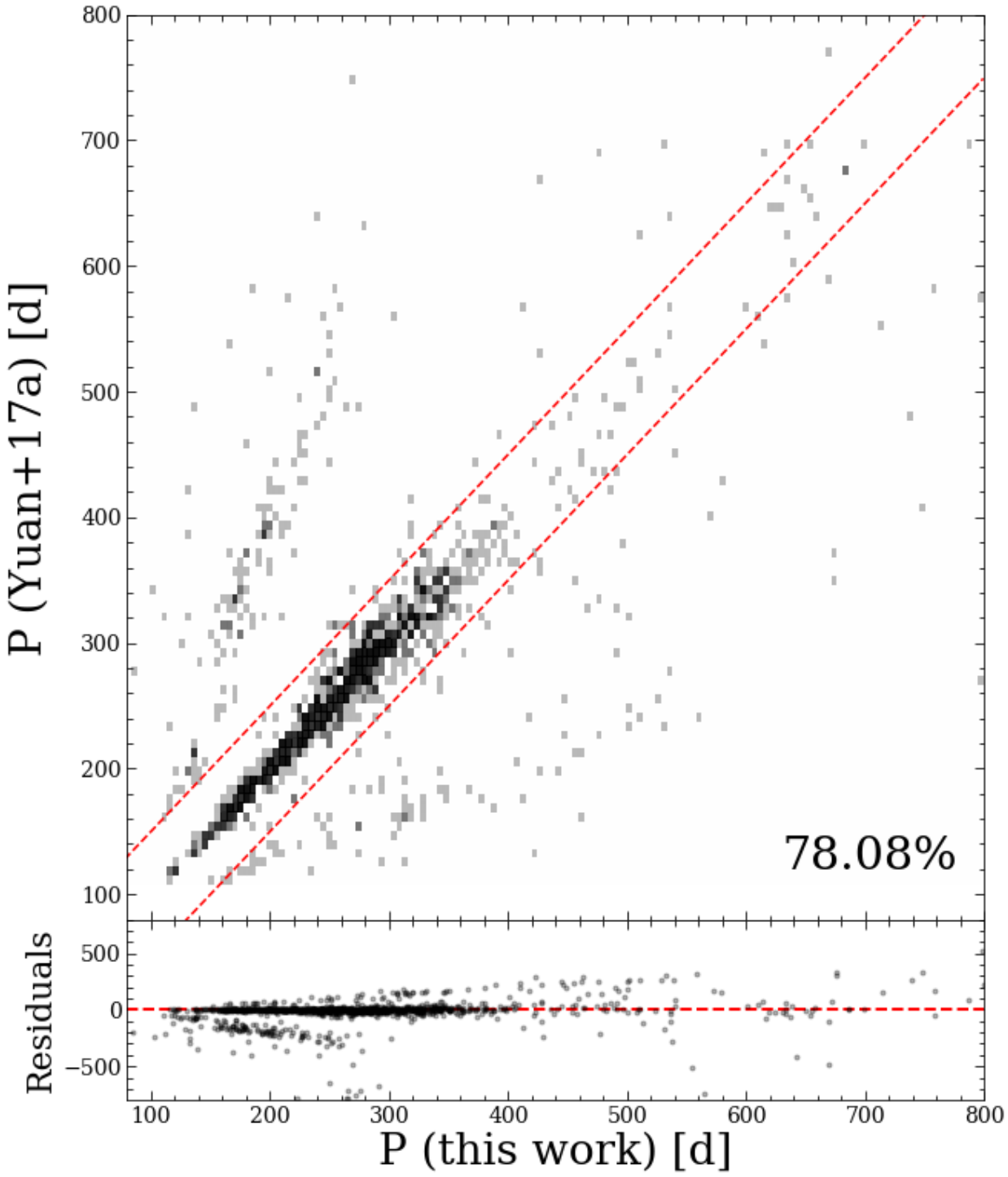

Figure 2.12 A comparison of the periods of the Mira candidates identified in Yuan et al. (2017a) that were recovered in this work. The upper panel shows the Yuan et al. (2017a) periods plotted against the periods we determined for the same objects in this work. The percentage of objects contained within the dashed red lines is shown in the lower right. The lower panel shows the residuals from subtracting the Yuan et al. (2017a) periods from this work's periods.

The NIR magnitudes were used to calculate "reddening free" Wesenheit indices (Madore, 1982) in the available bands:

$$W_{JK_S} = K_S - R^K_{JK}(J - K_S)\ ;\ R^K_{JK} = \frac{A_{K_S}}{A_J - A_{K_S}} \tag{2.4}$$

$$W_{JH} = H - R^H_{JH}(J - H)\ ;\ R^H_{JH} = \frac{A_H}{A_J - A_H} \tag{2.5}$$

with $A_J = 0.03$, $A_H = 0.02$, and $A_{K_S} = 0.01$ mag based on Schlafly and Finkbeiner (2011) and Yuan et al. (2018).

If an object had only a J or a K_S measurement, the mean $J - K_S$ value of the sample was used to determine W_{JK_S}. We created period-luminosity and period-Wesenheit diagrams to check for obvious PLRs or period-Wesenheit relations. The period-W_{JK_S} was most promising in this regard (see Figures 2.13 and 2.14) and allowed us to roughly classify objects as falling on fundamental ("FU") or first overtone ("FO") pulsation sequences, or neither ("UN": unknown). The bulk of the Yuan et al. (2017a) Miras we recovered ($\sim 1,200$) were FU pulsators. We opted to restrict ourselves to objects with W_{JK_S} values to identify our final sample of Mira candidates because of the relatively low scatter in the period-W_{JK_S} relation ($\sigma \sim 0.12 - 0.32$; Yuan et al. 2017a,b).

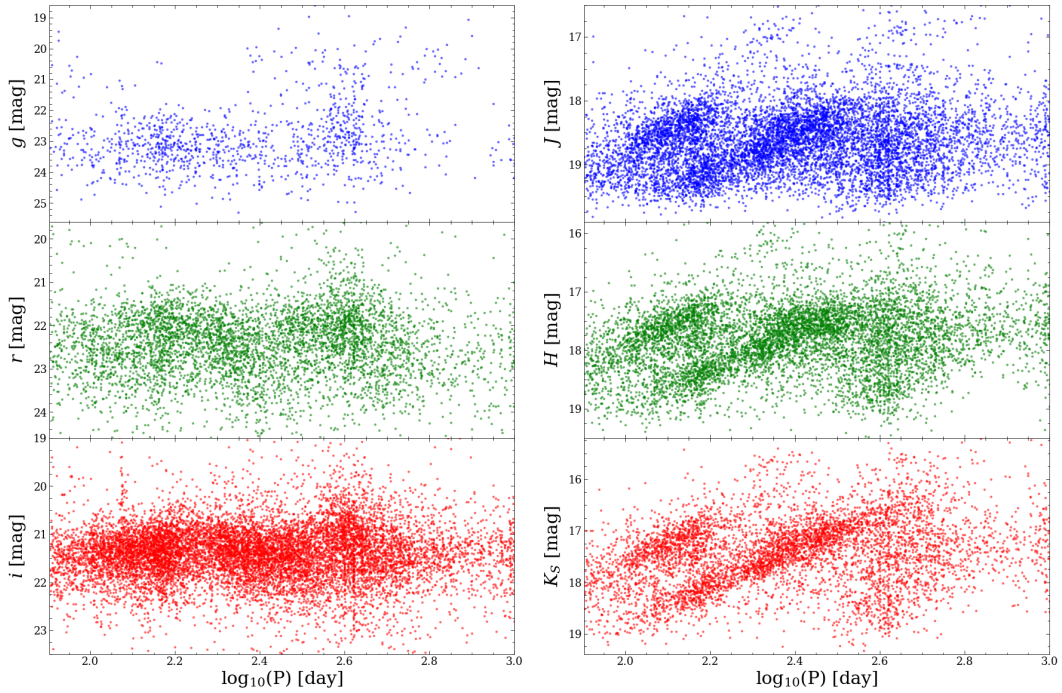

Figure 2.13 PL diagrams of the preliminary Mira candidates that remained after the cuts described in Section 2.3. Left column, top to bottom: period-g, period-r, and period-i diagrams. Left column, top to bottom: period-J, period-H, and period-K_S diagrams.

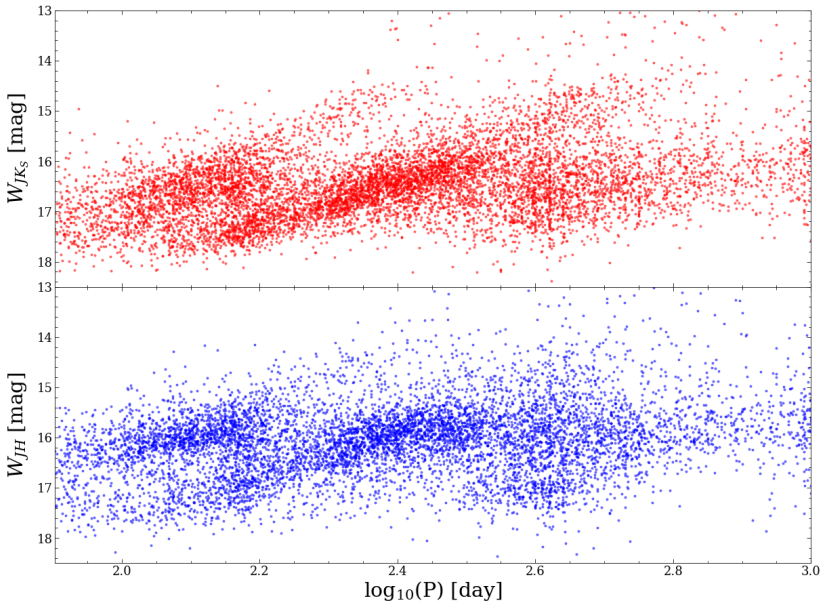

Figure 2.14 Period-Wesenheit diagrams of the preliminary Mira candidates that remained after the cuts described in Section 2.3. Upper panel: period-W_{JK_S} diagram. Lower panel: period-W_{JH} diagram.

2.4 Identifying New Mira Candidates

2.4.1 Determining Period-Wesenheit Relations from Outcomes of Machine Learning Classifiers

We used six machine learning methods as classifiers – logistic regression, random forest, linear discriminant analysis, quadratic discriminant analysis, kernel support vector machine (SVM), and positive-unlabeled learning with bagging SVM[4] – to identify new Mira candidates. All six of the methods work as binary classifiers, which is ideal for our purpose of distinguishing Miras from non-Miras. We set up the classifiers so that each classifier returned a score for each object rather than an outright classification: the higher an object's score, the more Mira-like the object was.

The classifiers were provided with five of the features described in Table 2.4, which are associated with the i-band light curves and light curve models. These features were amongst those used to identify Mira candidates in Yuan et al. (2017a); we did not consider all the features from Yuan et al. (2017a) because they used a different method to fit their light curves. We only gave the classifiers objects that had been roughly classified as FU or FO.

[4]See Mordelet and Vert (2014).

Table 2.4. The classifier features used to identify new Mira candidates. The features are ordered by decreasing importance for Mira classification as presented in Yuan et al. (2017a); the original ranks are presented here. The feature descriptions and sources are also from Yuan et al. (2017a). L: light curve; M: model.

Feature	Description	Source	Rank
$\sigma(R_q)/\sigma(\bar{m})$	Ratio of standard deviations defined below	L	2
$A_{0.9}$	Light curve range from 10th to 90th percentile	L	3
A	Light curve range	L	5
A_P	Amplitude of the periodic component	M	6
$\sigma(\bar{m})$	Standard deviation of residuals about unweighted mean magnitude, $\bar{m}$	L	8
$\sigma(R_q)$	Standard deviation of residuals from piece-wise quadratic fits*	M	10

Note. — $\sigma(R_q)$ was not used as a parameter in its own right; the description is included to define $\sigma(R_q)/\sigma(\bar{m})$.

Table 2.5. Mira/non-Mira thresholds and AUC values for each classifier.

Classifier	Threshold	AUC
Logistic Regression	0.603	0.991
Random Forest	0.195	0.993
Linear Discriminant Analysis	0.758	0.990
Quadratic Discriminant Analysis	0.833	0.991
Kernel SVM	0.845	0.993
Bagging SVM	0.933	0.989

To train and validate the classifiers, we used the Miras from Yuan et al. (2018) that we recovered in our data as well as the objects that did not pass the sample cuts described in Section 2.3. The former were considered as known Miras while the latter were considered as known non-Miras.

After training and validating the classifiers, we used the scores assigned to the validation Miras and non-Miras to create Receiver Operating Characteristic (ROC) curves and determine a threshold for each classifier that would separate Miras from non-Miras. The threshold for each method was determined by maximizing the geometric mean, which is defined as $\sqrt{\text{sensitivity} \times \text{specificity}}$, where sensitivity is the fraction of true positives and specificity is the fraction of true negatives. Using the geometric mean to determine the Mira/non-Mira threshold allows for a balance between classifier performance on both the majority and minority classes. It also avoids overfitting the negative class (non-Miras) and under-fitting the positive class (Miras). The Mira/non-Mira thresholds and area under the ROC curve (AUC) for each classifier are shown in Table 2.5.

We selected a sample of Mira candidates for each classifier by retaining the objects with a classifier score greater than or equal to the respective Mira/non-Mira threshold. We visually inspected the light curves associated every unique Mira candidate and labeled candidates as high, low, or no confidence. We only retained high confidence candidates from this point on.

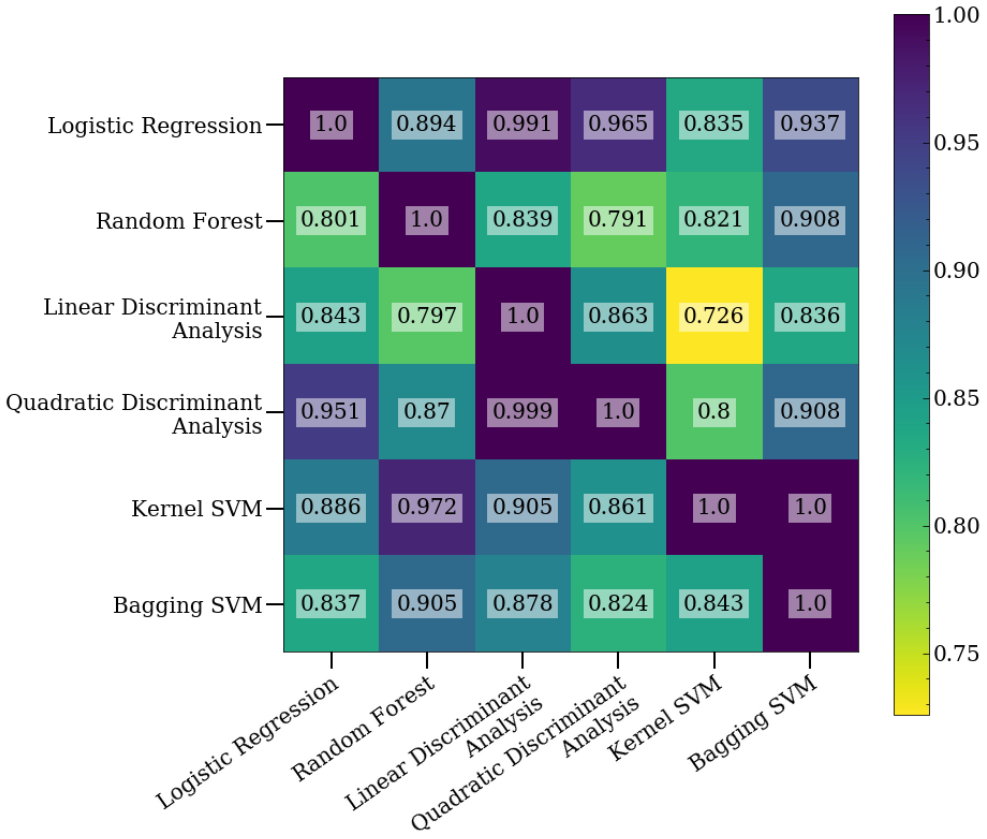

Figure 2.15 Fraction of common candidates across the samples returned by the six machine learning classifiers.

We also found that some of the Mira candidates at this point had model i-band amplitudes ≤ 0.3 mag, which we excluded. To see the initial number of candidates associated with each classifier and the number of candidates that remained after visual inspection and amplitude cuts, refer to Table 2.6. The fractions of initial candidates (the second column in Table 2.6) in common across the classifier samples are shown in Figure 2.15 and the updated W_{JK_S}-period diagram is shown in Figure 2.16, containing the objects from the last row of Table 2.6.

Table 2.6. The number of Mira candidates in each classifier sample initially, after visual inspection, and after excluding candidates with model i-band amplitude ≤ 0.3 mag.

Classifier	Initial	Visual Inspection	$A_i > 0.3$ mag
Logistic Regression	3,066	2,880	2,433
Random Forest	3,416	3,214	2,758
Linear Discriminant Analysis	3,608	3,385	2,533
Quadratic Discriminant Analysis	3,087	2,924	2,401
Kernel SVM	2,860	2,715	2,616
Bagging SVM	3,433	3,222	2,813
Unique Objects	4,275	3,982	2,916

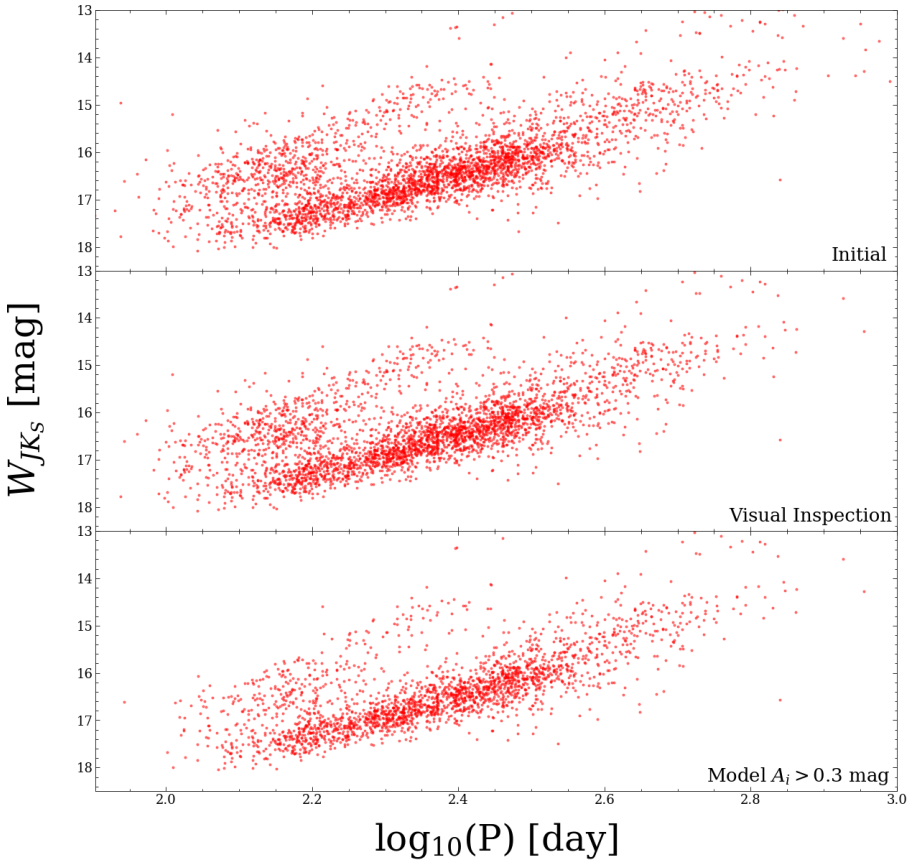

Figure 2.16 Period-W_{JK_S} diagrams of the unique objects initially identified as strong Mira candidates by the machine learning classifiers (top panel); the high confidence candidates after visual inspection (middle panel); and the candidates with model i-band amplitudes > 0.3 mag (bottom panel).

We fit linear and quadratic period-W_{JK_S} relations to the O-rich objects in each classifier sample. We assumed that objects with $J-K_S \leq 1.30$ were O-rich and objects with $J-K_S > 1.30$ were C-rich objects based on LMC Miras described in Soszyński et al. (2009a) (see Figure 2.17). This distinction between O- and C-rich objects excluded objects with only a J or a K_S measurement. The linear and quadratic equations are defined as Equations 2.6 and 2.7 respectively:

$$W_{JK_S} = a_0 + a_1(\log_{10}P - 2.3) \tag{2.6}$$

$$W_{JK_S} = a'_0 + a'_1(\log_{10}P - 2.3) + a'_2(\log_{10}P - 2.3)^2 \tag{2.7}$$

To fit the period-W_{JK_S} relations, we first separated the FU and FO objects by eye and fit relations to each sample. We then fit all the objects using the initial FU relation with 2.5σ clipping and following that, fit the initial FO relation to the remaining objects with 2.5σ clipping as well. We then fit relations to the sigma-clipped samples of FU and FO objects, which served as the final period-W_{JK_S} relations. The sigma-clipped samples for the linear and quadratic fits are shown in Figures 2.18 and 2.19 respectively, and the PLR coefficients are shown in Tables 2.7 and 2.8.

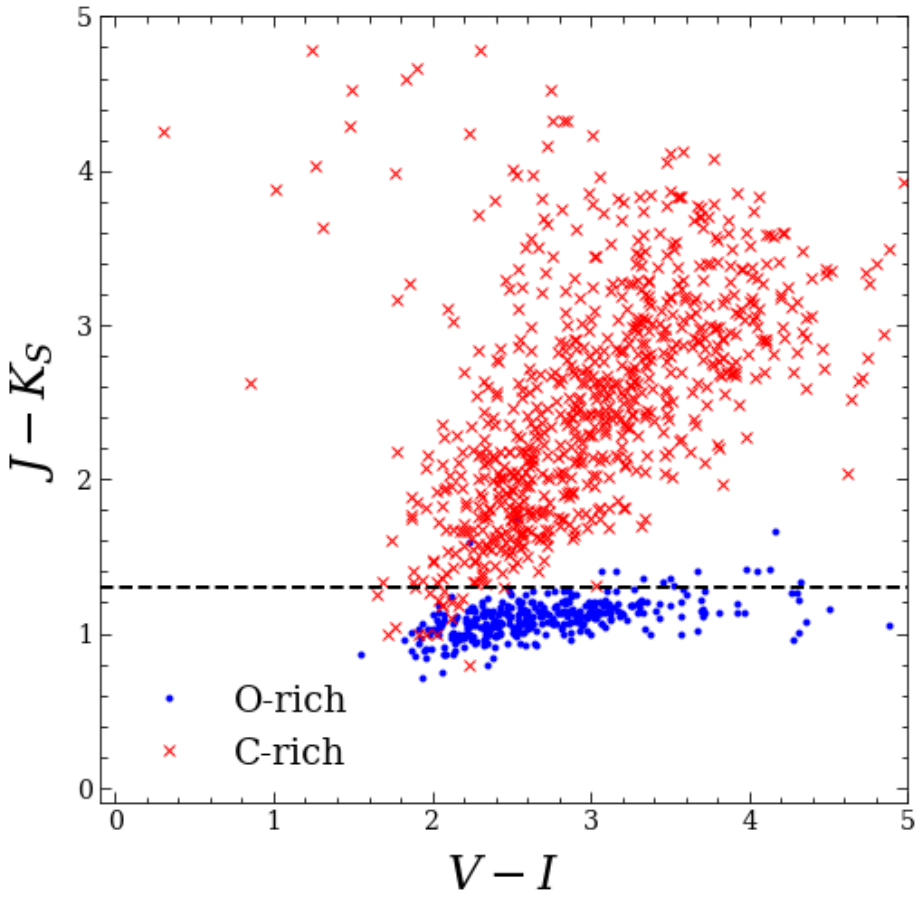

Figure 2.17 $J - K_S$ versus $V - I$ for the O-rich (blue dots) and C-rich (red crosses) OGLE LMC Miras. The O/C-rich classifications come from Soszyński et al. (2009a). The horizontal line is drawn at $J - K_S = 1.30$, which is the threshold we used to select O-rich objects from our Mira candidates.

Table 2.7. Coefficients associated with the linear period-W_{JK_S} relations fit to the O-rich fundamental (FU) and first overtone (FO) M33 Mira candidates with $P < 400$ d.

Classifier	Mode	a_0	a_1	σ	N
Logistic Regression	FU	16.901 ± 0.009	-4.051 ± 0.072	0.161	612
Random Forest	FU	16.898 ± 0.008	-4.011 ± 0.065	0.160	681
Linear Discriminant Analysis	FU	16.894 ± 0.009	-3.987 ± 0.071	0.162	627
Quadratic Discriminant Analysis	FU	16.903 ± 0.009	-4.014 ± 0.071	0.159	596
Kernel SVM	FU	16.903 ± 0.008	-4.011 ± 0.066	0.158	650
Bagging SVM	FU	16.894 ± 0.008	-3.975 ± 0.065	0.161	692
Logistic Regression	FO	15.414 ± 0.050	-6.817 ± 0.361	0.493	81
Random Forest	FO	15.507 ± 0.056	-5.913 ± 0.372	0.451	104
Linear Discriminant Analysis	FO	15.402 ± 0.050	-6.572 ± 0.350	0.485	84
Quadratic Discriminant Analysis	FO	15.418 ± 0.050	-6.843 ± 0.358	0.489	81
Kernel SVM	FO	15.383 ± 0.056	-6.652 ± 0.371	0.446	92
Bagging SVM	FO	15.488 ± 0.051	-5.872 ± 0.332	0.462	104

Table 2.8. Coefficients associated with the quadratic period-W_{JK_S} relations fit to the O-rich fundamental (FU) and first overtone (FO) M33 Mira candidates.

Classifier	Mode	a'_0	a'_1	a'_2	σ	N
Logistic Regression	FU	16.906 ± 0.010	-3.998 ± 0.083	-0.644 ± 0.372	0.163	631
Random Forest	FU	16.905 ± 0.009	-3.926 ± 0.070	-0.890 ± 0.338	0.162	702
Linear Discriminant Analysis	FU	16.903 ± 0.010	-3.961 ± 0.081	-0.676 ± 0.369	0.164	644
Quadratic Discriminant Analysis	FU	16.907 ± 0.010	-3.972 ± 0.082	-0.749 ± 0.367	0.163	617
Kernel SVM	FU	16.916 ± 0.009	-3.946 ± 0.071	-0.893 ± 0.334	0.157	664
Bagging SVM	FU	16.904 ± 0.009	-3.932 ± 0.069	-0.824 ± 0.335	0.163	710
Logistic Regression	FO	15.636 ± 0.061	-4.925 ± 0.307	1.417 ± 1.074	0.738	101
Random Forest	FO	15.680 ± 0.058	-4.515 ± 0.267	0.522 ± 0.993	0.586	116
Linear Discriminant Analysis	FO	15.640 ± 0.060	-4.769 ± 0.290	1.135 ± 1.037	0.720	107
Quadratic Discriminant Analysis	FO	15.641 ± 0.061	-4.947 ± 0.306	1.436 ± 1.070	0.733	101
Kernel SVM	FO	15.683 ± 0.060	-4.511 ± 0.279	0.523 ± 1.012	0.594	109
Bagging SVM	FO	15.671 ± 0.057	-4.585 ± 0.254	0.429 ± 0.928	0.637	122

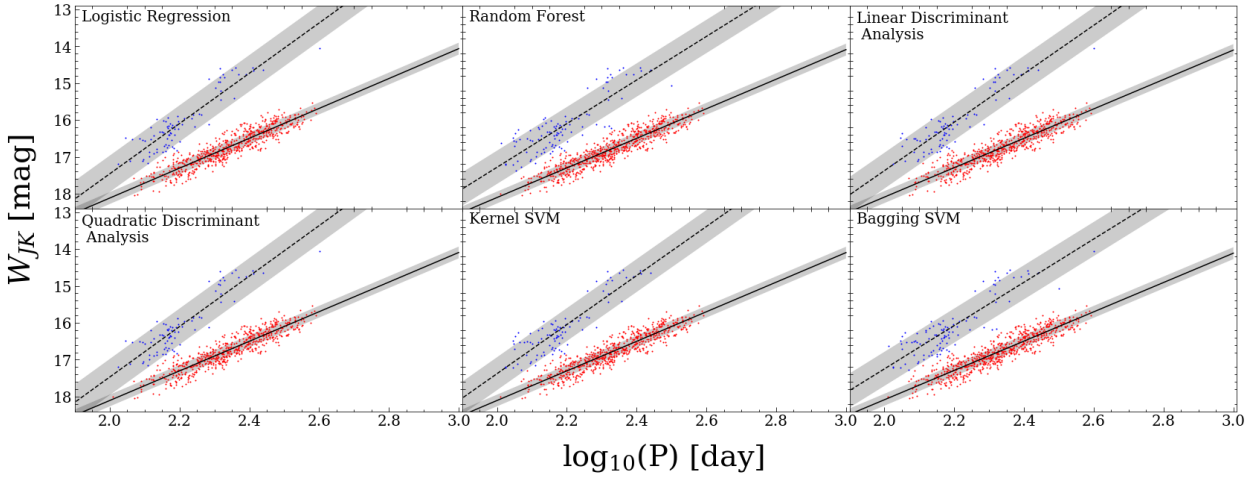

Figure 2.18 Linear period-W_{JK_S} relations for the O-rich FU (red) and FO (blue) objects in each classifier sample. The FU relations are shown using a solid line and the FO relations are shown using a dashed line. The shaded regions indicate the 1σ spread. From the upper left, moving clockwise, the classifiers associated with the respective sample are: logistic regression, random forest, linear discriminant analysis, bagging SVM, kernel SVM, and quadratic discriminant analysis.

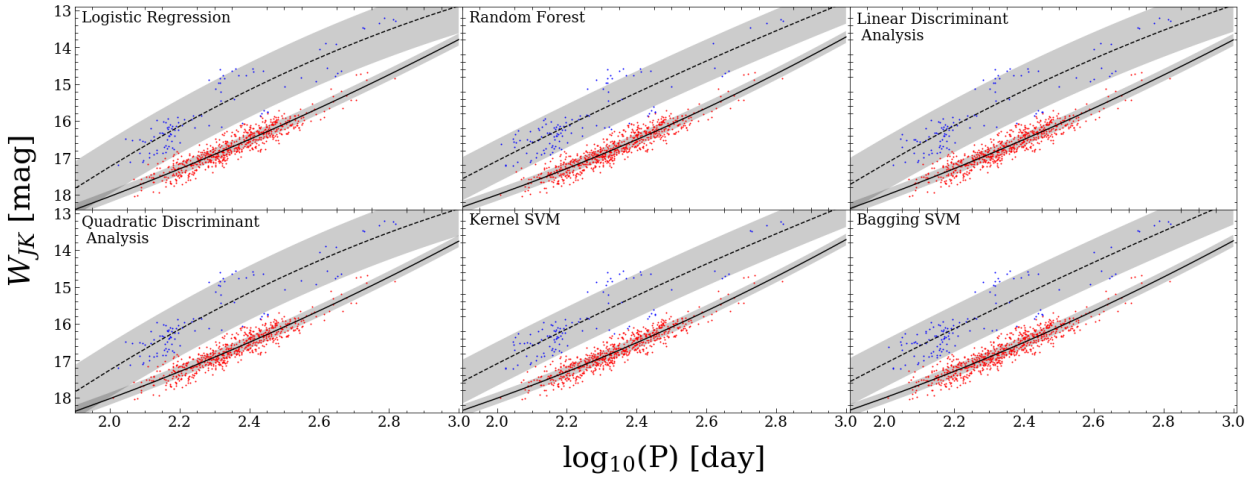

Figure 2.19 Same as Figure 2.18, but for the quadratic period-W_{JK_S} relations.

2.4.2 Determining Period-Wesenheit Relations from OGLE LMC Long-Period Variables

We also identify a sample of Mira candidates by using period–W_{JK_S} relations from Soszyński et al. (2009a) to fit similar relations to the sample of M33 Mira candidates identified in Section 2.3. Soszyński et al. (2009a) describes the fourth component of the OGLE-III catalog of variable stars, which contains LPVs identified in the LMC. Among these LPVs are 1,667 Miras and 11,128 semi-regular variables (SRVs). The work also identifies two sequences in period-luminosity space — Wood's C and C′ sequences (Ita et al., 2004) — which Miras and SRVs fall on. In our work, FU objects fall on the C sequence while FO objects fall on the C′ sequence. For this part of the analysis, we excluded M33 objects whose amplitude fell in the bottom 20th percentile.

We rederived the LMC period–W_{JK_S} diagram by first cross-matching the OGLE Miras and SRVs with the NIR catalog presented in Kato et al. (2007) to get JHK_S magnitudes for the OGLE objects. We then calculated W_{JK_S} using the definition presented in Soszyński et al. (2009a)[5]. All but 3 of the OGLE Miras fell on the C sequence, so we relied on the OGLE SRVs that fell on the C′ sequence to fit a relation to the M33 FO objects.

To distinguish between O- and C-rich objects, we again used a threshold of $J-K_S > 1.30$ to denote C-rich objects. We fit a linear W_{JK}–period relation in the form of Equation 2.6 with 2.5σ clipping to the O-rich LMC Miras that fell on the C sequence. We then fit the W_{JK}–period relation of the O-rich M33 FU objects with the same slope (a_1) as the LMC FU relation and determined the difference between the intercepts (a_0) of the LMC and M33 W_{JK}–period relations. Because M33 FO PLR fit would be dependent on the FU PLR intercept difference, we included Yuan et al. (2018) Miras in the M33 FU PLR fit to increase our sample size. We then fit a linear W_{JK}–period relation to O-rich SRVs that fell on the C′ sequence, applied the aforementioned offset difference to the intercept of this relation, and used the same slope and intercept to fit a linear W_{JK}–period relation to the O-rich M33 FO

[5] $W_{JK_S} = K_S - 0.686(J - K_S)$

Table 2.9. Coefficients associated with the linear period-W_{JK_S} relations fit to the O-rich OGLE and M33 objects. The number of M33 objects shown in parentheses are the number of Mira candidates that were not described in Yuan et al. (2018).

Host	Object	Mode	a_0	a_1	σ	N
LMC	Mira	FU	10.847 ± 0.017	-3.917 ± 0.137	0.139	219
M33	Mira	FU	16.957 ± 0.007	—	0.103	622 (268)
LMC	SRV	FO	9.216 ± 0.007	-4.249 ± 0.018	0.108	2,735
M33	Mira	FO	15.875 ± 0.025	—	0.346	(309)

objects. The slope was fixed while the intercept was allowed to vary. The fundamental and first overtone LMC and M33 PLRs are shown in Figures 2.20 and 2.21 respectively, while the PLR coefficients are in Table 2.9.

We use the period-W_{JK_S} relations from Sections 2.4.1 and 2.4.2 to get a preliminary distance modulus for M33 as:

$$m_{M33} - M = \mu_{M33} \tag{2.8}$$

$$m_{LMC} - M = 5\log_{10}(\frac{d_{LMC}}{10}) \implies M = m_{LMC} - 5\log_{10}(\frac{d_{LMC}}{10}) \tag{2.9}$$

where m_{M33} is derived from the period-W_{JK_S} relation of O-rich, fundamental M33 objects identified by the Kernel SVM ($a_0 = 16.903 \pm 0.008$; $a_1 = -4.011 \pm 0.066$), or from fitting a fixed LMC-based slope to the M33 Mira candidates and the recovered Yuan et al. (2018) Miras ($a_0 = 16.957 \pm 0.007$; $a_1 = -3.917$); m_{LMC} is derived from the period-W_{JK_S} relation of O-rich, fundamental LMC objects ($a_0 = 10.847 \pm 0.017$; $a_1 = -3.917 \pm 0.137$); d_{LMC} is the LMC distance from Pietrzyński et al. (2019) (49.59 ± 0.09 (statistical) $\pm$ 0.54 (systematic) kiloparsecs); M is the absolute magnitude of a fundamental, O-rich Mira with $P < 400$ d; and μ_{M33} is the distance modulus of M33. We find that $\mu_{M33} = 24.52 - 24.58 \pm 0.04$ mags pending crowding corrections, which is consistent with previously measured distance moduli

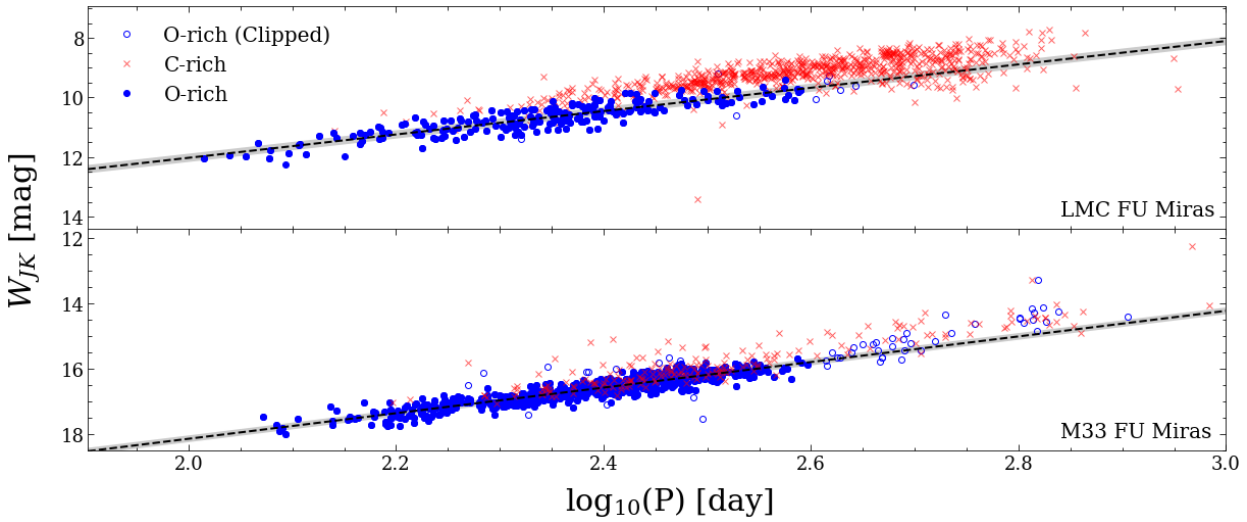

Figure 2.20 Period-W_{JK_S} relations for the fundamental LMC (upper panel) and M33 Miras (lower panel). The shaded regions indicate the 1σ spread. O-rich objects: filled blue circles; clipped O-rich objects: unfilled blue circles; C-rich objects: red crosses.

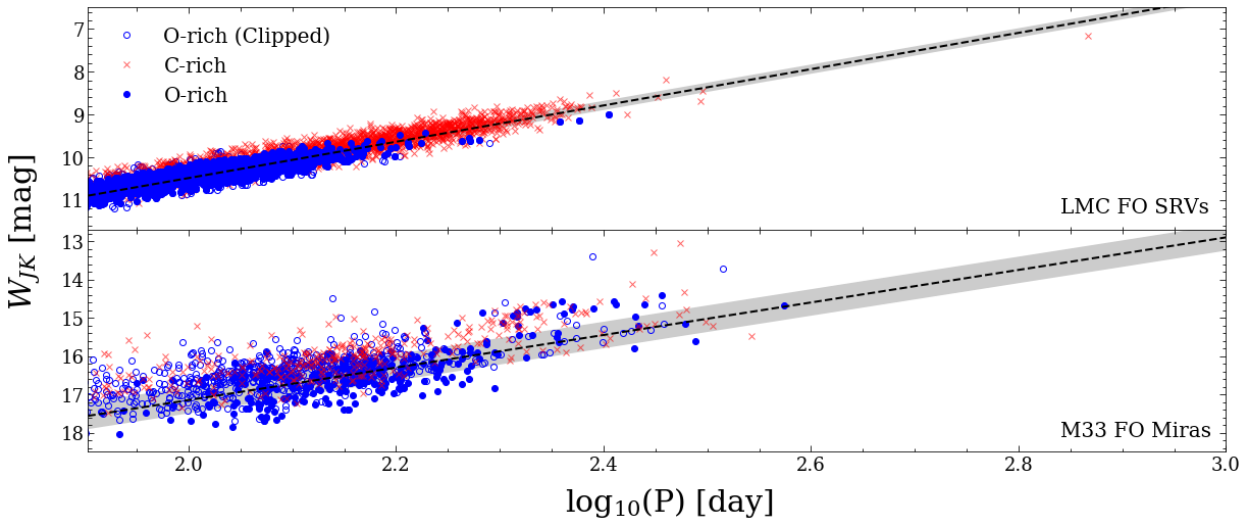

Figure 2.21 Same as Figure 2.20 but for the first overtone LMC SRVs (upper panel) and the M33 Miras (lower panel).

of M33 (Gieren et al., 2013; Ren et al., 2021; Sarajedini, 2021).

2.4.3 Comparison to Yuan et al. (2017a) Mira PLRs

Yuan et al. (2017a) derived quadratic PLRs for O-rich Miras hosted in the LMC and M33 in the optical (I_m), NIR (JHK_S), and mid-infrared (3.6, 4.5 μm), as well as for W_{JK_S}. These PLRs were fit to objects that fell on the C sequence, and the NIR photometry used in Yuan et al. (2017a) came from Javadi et al. (2015), the same catalog used to calibrate our NIR photometry. The quadratic PLRs presented in Section 2.4.1 are consistent with the Yuan et al. (2017a) period-W_{JK_S} relation[6] within $\sim 1.2 - 2\sigma$.

2.4.4 Period-Luminosity Relations in *gri*

Iwanek et al. (2021) analysed the light curves of LMC Miras in the optical and infrared and derived variability amplitude ratios and phase-lags for different bands. They also generated spectral energy distributions (SEDs) based on a high quality sample of O- and C-rich Miras. These SEDs were used to create synthetic linear PLRs for O- and C-rich Miras in 42 optical and infrared bands, including LSST *gri*.

We fit *gri* linear PLRs with 2.5σ clipping in the form of Equation 2.6 to the unique, O-rich FU Mira candidates identified in Section 2.4.1 (the ML-M33 sample) and the O-rich FU Mira candidates used to fit the M33 period-W_{JK_S} relation in Section 2.4.2 (the LMC-M33 sample). For one set of fits, we allowed both the intercept and slope to vary, and for the other, we fixed the slope to the value from Iwanek et al. (2021). The PLRs are shown in Figure 2.22 and the PLR parameters are shown in Table 2.10. The intercepts for candidates from the same sample are consistent within their respective uncertainties while the slopes vary significantly. The *i*-band PLR shows the lowest scatter, but it also was fit using more objects than the *g*- and *r*-band PLRs.

[6] $a_0 = 17.19 \pm 0.01$, $a_1 = -4.15 \pm 0.02$, $a_2 = -2.46 \pm 0.04$; a_1, a_2 derived from LMC objects and fixed to fit M33 objects.

Table 2.10. Coefficients associated with the linear *gri* PLRs fit to the unique, O-rich candidates with $P < 400$ d identified using machine learning classifiers (the ML-M33 sample) and the O-rich candidates with $P < 400$ d identified by fitting LMC-based PLRs to the M33 Mira candidates (the LMC-M33 sample). The "Slope" columns indicates whether a_1 was kept fixed or allowed to vary. The a_1 values and uncertainties for the "Fixed" rows are from Iwanek et al. (2021).

Band	Slope	Sample	a_0	a_1	σ	N
g	Free	LMC-M33	23.475 ± 0.062	1.050 ± 0.630	2.116	98
	Fixed	LMC-M33	23.393 ± 0.067	3.830 ± 2.378	2.265	98
	Free	ML-M33	23.298 ± 0.054	0.876 ± 0.457	2.021	163
	Fixed	ML-M33	23.480 ± 0.056	3.830 ± 2.378	2.189	163
r	Free	LMC-M33	22.602 ± 0.035	2.934 ± 0.355	1.400	293
	Fixed	LMC-M33	22.630 ± 0.032	1.892 ± 1.816	1.343	293
	Free	ML-M33	22.394 ± 0.025	1.511 ± 0.214	1.117	547
	Fixed	ML-M33	22.419 ± 0.025	1.892 ± 1.816	1.141	547
i	Free	LMC-M33	21.256 ± 0.019	1.856 ± 0.149	0.326	622
	Fixed	LMC-M33	21.366 ± 0.016	0.653 ± 1.462	0.345	622
	Free	ML-M33	21.291 ± 0.010	0.543 ± 0.080	0.345	1177
	Fixed	ML-M33	21.295 ± 0.010	0.653 ± 1.462	0.345	1177

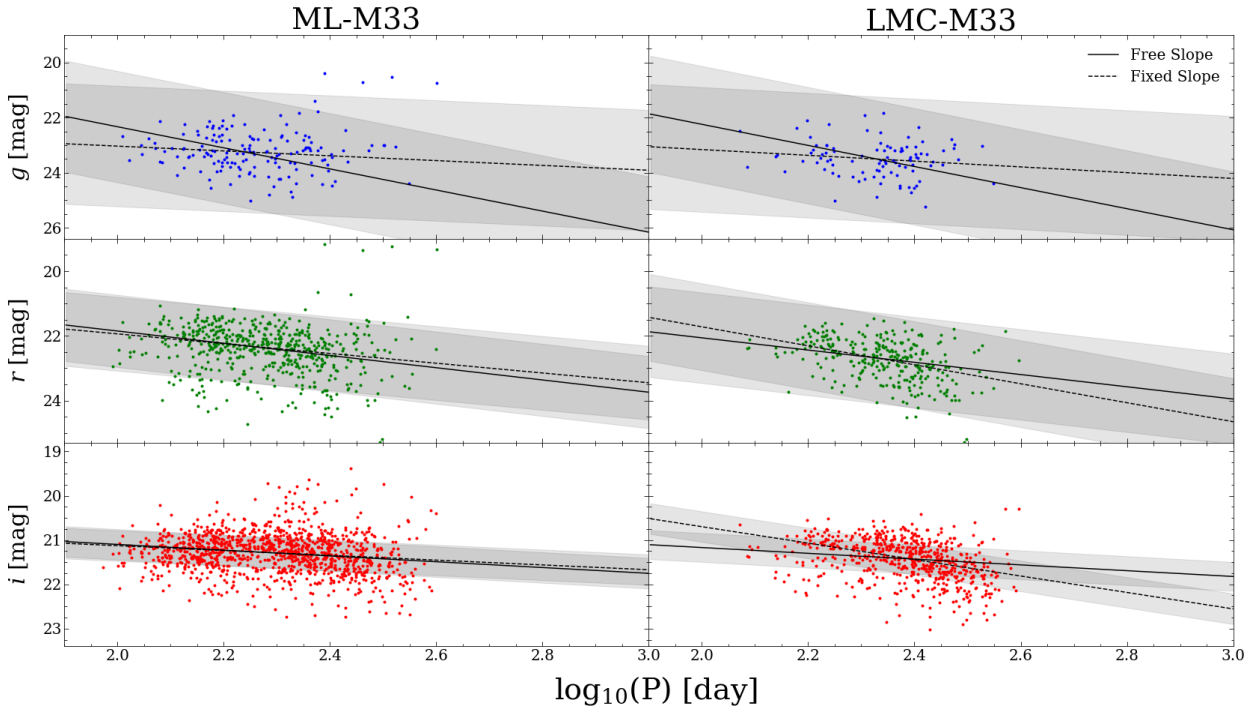

Figure 2.22 PLRs of the Mira candidates identified in Sections 2.4.1 (ML-M33; left column) and 2.4.2 (LMC-M33; right column). The solid lines show the PLR fit where the slope and intercept were allowed the vary and the dashed lines show the PLR fit where the slope was fixed to the value from Iwanek et al. (2021). The shaded regions indicate the 1σ spread.

2.5 Summary

We used multiband observations and machine learning classifiers to identify 2,916 new Mira candidates in M33. For the first time, we find evidence for a first overtone pulsation sequence in the M33 Mira candidates. We present a catalog of Mira candidates with empirical measurements in the LSST photometric bands that can be used to inform Mira searches in the LSST era. We fit period-Wesenheit relations and PLRs to the Mira candidates we obtained and compared them to previously derived empirical and synthetic Mira PLRs. We showed how Mira candidates can be identified by using optical light curves and models and note the importance of NIR information in confirming these candidates. We also note that NIR observations, when available, are superior to creating high fidelity samples of Miras for distance measurements since NIR data can be used to distinguish between first overtone and fundamental pulsators.

Facilities: CFHT

Software: Brazos Computational Resource; `DAOPHOT`, `ALLSTAR`, `ALLFRAME`, `TRIAL` (Stetson 1987, Stetson 1994, Stetson 1996); Astropy (Astropy Collaboration et al., 2013, 2018); Project Jupyter (Kluyver et al., 2016); Matplotlib (Hunter, 2007); Numpy (Oliphant, 2006); Pandas (McKinney et al., 2010); SciPy (Jones et al., 2001); IRAF (Tody, 1986a); SAOImage DS9 (Joye and Mandel, 2003).

3. *H*-BAND LIGHT CURVES OF MILKY WAY CEPHEIDS VIA DIFFERENCE IMAGING ANALYSIS

We present H-band light curves of Milky Way Classical Cepheids observed as part of the Dark Energy, H_0, and peculiar Velocities using Infrared Light from Supernovae (DEHVILS) survey with the Wide-Field Infrared Camera on the United Kingdom Infrared Telescope. Due to the crowded nature of these fields caused by defocusing the Camera, we performed difference-imaging photometry by modifying a pipeline originally developed to analyze images from the *Transiting Exoplanet Survey Satellite*. We achieved a photometric precision in line with expectations from photon statistics, reaching 0.01 mag for $8 \lesssim H \lesssim 11$ mag. We used the resulting Cepheid light curves to derive corrections to "mean light" for random-phase *Hubble Space Telescope* observations in $F160W$. We find good agreement with previous phase corrections based on VI light curves from the literature, with a mean difference of -1 ± 6 millimag.*

3.1 Motivation

A source of systematic uncertainty in local measurements of H_0 comes from comparing MW Cepheids to their extragalactic counterparts. One route to addressing this uncertainty lies in the *Gaia* mission (Gaia Collaboration et al., 2016), which is providing high-precision parallaxes for billions of objects, including MW Cepheids. Presently, the intermediate *Gaia* data products require parallax offsets that depend on magnitude and ecliptic latitude (Lindegren et al., 2018, 2021a,b).

HST observations of MW Cepheids can play a critical role in local H_0 measurements, as they can be simultaneously used to determine the *Gaia* parallax offset for Cepheids and

*This chapter reproduces the majority of an article that was published in the Astrophysical Journal Supplement Series (ApJS) following peer review. The version of record is located in ApJS, Volume 258, Number 2, January 2022, and is available online at: https://doi.org/10.3847/1538-4365/ac41d3.

reduce the zero-point errors that arise while comparing MW Cepheids to extragalactic variables. Such observations were obtained for 29/40 targets during HST Cycle 27 (prop #15879, PI: Riess). The targets were all known MW Cepheids with photometric parallaxes $\pi_{\rm phot} > 0.8$ mas (to maximize sensitivity to the *Gaia* offset), $V > 6$ mag (to avoid saturation by *Gaia*), and $A_H < 0.6$ mag (to minimize the impact of reddening). Since the HST observations were obtained at random phases due to the "snapshot" nature of the program, ground-based optical or NIR light curves must be used to correct the single-epoch HST magnitudes to "mean light," or the mean HST magnitude of a given Cepheid. Riess et al. (2021a) presented results based on all observations obtained for this program through the end of 2020 (25/29 targets), relying on VI data for phase corrections. They obtained $H_0 = 73.2 \pm 1.3$ km s^{-1} Mpc^{-1}, a 1.8% measurement that exceeds the Planck CMB+ΛCDM expectation by 4.2σ.

As part of this HST program, we aimed to obtain H-band ground-based light curves for as many of these Cepheids as possible to check the consistency of phase corrections obtained from optical and NIR data. We used observations taken for the Dark Energy, H_0, and peculiar Velocities using Infrared Light from Supernovae (DEHVILS) survey with the Wide-Field Infrared Camera (WFCAM) on the United Kingdom Infrared Telescope (UKIRT). To avoid saturation from the target Cepheids, WFCAM is defocused prior to the Cepheid observations. Consequently, the resulting images show significant crowding and blending. This renders typical aperture or point-spread function (PSF) photometry techniques less effective, which is why we turned to difference-imaging analysis (DIA).

The basis of DIA is determining the flux difference of a source between a reference and a science image. The reference image typically has the highest signal-to-noise ratio (S/N) (and in some cases the best resolution) of all available images and is degraded to match the conditions of a given science image before it is subtracted from the science image. Objects with constant flux levels will be subtracted into background noise while variable objects will leave behind some residual flux (Alard and Lupton, 1998). Aperture or PSF photometry can then be performed on the differenced images to extract the light curves of variable

objects. The DIA implementation used in this work is a slightly modified version of the method presented in Oelkers and Stassun (2018) and Oelkers and Stassun (2019), which was developed to extract light curves from images taken by the *Transiting Exoplanet Survey Satellite* (TESS).

The rest of this chapter is organized as follows: Section 3.2 describes the DEHVILS survey along with the H-band Cepheid observations and image preprocessing, Section 3.3 describes the DIA procedure, Section 3.4 presents the Cepheid light curves and compares the derived phase corrections to HST observations to similar corrections based on VI light curves, and Section 3.5 provides a summary of this work.

3.2 Observations and Image Preprocessing

3.2.1 The DEHVILS Survey

The DEHVILS survey started in northern spring 2020 with the primary goal of using UKIRT to build a NIR sample of SNe Ia. The survey aims to measure the local growth of structure parameters and provide an "anchor" sample for next-generation high-redshift samples such as those from the Rubin Observatory and the *Nancy Grace Roman Space Telescope*. DEHVILS has observed over 100 SNe Ia in YJH in its first year of operations and, with collaborators at the University of Hawai'i, over 300 SNe Ia in J.

UKIRT's WFCAM has already observed ∼17,900 square degrees of sky in J as part of the UKIRT Hemisphere Survey (Dye et al., 2018) and ∼6200 square degrees in $zYJHK$ as part of the UKIRT Infrared Deep Sky Survey (Lawrence et al., 2007). Thanks to the large-area footprint and WFCAM's ~ 1 deg. field of view, the photometry can be calibrated relative to the 2MASS Point Source Catalog (PSC; Skrutskie et al. 2006) at the $\sim 1\%$ level (Hodgkin et al., 2009). DEHVILS also uses observations of `CALSPEC` standard stars (Bohlin, 1996) with in-focus and defocused observations to measure the calibration and linearity of the UKIRT system.

Table 3.1. Milky Way Cepheids observed by the DEHVILS survey

Name	RA (J2000)	Dec (J2000)	H [mag]	log P [day]
RX Cam	04:04:58.5	+58:39:35.2	4.864 ± 0.021	0.898
RV Sco	16:58:19.7	−33:36:32.8	4.817 ± 0.075	0.783
BF Oph	17:06:05.5	−26 34 50.0	5.282 ± 0.043	0.609
AP Sgr	18:13:02.5	−23:07:02.2	4.980 ± 0.039	0.704
SS Sct	18:43:43.5	−07:43:52.0	5.910 ± 0.031	0.565
TX Cyg	21:00:06.4	+42:35:51.2	4.844 ± 0.025	1.168
V0386 Cyg	21:14:40.4	+41:42:58.8	5.700 ± 0.009	0.721

Note. — H magnitudes and uncertainties from the 2MASS PSC (Skrutskie et al., 2006); periods from Riess et al. (2021a).

3.2.2 Observations and Image Preprocessing

DEHVILS targeted 12 MW Cepheids from the aforementioned HST program that were observable from Hawai'i. Though these Cepheids will normally saturate at the minimum UKIRT exposure times, by defocusing the telescope we can avoid the nonlinear regime. We present the analysis for seven of these variables whose observations have been completed. Each target was observed for $11-20$ epochs spread over $2-3$ months between May 2020 and October 2020.

Table 3.1 presents the mean H magnitudes and periods of these objects. The magnitudes and associated uncertainties are from the 2MASS PSC while the periods are from Riess et al. (2021a). The Cepheid periods were derived while applying the phase correction procedure that is described briefly in Section 3.4.2 and in more detail in the appendix of Riess et al. (2018a). The procedure relies on multiband literature photometry, whose sources are shown in Tables 2 and 4 of Riess et al. (2021a). The long baseline of the photometry used ($\sim 20-25$ yr) yields negligible uncertainties in the derived periods.

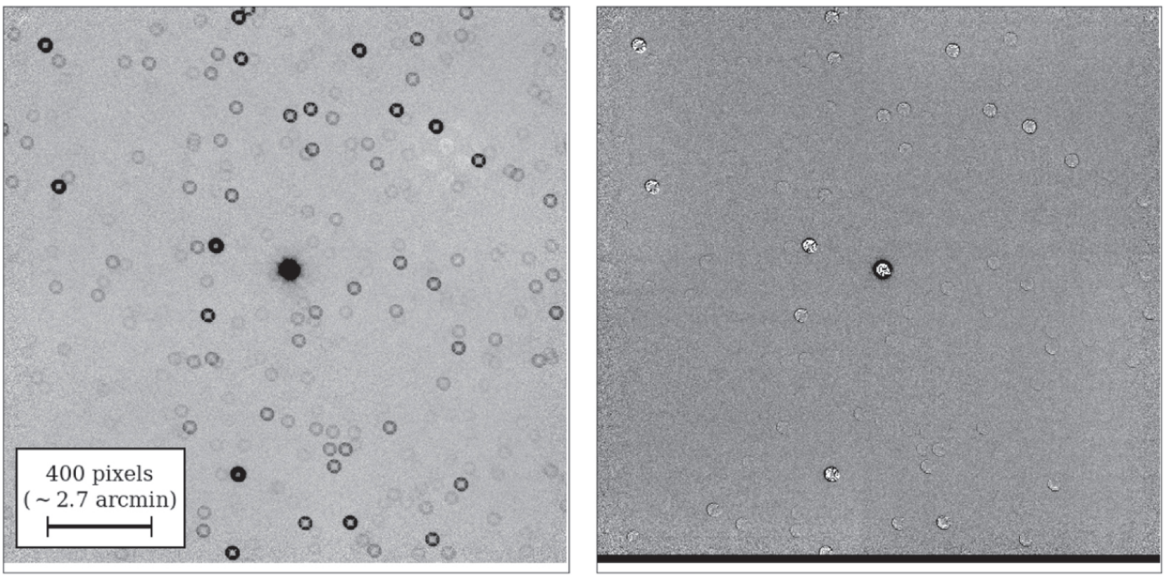

Figure 3.1 A representative science image (left) of the RX Cam field, with the Cepheid near the center. The differenced image (right) is the result of subtracting the convolved reference image from the science image. The color scale is inverted for clarity. North is up and east is to the left.

WFCAM is a wide-field infrared camera consisting of four detectors (arranged in a 2×2 array), each with a field of view of 0.21 sq. deg. and a plate scale of 0.4 arcsec per pixel. The detectors cover 13.65 arcmin on a side and are spaced 12.65 arcmin apart. Available filters include $zYJHK$ (Casali et al., 2007).

In a given exposure, the relevant Cepheid was observed by one of the four WFCAM detectors. We obtained two images per epoch for a given Cepheid, rotated 90 degrees from each other. The left panel of Figure 3.1 shows a typical image of one of our targets.

Images of a given Cepheid were aligned by updating their World Coordinate System (WCS) information prior to running the DIA pipeline. The first image from the first epoch of a given object was adopted as the reference WCS. At least 12 bright, isolated stars were visually identified in all images of a given field and their (x, y) positions were used to derive geometric transformations using IRAF (Tody, 1986b), with iterative rejection of outliers.

3.3 Difference Imaging Procedure

3.3.1 DIA Pipeline for TESS Full-frame Images

This work used a modified version of the difference-imaging pipeline from Oelkers et al. (2015) and Oelkers and Stassun (2018, 2019) (hereafter OS-DIA) to measure the photometry of each Cepheid. The OS-DIA pipeline was originally designed to measure stellar photometry from defocused images generated by the Chinese Small Telescope Array (CSTAR) and was adapted to extract light curves from TESS full-frame images (FFIs) (Oelkers et al., 2015; Oelkers and Stassun, 2018). In its current form, the pipeline queries the TESS Input Catalog (TIC; Stassun et al. 2018), which is based on the 2MASS PSC, to determine the sources in a given image. The pipeline reduced more than 106 images from CSTAR, and has generated more than 100 million light curves from TESS FFIs with a precision that has met the expectation of initial prediction models (60 ppm $\mathrm{hr}^{-0.5}$; Ricker et al. 2014; Oelkers et al. 2015; Sullivan et al. 2015).

The OS-DIA pipeline uses a Dirac δ-function kernel to transform reference images and account for "non-Gaussian, arbitrarily shaped PSFs," such as those seen in the defocused WFCAM images of this work. This kernel type provides more flexibility when characterizing non-Gaussian PSFs because each individual kernel basis is independently solved for, which results in a kernel map that is not required to be Gaussian in shape. Light curves of all objects are extracted from the differenced images via aperture photometry and detrended (removed low level frame-to-frame systematics) using the light curves of sources with low dispersion that have similar magnitudes and are nearby to the variable objects on the detector. The reference image flux of a source is added to its flux in the differenced images, so the magnitudes returned by the pipeline are instrumental magnitudes. We employed the OS-DIA pipeline on the WFCAM images with a spatially constant 5×5 pixel kernel, since our initial testing showed first- and second-order spatially varying kernels provided little improvement in photometric precision but significantly increased the runtime of the pipeline.

Figure 3.2 shows a typical kernel for one of our images and its efficacy at convolving the reference image to match the PSF of the image to be differenced.

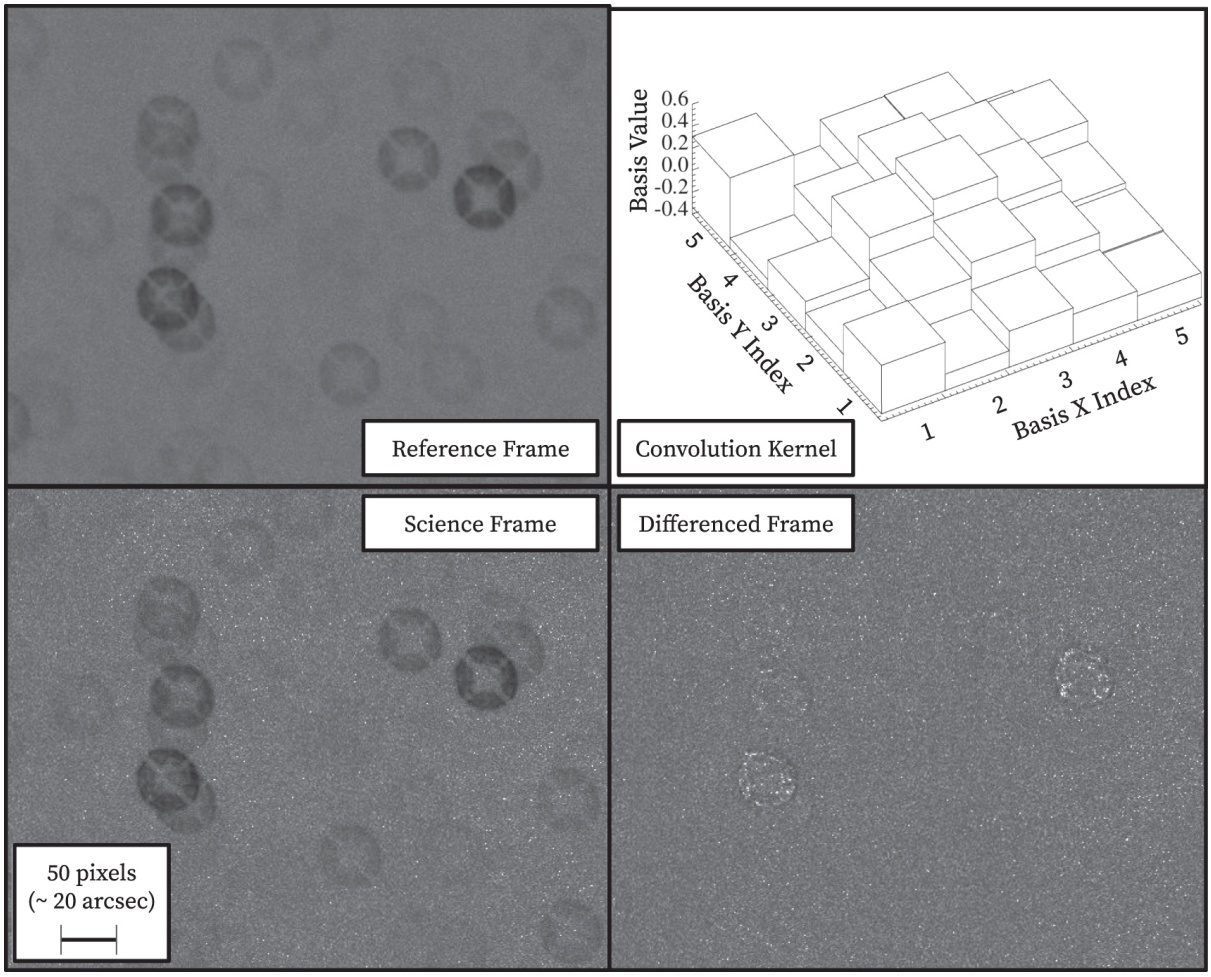

Figure 3.2 Top left: a 500×400 pixel cutout of the RX Cam reference frame. Top right: a 3D visualization of the 5×5 δ-function kernel used to convolve the reference frame (top left) to match a typical science frame (bottom left). Bottom left: a cutout of the same area for a typical science frame in the RX Cam image sequence. Bottom right: residuals after subtraction. All images are displayed using the same logarithmic stretch; colors have been inverted for clarity.

3.3.2 Pipeline Modifications for WFCAM Images

We made a number of modifications to the OS-DIA pipeline to improve its performance on our defocused images. First, we used the coordinates of the center of the reference image to query the TIC to get a list of sources that appeared in the image. However, since the WFCAM images were defocused, there was a consistent offset between the TIC coordinates and the WFCAM initial WCS. We removed this offset by visually identifying the stellar centroids that would capture the stellar flux completely within our photometry apertures, which varied between $26 - 41$ pixels depending on the defocused nature of the Cepheid.

We median-combined all the images of a given Cepheid to generate the reference frame used for subtraction. This differs from the procedure in Oelkers and Stassun (2018, 2019) that only used the first image in the series as the reference image.

We modified the selection procedure to identify stars which could be used to solve for the reference kernel. We only selected stars which had pixel positions farther than at least 100 pixels from the edge, and had photometric uncertainties less than 0.05 mag after an initial execution of aperture photometry on the reference frame. Additionally, we purposefully excluded the Cepheid from the list of stars that could be used for the kernel generation since its variability would likely degrade the quality of the kernel it was used to solve.

Finally, we modified the original OS-DIA light-curve detrending procedure applied to the Cepheids. Normally, this pipeline uses a median-combined subset of 100 stars of similar magnitude to the target star which decreases the photometric dispersion when combined and subtracted from the target light curve. This approach was used to evaluate our photometric precision as discussed in Section 3.3.3. However, we were unable to use this method for the Cepheids as there are few (if any) stars with similar magnitudes in each frame. Instead, we first selected all stars within 250 pixels of the Cepheid as "trend" stars. Next, we subtracted the reference frame magnitude of each trend star from its full light curve, and median-combined the trend light curves with a 2σ clipping to create a reference trend. This reference trend was then subtracted from the light curve of the corresponding Cepheid.

3.3.3 Evaluating the Photometric Precision of Output Light Curves

We characterized the photometric quality of the differenced light curves for stars other than the Cepheids as follows. We first subtracted the mean magnitude of each star in every field from the corresponding detrended light curve and then computed the median absolute value of the resulting offsets, performing iterative 5σ clipping to exclude outliers. The results for one representative field are shown in Figure 3.3. We achieved a photometric precision limit of ~ 0.01 mag for bright ($8 < H < 11$ mag) stars. We investigated whether the achieved photometric precision was in line with expectations by performing aperture photometry on the raw images of the RX Cam field using the corresponding input star list to the pipeline. We determined the S/N of each object taking into account contributions from photon statistics, sky background, and readout noise. As shown by the solid black line in Figure 3.3, the photometric precision expected from S/N considerations closely follows the noise floor. The objects with excess rms ($0.07 - 0.2$ mag for $11.5 < H < 13.3$) are either uncharacterized variables or located near the edges of the reference image, where the quality of the image subtraction and subsequent photometry procedures are less reliable.

In the case of the Cepheids, we phased their light curves adopting the periods listed in Table 3.1 and fit them using templates from Inno et al. (2015)[1] which is linear in amplitude and mean magnitude, and nonlinear in initial phase offset. We adopted a strategy of first searching for the initial phase offset that achieved a global least-squares minimum, simultaneously solving for amplitude and mean magnitude for each trial value of the initial phase. Then, the initial phase offset and parameter uncertainties were fine-tuned using the Gauss–Newton algorithm. This strategy ensures both accuracy and speed. The best fit model amplitudes and initial phase offsets, along with their uncertainties, are listed in Table 3.2.

We used the residuals from the light-curve fitting to estimate a global statistical uncertainty of 0.027 mag for the Cepheid photometry. This larger value relative to the brightest

[1]The template-fitting code is available at https://github.com/wenlong2/Fit2Inno2015.

non-Cepheids in the frame likely arises from our limited ability to detrend the former light curves. Overall, the phase correction uncertainties are dominated by the light-curve-modeling errors, and thus were estimated by the scatter of the light-curve-fitting residuals.

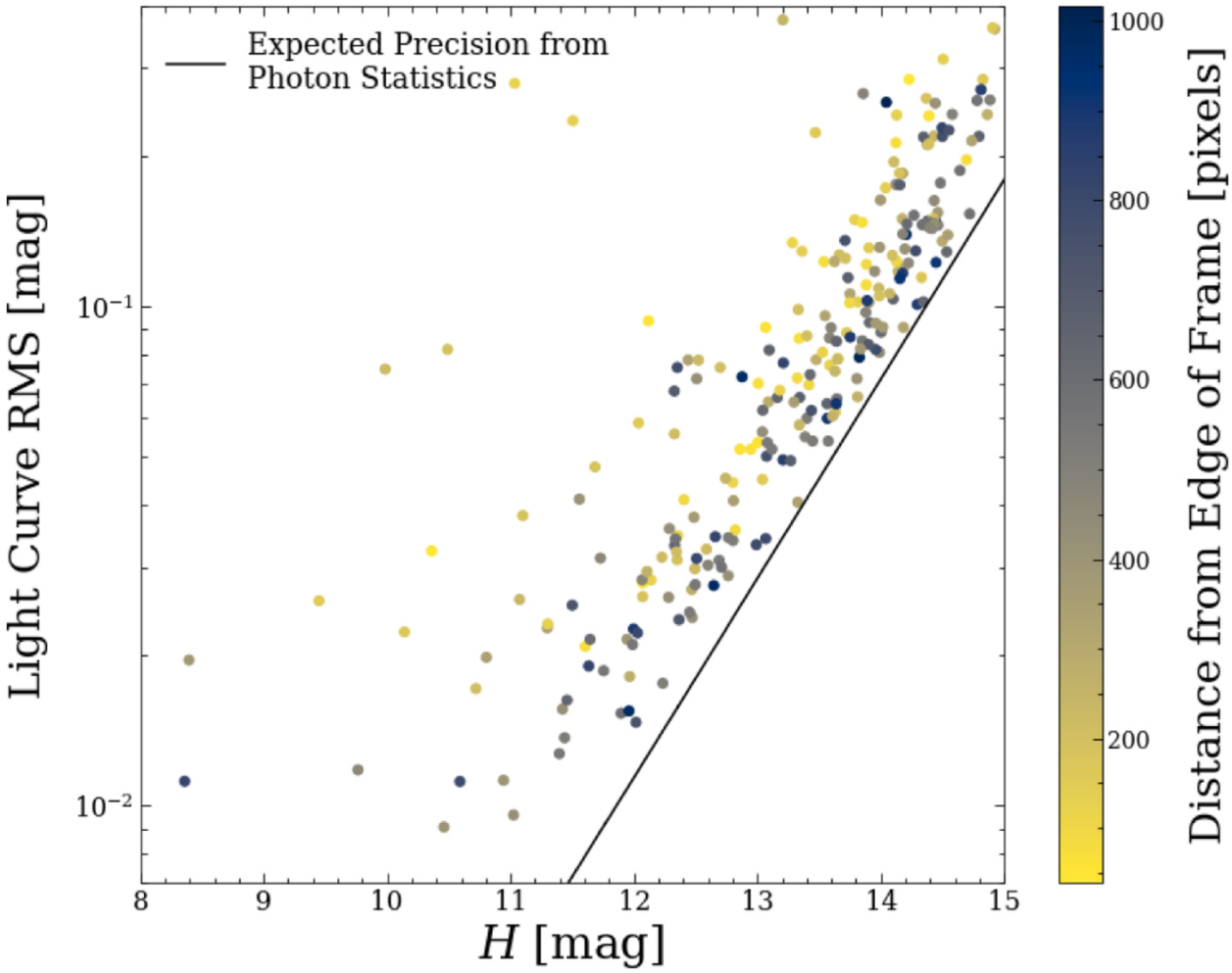

Figure 3.3 Photometric precision of light curves obtained via difference imaging (colored points) and the expected precision from photon statistics (solid line) for a representative field (RX Cam). The color of each point indicates distance from the edge of the frame, showing greater precision in the central area.

Table 3.2. Parameters from Template Fitting of Cepheid Light Curves

Name	Amplitude	Phase Offset
AP Sgr	0.238 ± 0.013	0.032 ± 0.008
BF Oph	0.237 ± 0.017	0.084 ± 0.009
RV Sco	0.226 ± 0.015	0.041 ± 0.008
RX Cam	0.178 ± 0.022	0.049 ± 0.014
SS Sct	0.192 ± 0.005	0.030 ± 0.005
TX Cyg	0.285 ± 0.020	-0.007 ± 0.011
V0386 Cyg	0.259 ± 0.010	0.042 ± 0.004

3.4 Cepheid Light Curves and Phase Corrections

Table 3.3 presents our fully calibrated photometric measurements; observations taken within 2.4 hr were averaged into a single epoch. Figure 3.4 shows the raw, detrended, and phased Cepheid light curves and also includes "postage stamps" of 4 arcsec around each variable.

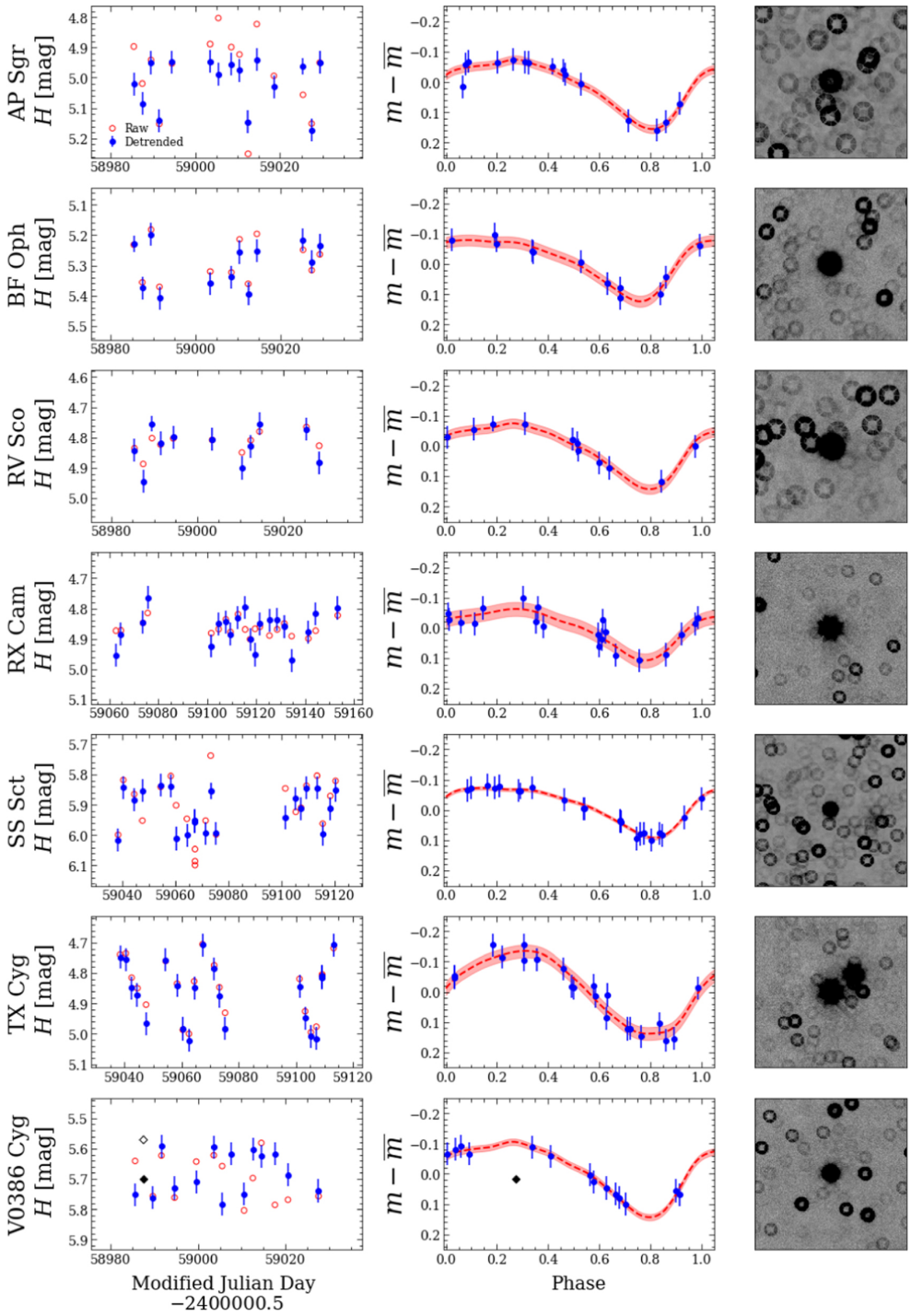

Figure 3.4 Raw (open red circles) and detrended (left) and phased (center) light curves (filled blue circles) and models (dashed red lines), plus reference images (right, 4 arcsec on a side, inverted for clarity) of our target Cepheids. The mean magnitudes used in the left column were taken from 2MASS PSC. Phased light curves are plotted relative to the mean magnitude of each light curve, and the models are shown with 1σ intervals (shaded red regions). Observations taken within 2.4 hr were averaged into a single epoch. Periods were taken from Riess et al. (2021a). The black diamonds in the V0386 Cyg light curves correspond to an epoch that was excluded due to a significant difference in defocused PSF size compared to all other images.

Table 3.3. Cepheid Photometry

Name	MJD[a]	Phase[b]	H [mag][c]
AP Sgr	8985.4918	0.529	5.024
BF Oph	8985.4344	0.197	5.228
RV Sco	8985.4264	0.516	4.858
RX Cam	9062.5855	0.665	4.941
SS Sct	9038.4188	0.805	6.023
TX Cyg	9038.4533	0.221	4.695
V0386 Cyg	8985.6038	0.915	5.761

Note. — (a) JD−2450000.5. (b) based on the periods listed in Table 3.1 and the phase offsets listed in Table 3.2; the overall systematic uncertainty in this parameter for a given Cepheid is provided in the latter table. (c) DIA magnitude + mean 2MASS magnitude from Table 3.1; a statistical uncertainty of 0.027 mag applies to all lines (see §3.3.3). Only a few rows are shown here for guidance; the full version is available in A.3.

3.4.1 Comparison of Derived Cepheid Amplitudes with Previous Studies

We compared three of our Cepheid light curves (V0386 Cyg, TX Cyg, and RX Cam) with those obtained by Monson and Pierce (2011) to provide context into our template fitting and data reduction. We executed a bootstrap simulation sampling from both sets of light curves independently (with replacement) 1000 times. We scaled the amplitude of the Cepheid template (described in Section 3.3.3) during each bootstrap simulation and selected the amplitude which minimized the least-squares residuals of the fit. The results are presented in Figure 3.5.

We found the amplitudes for V0386 Cyg to be 0.25 mag in this work and 0.21 mag from Monson and Pierce (2011), which are consistent within 1.0σ using the photometric uncertainties of the light curves and 1.3σ using the standard deviation of the bootstrap simulations. We found the amplitudes for TX Cyg to be 0.27 mag in this work and 0.31 mag from Monson and Pierce (2011), which are consistent within 1.0σ using the photometric

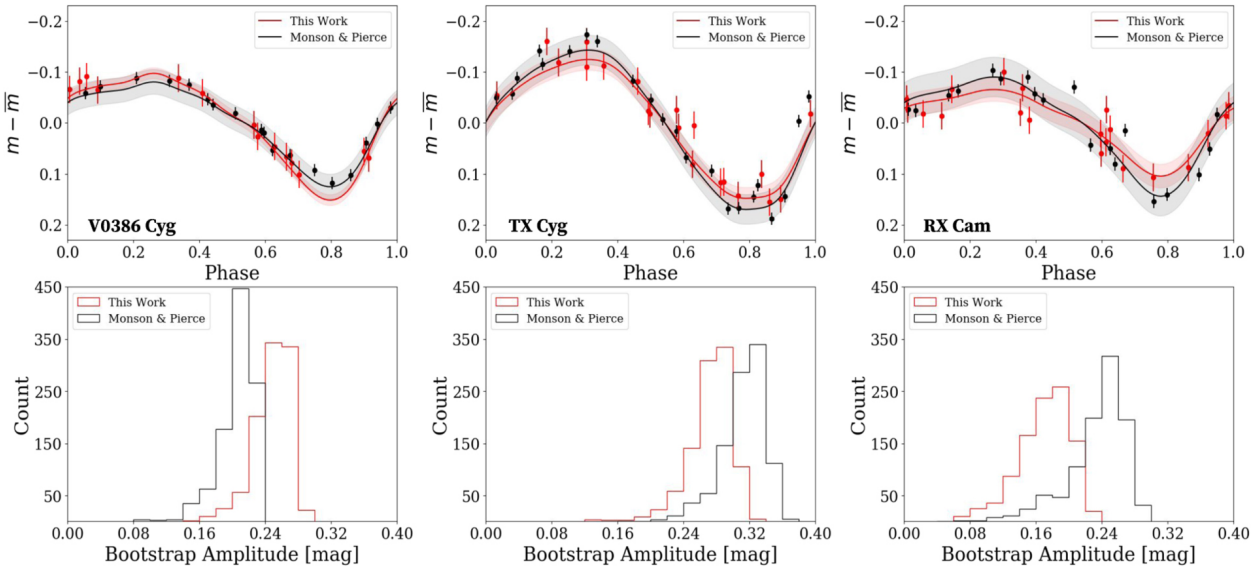

Figure 3.5 Results of the bootstrap procedure to compare Cepheid amplitudes derived from our work (red) and from (Monson and Pierce 2011, black). Top: Binned and phase-folded light curves; solid lines show the best-fit templates. The red and black shaded regions represent the 1σ intervals. Bottom: Results of 1000 bootstrap samplings (with replacement) to estimate the uncertainty on the best-fit amplitudes. We find agreement between the two data sets at the $1.1 - 1.4\sigma$ level.

uncertainties of the light curves and 1.0σ using the standard deviation of the bootstrap simulations. Lastly, we found the amplitudes for RX Cam to be 0.17 mag in this work and 0.23 mag from Monson and Pierce (2011), which are consistent within 1.5σ using the photometric uncertainties of the light curves and 1.4σ using the standard deviation of the bootstrap simulations. We interpret these results as being statistically consistent.

3.4.2 Comparison of Phase Corrections Based on *VI*- and *H*-band Light Curves

We obtained corrections to "mean light" for the random phase HST Wide Field Camera 3 (WFC3) $F160W$ observations of these Cepheids reported in Riess et al. (2021a). One set of corrections was based on V- and I-band light curves from the literature (see Tables 3 and 4 in Riess et al. 2021a) while the other was based on our H-band light curves. The procedure to obtain the phase corrections is described in detail in the Appendix of Riess et al. (2018c), but we briefly summarize the procedure below.

First, any available observations in the $VIJH$ bands that contain epochs close to the HST observations of a given Cepheid are assembled. These bands are used because they are similar in central wavelength and bandpass to the HST WFC3 bands $F555W$, $F814W$, and $F160W$, and thus can be easily transformed. The assembled observations are then combined into a single data set, which is fit with a Fourier series to obtain a model of Cepheid variability. Riess et al. (2018c) consider two models of variability: one where the period is kept constant and another where the period is allowed to vary along with the other model parameters. For the set of phase corrections presented here, the constant period model was used.

The variability model is then used to convert observation times to phase, and a cubic spline (or a Cepheid template if the number of observations is limited) is used to interpolate the light curves in a single band and determine magnitude at the observed phase, m_ϕ. m_ϕ is used to define a phase correction curve $C_\phi = \overline{m} - m_\phi$. The H-band phase was allowed to vary freely and was not shifted relative to the V-band phase. Photometric transformations from Riess et al. (2016) are then used to convert the phase corrections from the ground-based to the HST photometric system.

Figure 3.6 compares the two sets of phase corrections. We find good agreement with the phase corrections based on VI light curves, with a small mean difference of -1 ± 6 mmag.

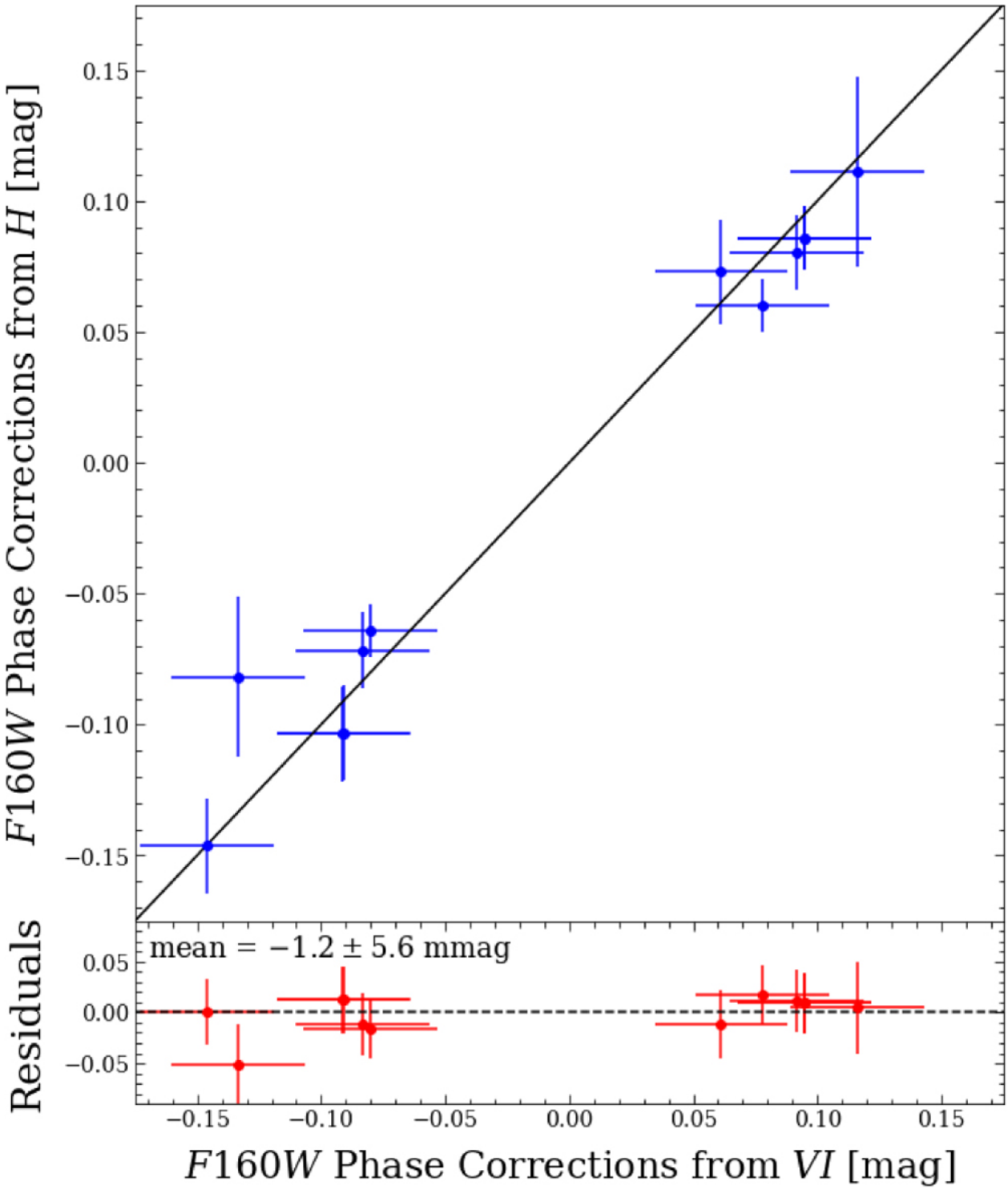

Figure 3.6 Comparison of corrections to "mean light" for the random-phase HST $F160W$ observations of the seven MW Cepheids discussed in this work, derived from ground-based VI and H light curves, respectively

3.5 Summary

We presented H-band light curves of seven MW Cepheids observed as part of the DEHVILS survey. We extracted the light curves using a modified difference-imaging pipeline that has been recently adapted to TESS FFIs and modified to account for the defocused observing mode. We find our adapted pipeline has achieved a photometric precision limit of ~ 0.01 mag. We used the resulting light curves to determine phase corrections for HST $F160W$ observations of these Cepheids and correct the measurements to "mean light." We compared the H-band phase corrections to those obtained using VI-band light curves from the literature and found good agreement, with a mean difference of -1 ± 6 mmag.

Facilities: UKIRT, *HST*

Software: Astropy (Astropy Collaboration et al., 2013, 2018); Project Jupyter (Kluyver et al., 2016); Matplotlib (Hunter, 2007); Numpy (Oliphant, 2006); Pandas (McKinney et al., 2010); Photutils (Bradley et al., 2020); IRAF (Tody, 1986b); SAOImage DS9 (Joye and Mandel, 2003).

4. SUMMARY

Cepheids and Mira variables have enormous utility as extragalactic distance indicators. Detailed characterization of these stars will help us make more precise local measurements of the Hubble constant, which will contribute to resolving the Hubble tension. This dissertation presented two analyses that broadened our understanding of Miras and showed how we can use a novel photometric technique to accurately measure Cepheid variability.

We used optical and NIR observations to carry out a search for Miras in M33. We took advantage of our knowledge of a previously identified sample of M33 Miras and machine learning classifiers to identify 2,916 new Mira candidates. We also identified Mira candidates using the PLRs of Miras and SRVs identified by OGLE in the LMC. We used the machine learning linear PLR for O-rich M33 Miras with the linear PLR for O-rich LMC Miras to obtain a preliminary distance modulus for M33 of $\mu = 24.52 - 23.58 \pm 0.04$ mags. We presented the first empirical measurements of Miras in the LSST photometric bands as well as the first evidence for a first overtone pulsation sequence in the M33 Miras. These results will inform Mira searches in LSST data, which promises an abundance of Miras out to distances and breadth heretofore inaccessible.

We applied difference imaging analysis to observations of seven MW Cepheids to extract their light curves in the H band. These observations were taken in a defocused observing mode, which caused the Cepheid fields to become increasingly crowded and less suitable to typical photometric techniques. We adapted a difference imaging pipeline that was written for images taken by TESS to use with our Cepheid observations. We used the extracted H-band light curves to correct HST observations from random phase to "mean light". We compared the H-based phase corrections to those obtained from VI light curves from the literature and found good agreement, with a mean difference of -1 ± 6 millimag.

REFERENCES

Alam, S., Aubert, M., Avila, S., Balland, C., Bautista, J. E., et al. (2021). Completed SDSS-IV extended Baryon Oscillation Spectroscopic Survey: Cosmological implications from two decades of spectroscopic surveys at the Apache Point Observatory. *Phys. Rev. D*, 103(8):083533.

Alard, C. and Lupton, R. H. (1998). A Method for Optimal Image Subtraction. *ApJ*, 503(1):325–331.

Astropy Collaboration, Price-Whelan, A. M., Sipőcz, B. M., Günther, H. M., Lim, P. L., Crawford, S. M., Conseil, S., Shupe, D. L., Craig, M. W., Dencheva, N., Ginsburg, A., VanderPlas, J. T., Bradley, L. D., Pérez-Suárez, D., de Val-Borro, M., Aldcroft, T. L., Cruz, K. L., Robitaille, T. P., Tollerud, E. J., Ardelean, C., Babej, T., Bach, Y. P., Bachetti, M., Bakanov, A. V., Bamford, S. P., Barentsen, G., Barmby, P., Baumbach, A., Berry, K. L., Biscani, F., Boquien, M., Bostroem, K. A., Bouma, L. G., Brammer, G. B., Bray, E. M., Breytenbach, H., Buddelmeijer, H., Burke, D. J., Calderone, G., Cano Rodríguez, J. L., Cara, M., Cardoso, J. V. M., Cheedella, S., Copin, Y., Corrales, L., Crichton, D., D'Avella, D., Deil, C., Depagne, É., Dietrich, J. P., Donath, A., Droettboom, M., Earl, N., Erben, T., Fabbro, S., Ferreira, L. A., Finethy, T., Fox, R. T., Garrison, L. H., Gibbons, S. L. J., Goldstein, D. A., Gommers, R., Greco, J. P., Greenfield, P., Groener, A. M., Grollier, F., Hagen, A., Hirst, P., Homeier, D., Horton, A. J., Hosseinzadeh, G., Hu, L., Hunkeler, J. S., Ivezić, Ž., Jain, A., Jenness, T., Kanarek, G., Kendrew, S., Kern, N. S., Kerzendorf, W. E., Khvalko, A., King, J., Kirkby, D., Kulkarni, A. M., Kumar, A., Lee, A., Lenz, D., Littlefair, S. P., Ma, Z., Macleod, D. M., Mastropietro, M., McCully, C., Montagnac, S., Morris, B. M., Mueller, M., Mumford, S. J., Muna, D., Murphy, N. A., Nelson, S., Nguyen, G. H., Ninan, J. P., Nöthe, M., Ogaz, S., Oh, S., Parejko, J. K., Parley, N., Pascual, S., Patil, R., Patil, A. A., Plunkett, A. L., Prochaska, J. X., Rastogi, T., Reddy Janga, V., Sabater, J., Sakurikar, P., Seifert, M., Sherbert, L. E., Sherwood-

Taylor, H., Shih, A. Y., Sick, J., Silbiger, M. T., Singanamalla, S., Singer, L. P., Sladen, P. H., Sooley, K. A., Sornarajah, S., Streicher, O., Teuben, P., Thomas, S. W., Tremblay, G. R., Turner, J. E. H., Terrón, V., van Kerkwijk, M. H., de la Vega, A., Watkins, L. L., Weaver, B. A., Whitmore, J. B., Woillez, J., Zabalza, V., and Astropy Contributors (2018). The Astropy Project: Building an Open-science Project and Status of the v2.0 Core Package. *AJ*, 156(3):123.

Astropy Collaboration, Robitaille, T. P., Tollerud, E. J., Greenfield, P., Droettboom, M., Bray, E., Aldcroft, T., Davis, M., Ginsburg, A., Price-Whelan, A. M., Kerzendorf, W. E., Conley, A., Crighton, N., Barbary, K., Muna, D., Ferguson, H., Grollier, F., Parikh, M. M., Nair, P. H., Unther, H. M., Deil, C., Woillez, J., Conseil, S., Kramer, R., Turner, J. E. H., Singer, L., Fox, R., Weaver, B. A., Zabalza, V., Edwards, Z. I., Azalee Bostroem, K., Burke, D. J., Casey, A. R., Crawford, S. M., Dencheva, N., Ely, J., Jenness, T., Labrie, K., Lim, P. L., Pierfederici, F., Pontzen, A., Ptak, A., Refsdal, B., Servillat, M., and Streicher, O. (2013). Astropy: A community Python package for astronomy. *A&A*, 558:A33.

Baker, N. and Kippenhahn, R. (1961). The Pulsations of Models of δ Cephei Stars. *AJ*, 70:278.

Baker, N. H. (1963). Pulsational Instability of Cepheid Models. *AJ*, 68:533.

Battinelli, P. and Demers, S. (2004). Carbon star survey of Local Group galaxies. IX. The spheroidal galaxy NGC 185. *A&A*, 417:479–486.

Battinelli, P. and Demers, S. (2009). Assessment of the near infrared identification of carbon stars. II. The local group galaxies IC 1613 and NGC 3109. *A&A*, 493(3):1075–1080.

Bohlin, R. C. (1996). Spectrophotometric Standards From the Far-UV to the Near-IR on the White Dwarf Flux Scale. *AJ*, 111:1743.

Bono, G., Marconi, M., Cassisi, S., Caputo, F., Gieren, W., and Pietrzynski, G. (2005). Classical Cepheid Pulsation Models. X. The Period-Age Relation. *ApJ*, 621(2):966–977.

Bono, G., Marconi, M., and Stellingwerf, R. F. (1999). Classical Cepheid Pulsation Models.

I. Physical Structure. *ApJS*, 122(1):167–205.

Boulade, O., Charlot, X., Abbon, P., Aune, S., Borgeaud, P., Carton, P.-H., Carty, M., Da Costa, J., Deschamps, H., Desforge, D., Eppellé, D., Gallais, P., Gosset, L., Granelli, R., Gros, M., de Kat, J., Loiseau, D., Ritou, J. ., Roussé, J. Y., Starzynski, P., Vignal, N., and Vigroux, L. G. (2003). MegaCam: the new Canada-France-Hawaii Telescope wide-field imaging camera. In Iye, M. and Moorwood, A. F. M., editors, *Instrument Design and Performance for Optical/Infrared Ground-based Telescopes*, volume 4841 of *Society of Photo-Optical Instrumentation Engineers (SPIE) Conference Series*, pages 72–81.

Boyer, M. L., McQuinn, K. B. W., Groenewegen, M. A. T., Zijlstra, A. A., Whitelock, P. A., van Loon, J. T., Sonneborn, G., Sloan, G. C., Skillman, E. D., Meixner, M., McDonald, I., Jones, O. C., Javadi, A., Gehrz, R. D., Britavskiy, N., and Bonanos, A. Z. (2017). An Infrared Census of DUST in Nearby Galaxies with Spitzer (DUSTiNGS). IV. Discovery of High-redshift AGB Analogs. *ApJ*, 851(2):152.

Bradley, L., Sipőcz, B., Robitaille, T., Tollerud, E., Vinícius, Z., Deil, C., Barbary, K., Wilson, T. J., Busko, I., Günther, H. M., Cara, M., Conseil, S., Bostroem, A., Droettboom, M., Bray, E. M., Bratholm, L. A., Lim, P. L., Barentsen, G., Craig, M., Pascual, S., Perren, G., Greco, J., Donath, A., de Val-Borro, M., Kerzendorf, W., Bach, Y. P., Weaver, B. A., D'Eugenio, F., Souchereau, H., and Ferreira, L. (2020). astropy/photutils: 1.0.0.

Carroll, B. W. and Ostlie, D. A. (1996). *An Introduction to Modern Astrophysics*.

Casali, M., Adamson, A., Alves de Oliveira, C., Almaini, O., Burch, K., Chuter, T., Elliot, J., Folger, M., Foucaud, S., Hambly, N., Hastie, M., Henry, D., Hirst, P., Irwin, M., Ives, D., Lawrence, A., Laidlaw, K., Lee, D., Lewis, J., Lunney, D., McLay, S., Montgomery, D., Pickup, A., Read, M., Rees, N., Robson, I., Sekiguchi, K., Vick, A., Warren, S., and Woodward, B. (2007). The UKIRT wide-field camera. *A&A*, 467(2):777–784.

Chambers, K. C., Magnier, E. A., Metcalfe, N., Flewelling, H. A., Huber, M. E., Waters, C. Z., Denneau, L., Draper, P. W., Farrow, D., and Finkbeiner, D. P. (2016). The Pan-STARRS1 Surveys. *arXiv e-prints*, page arXiv:1612.05560.

Cioni, M. R. L. and Habing, H. J. (2003). AGB stars in the Magellanic Clouds. I. The C/M ratio. *A&A*, 402:133–140.

Cioni, M. R. L., Irwin, M., Ferguson, A. M. N., McConnachie, A., Conn, B. C., Huxor, A., Ibata, R., Lewis, G., and Tanvir, N. (2008). AGB stars as tracers of metallicity and mean age across M 33. *A&A*, 487(1):131–146.

Dye, S., Lawrence, A., Read, M. A., Fan, X., Kerr, T., Varricatt, W., Furnell, K. E., Edge, A. C., Irwin, M., Hambly, N., Lucas, P., Almaini, O., Chambers, K., Green, R., Hewett, P., Liu, M. C., McGreer, I., Best, W., Zhang, Z., Sutorius, E., Froebrich, D., Magnier, E., Hasinger, G., Lederer, S. M., Bold, M., and Tedds, J. A. (2018). The UKIRT Hemisphere Survey: definition and J-band data release. *MNRAS*, 473(4):5113–5125.

El Eid, M. F. (2016). Introduction to Asymptotic Giant Branch Stars. In *Journal of Physics Conference Series*, volume 703 of *Journal of Physics Conference Series*, page 012005.

ESA (1997). *The HIPPARCOS and TYCHO catalogues. Astrometric and photometric star catalogues derived from the ESA HIPPARCOS Space Astrometry Mission*, volume 1200 of *ESA Special Publication*.

Eyer, L. and Mowlavi, N. (2008). Variable stars across the observational HR diagram. In *Journal of Physics Conference Series*, volume 118 of *Journal of Physics Conference Series*, page 012010.

Freedman, W. L., Madore, B. F., Gibson, B. K., Ferrarese, L., Kelson, D. D., Sakai, S., Mould, J. R., Kennicutt, Robert C., J., Ford, H. C., Graham, J. A., Huchra, J. P., Hughes, S. M. G., Illingworth, G. D., Macri, L. M., and Stetson, P. B. (2001). Final Results from the Hubble Space Telescope Key Project to Measure the Hubble Constant. *ApJ*, 553(1):47–72.

Freytag, B., Liljegren, S., and Höfner, S. (2017). Global 3D radiation-hydrodynamics models of AGB stars. Effects of convection and radial pulsations on atmospheric structures. *A&A*, 600:A137.

Friedmann, A. (1922). Über die Krümmung des Raumes. *Zeitschrift fur Physik*, 10:377–386.

Frogel, J. A., Persson, S. E., and Cohen, J. G. (1980). Luminosities and temperatures of the reddest stars in three LMC clusters. *ApJ*, 239:495–501.

Gaia Collaboration et al. (2016). The Gaia mission. *A&A*, 595:A1.

Gaia Collaboration et al. (2021). Gaia Early Data Release 3. Summary of the contents and survey properties. *A&A*, 649:A1.

Gieren, W., Górski, M., Pietrzyński, G., Konorski, P., Suchomska, K., Graczyk, D., Pilecki, B., Bresolin, F., Kudritzki, R.-P., Storm, J., Karczmarek, P., Gallenne, A., Calderón, P., and Geisler, D. (2013). The Araucaria Project. A Distance Determination to the Local Group Spiral M33 from Near-infrared Photometry of Cepheid Variables. *ApJ*, 773(1):69.

Glass, I. S. and Evans, T. L. (1981). A period-luminosity relation for Mira variables in the Large Magellanic Cloud. *Nature*, 291(5813):303–304.

Goodricke, J. (1786). A Series of Observations on, and a Discovery of, the Period of the Variation of the Light of the Star Marked δ by Bayer, Near the Head of Cepheus. In a Letter from John Goodricke, Esq. to Nevil Maskelyne, D. D. F. R. S. and Astronomer Royal. *Philosophical Transactions of the Royal Society of London Series I*, 76:48–61.

Hamren, K. M., Rockosi, C. M., Guhathakurta, P., Boyer, M. L., Smith, G. H., Dalcanton, J. J., Gregersen, D., Seth, A. C., Lewis, A. R., Williams, B. F., Toloba, E., Girardi, L., Dorman, C. E., Gilbert, K. M., and Weisz, D. R. (2015). A Spectroscopic and Photometric Exploration of the C/M Ratio in the Disk of M31. *ApJ*, 810(1):60.

Hartman, J. D., Bersier, D., Stanek, K. Z., Beaulieu, J. P., Kaluzny, J., Marquette, J. B., Stetson, P. B., and Schwarzenberg-Czerny, A. (2006). Deep Canada-France-Hawaii Telescope photometric survey of the entire M33 galaxy - I. Catalogue of 36000 variable point sources. *MNRAS*, 371(3):1405–1417.

He, S., Lin, Z., Yuan, W., Macri, L. M., and Huang, J. Z. (2021). Simultaneous inference of periods and period-luminosity relations for Mira variable stars. *arXiv e-prints*, page arXiv:2101.02938.

He, S., Yuan, W., Huang, J. Z., Long, J., and Macri, L. M. (2016). Period Estimation for

Sparsely-sampled Quasi-periodic Light Curves Applied to Miras. *AJ*, 152(6):164.

Hertzsprung, E. (1926). On the relation between period and form of the light-curve of variable stars of the δ Cephei type. , 3:115.

Hinkle, K. H., Lebzelter, T., and Straniero, O. (2016). Carbon and Oxygen Isotopic Ratios for Nearby Miras. *ApJ*, 825(1):38.

Hodgkin, S. T., Irwin, M. J., Hewett, P. C., and Warren, S. J. (2009). The UKIRT wide field camera ZYJHK photometric system: calibration from 2MASS. *MNRAS*, 394(2):675–692.

Hoffleit, D. (1997). History of the Discovery of Mira Stars. , 25(2):115–136.

Höfner, S. (2008). Winds of M-type AGB stars driven by micron-sized grains. *A&A*, 491(2):L1–L4.

Huang, C. D., Riess, A. G., Hoffmann, S. L., Klein, C., Bloom, J., Yuan, W., Macri, L. M., Jones, D. O., Whitelock, P. A., Casertano, S., and Anderson, R. I. (2018). A Near-infrared Period-Luminosity Relation for Miras in NGC 4258, an Anchor for a New Distance Ladder. *ApJ*, 857(1):67.

Huang, C. D., Riess, A. G., Yuan, W., Macri, L. M., Zakamska, N. L., Casertano, S., Whitelock, P. A., Hoffmann, S. L., Filippenko, A. V., and Scolnic, D. (2020). Hubble Space Telescope Observations of Mira Variables in the SN Ia Host NGC 1559: An Alternative Candle to Measure the Hubble Constant. *ApJ*, 889(1):5.

Hubble, E. (1929). A Relation between Distance and Radial Velocity among Extra-Galactic Nebulae. *Contributions from the Mount Wilson Observatory*, 3:23–28.

Hubble, E. and Humason, M. L. (1931). The Velocity-Distance Relation among Extra-Galactic Nebulae. *ApJ*, 74:43.

Hunter, J. D. (2007). Matplotlib: A 2d graphics environment. *Computing in science & engineering*, 9(3):90–95.

Iben, I., J. and Renzini, A. (1983). Asymptotic giant branch evolution and beyond. *ARA&A*, 21:271–342.

Inno, L., Matsunaga, N., Romaniello, M., Bono, G., Monson, A., Ferraro, I., Iannicola,

G., Persson, E., Buonanno, R., Freedman, W., Gieren, W., Groenewegen, M. A. T., Ita, Y., Laney, C. D., Lemasle, B., Madore, B. F., Nagayama, T., Nakada, Y., Nonino, M., Pietrzyński, G., Primas, F., Scowcroft, V., Soszyński, I., Tanabé, T., and Udalski, A. (2015). New NIR light-curve templates for classical Cepheids. *A&A*, 576:A30.

Ita, Y. and Matsunaga, N. (2011). Period-magnitude relation of Mira-like variables in the Large Magellanic Cloud as a tool to understanding circumstellar extinction. *MNRAS*, 412(4):2345–2352.

Ita, Y., Tanabé, T., Matsunaga, N., Nakajima, Y., Nagashima, C., Nagayama, T., Kato, D., Kurita, M., Nagata, T., Sato, S., Tamura, M., Nakaya, H., and Nakada, Y. (2004). Variable stars in the Magellanic Clouds: results from OGLE and SIRIUS. *MNRAS*, 347(3):720–728.

Ivezić, Ž., Kahn, S. M., Tyson, J. A., et al. (2019). LSST: From Science Drivers to Reference Design and Anticipated Data Products. *ApJ*, 873(2):111.

Iwanek, P., Kozłowski, S., Gromadzki, M., Soszyński, I., Wrona, M., Skowron, J., Ratajczak, M., Udalski, A., Szymański, M. K., Pietrukowicz, P., Ulaczyk, K., Poleski, R., Mróz, P., Skowron, D. M., and Rybicki, K. (2021). Multiwavelength Properties of Miras. *ApJS*, 257(2):23.

Javadi, A., Saberi, M., van Loon, J. T., Khosroshahi, H., Golabatooni, N., and Mirtorabi, M. T. (2015). The UK Infrared Telescope M33 monitoring project - IV. Variable red giant stars across the galactic disc. *MNRAS*, 447(4):3973–3991.

Jones, E., Oliphant, T., Peterson, P., et al. (2001). SciPy: Open source scientific tools for Python. [Online; accessed].

Joye, W. A. and Mandel, E. (2003). New Features of SAOImage DS9. In Payne, H. E., Jedrzejewski, R. I., and Hook, R. N., editors, *Astronomical Data Analysis Software and Systems XII*, volume 295 of *Astronomical Society of the Pacific Conference Series*, page 489.

Karakas, A. I. and Lattanzio, J. C. (2014). The Dawes Review 2: Nucleosynthesis and Stellar Yields of Low- and Intermediate-Mass Single Stars. , 31:e030.

Kato, D., Nagashima, C., Nagayama, T., Kurita, M., Koerwer, J. F., Kawai, T., Yamamuro, T., Zenno, T., Nishiyama, S., Baba, D., Kadowaki, R., Haba, Y., Hatano, H., Shimizu, H., Nishimura, M., Nagata, T., Sato, S., Murai, Y., Kawazu, T., Nakajima, Y., Nakaya, H., Kandori, R., Kusakabe, N., Ishihara, A., Kaneyasu, N., Hashimoto, J., Tamura, M., Tanabé, T., Ita, Y., Matsunaga, N., Nakada, Y., Sugitani, K., Wakamatsu, K.-I., Glass, I. S., Feast, M. W., Menzies, J. W., Whitelock, P. A., Fourie, P., Stoffels, J., Evans, G. P., and Hasegawa, T. (2007). The IRSF Magellanic Clouds Point Source Catalog. *PASJ*, 59:615–641.

Kholopov, P. N., Samus, N. N., Kazarovets, E. V., and Perova, N. B. (1985). The 67th Name-List of Variable Stars. *Information Bulletin on Variable Stars*, 2681:1.

Klagyivik, P. and Szabados, L. (2009). Observational studies of Cepheid amplitudes. I. Period-amplitude relationships for Galactic Cepheids and interrelation of amplitudes. *A&A*, 504(3):959–972.

Kluyver, T., Ragan-Kelley, B., Pérez, F., Granger, B., Bussonnier, M., Frederic, J., Kelley, K., Hamrick, J., Grout, J., Corlay, S., Ivanov, P., Avila, D., Abdalla, S., and Willing, C. (2016). Jupyter notebooks – a publishing format for reproducible computational workflows. In Loizides, F. and Schmidt, B., editors, *Positioning and Power in Academic Publishing: Players, Agents and Agendas*, pages 87 – 90. IOS Press.

Kobayashi, C., Karakas, A. I., and Umeda, H. (2011). The evolution of isotope ratios in the Milky Way Galaxy. *MNRAS*, 414(4):3231–3250.

Lattanzio, J. C. (2002). AGB stars: summary and warning. *New Astron. Rev.*, 46(8-10):469–474.

Lawrence, A., Warren, S. J., Almaini, O., Edge, A. C., Hambly, N. C., Jameson, R. F., Lucas, P., Casali, M., Adamson, A., Dye, S., Emerson, J. P., Foucaud, S., Hewett, P., Hirst, P., Hodgkin, S. T., Irwin, M. J., Lodieu, N., McMahon, R. G., Simpson, C., Smail, I., Mortlock, D., and Folger, M. (2007). The UKIRT Infrared Deep Sky Survey (UKIDSS). *MNRAS*, 379(4):1599–1617.

Leavitt, H. S. (1908). 1777 variables in the Magellanic Clouds. *Annals of Harvard College Observatory*, 60:87–108.3.

Leavitt, H. S. and Pickering, E. C. (1912). Periods of 25 Variable Stars in the Small Magellanic Cloud. *Harvard College Observatory Circular*, 173:1–3.

Lemaître, G. (1927). Un Univers homogène de masse constante et de rayon croissant rendant compte de la vitesse radiale des nébuleuses extra-galactiques. *Annales de la Société Scientifique de Bruxelles*, 47:49–59.

Lindegren, L., Bastian, U., Biermann, M., Bombrun, A., de Torres, A., Gerlach, E., Geyer, R., Hernández, J., Hilger, T., Hobbs, D., Klioner, S. A., Lammers, U., McMillan, P. J., Ramos-Lerate, M., Steidelmüller, H., Stephenson, C. A., and van Leeuwen, F. (2021a). Gaia Early Data Release 3. Parallax bias versus magnitude, colour, and position. *A&A*, 649:A4.

Lindegren, L., Hernández, J., Bombrun, A., Klioner, S., Bastian, U., et al. (2018). Gaia Data Release 2. The astrometric solution. *A&A*, 616:A2.

Lindegren, L., Klioner, S. A., Hernández, J., Bombrun, A., Ramos-Lerate, M., et al. (2021b). Gaia Early Data Release 3. The astrometric solution. *A&A*, 649:A2.

Macri, L. M., Ngeow, C.-C., Kanbur, S. M., Mahzooni, S., and Smitka, M. T. (2015). Large Magellanic Cloud Near-Infrared Synoptic Survey. I. Cepheid Variables and the Calibration of the Leavitt Law. *AJ*, 149(4):117.

Macri, L. M., Stanek, K. Z., Sasselov, D. D., Krockenberger, M., and Kaluzny, J. (2001). DIRECT Distances to Nearby Galaxies Using Detached Eclipsing Binaries and Cepheids. VI. Variables in the Central Part of M33. *AJ*, 121(2):870–890.

Madore, B. F. (1982). The period-luminosity relation. IV - Intrinsic relations and reddenings for the Large Magellanic Cloud Cepheids. *ApJ*, 253:575–579.

Majaess, D., Turner, D., Gieren, W., Berdnikov, L., and Lane, D. (2013). On the metallicity dependence of classical Cepheid light amplitudes. , 344(2):381–388.

Mancino, S., Romaniello, M., Anderson, R. I., and Kudritzki, R. P. (2021). Towards Precise

and Accurate Cepheid Chemical Abundances for a 1% H_0 Measurement: Temperature Determination. In Kinemuchi, K., Lovekin, C., Neilson, H., and Vivas, K., editors, *RR Lyrae/Cepheid 2019: Frontiers of Classical Pulsators*, volume 529 of *Astronomical Society of the Pacific Conference Series*, page 265.

McDonald, I. and Trabucchi, M. (2019). The onset of the AGB wind tied to a transition between sequences in the period-luminosity diagram. *MNRAS*, 484(4):4678–4682.

McKinney, W. et al. (2010). Data structures for statistical computing in python. In van der Walt, S. and Millman, J., editors, *Proceedings of the 9th Python in Science Conference*, volume 445, pages 51–56. Austin, TX.

Menzies, J. W., Whitelock, P. A., and Feast, M. W. (2015). The Local Group Galaxy IC 1613 and its asymptotic giant branch variables. *MNRAS*, 452(1):910–923.

Menzies, J. W., Whitelock, P. A., Feast, M. W., and Matsunaga, N. (2019). Luminous AGB variables in the dwarf irregular galaxy, NGC 3109. *MNRAS*, 483(4):5150–5165.

Mink, D. J. (1999). WCSTools: an Image Astrometry Toolkit. In Mehringer, D. M., Plante, R. L., and Roberts, D. A., editors, *Astronomical Data Analysis Software and Systems VIII*, volume 172 of *Astronomical Society of the Pacific Conference Series*, page 498.

Monson, A. J. and Pierce, M. J. (2011). Near-infrared (JHK) Photometry of 131 Northern Galactic Classical Cepheids. *ApJS*, 193(1):12.

Mordelet, F. and Vert, J.-P. (2014). A bagging svm to learn from positive and unlabeled examples. *Pattern Recognition Letters*, 37:201–209. Partially Supervised Learning for Pattern Recognition.

Mould, J. and Aaronson, M. (1980). The extended giant branches of intermediate age globular clusters in the Magellanic Clouds. *ApJ*, 240:464–477.

Oelkers, R. J., Macri, L. M., Wang, L., Ashley, M. C. B., Cui, X., Feng, L.-L., Gong, X., Lawrence, J. S., Qiang, L., Luong-Van, D., Pennypacker, C. R., Yang, H., Yuan, X., York, D. G., Zhou, X., and Zhu, Z. (2015). Difference Image Analysis of Defocused Observations With CSTAR. *AJ*, 149(2):50.

Oelkers, R. J. and Stassun, K. G. (2018). Precision Light Curves from TESS Full-frame Images: A Different Imaging Approach. *AJ*, 156(3):132.

Oelkers, R. J. and Stassun, K. G. (2019). Light Curves for All Stars Observed in TESS Full-frame Images: Sector 1 and Beyond. *Research Notes of the American Astronomical Society*, 3(1):8.

Oliphant, T. E. (2006). *A guide to NumPy*, volume 1. Trelgol Publishing USA.

Pellerin, A. and Macri, L. M. (2011). The M 33 Synoptic Stellar Survey. I. Cepheid Variables. *ApJS*, 193(2):26.

Percy, J. R. (1984). Astronomers Celebrate Cepheid Bicentenary. , 78:L76.

Percy, J. R. (2007). *Understanding Variable Stars*.

Persson, S. E., Madore, B. F., Krzemiński, W., Freedman, W. L., Roth, M., and Murphy, D. C. (2004). New Cepheid Period-Luminosity Relations for the Large Magellanic Cloud: 92 Near-Infrared Light Curves. *AJ*, 128(5):2239–2264.

Pietrzyński, G., Graczyk, D., Gallenne, A., Gieren, W., Thompson, I. B., Pilecki, B., Karczmarek, P., Górski, M., Suchomska, K., Taormina, M., Zgirski, B., Wielgórski, P., Kołaczkowski, Z., Konorski, P., Villanova, S., Nardetto, N., Kervella, P., Bresolin, F., Kudritzki, R. P., Storm, J., Smolec, R., and Narloch, W. (2019). A distance to the Large Magellanic Cloud that is precise to one per cent. *Nature*, 567(7747):200–203.

Planck Collaboration (2020). Planck 2018 results. VI. Cosmological parameters. *A&A*, 641:A6.

Puget, P., Stadler, E., Doyon, R., Gigan, P., Thibault, S., Luppino, G., Barrick, G., Benedict, T., Forveille, T., Rambold, W., Thomas, J., Vermeulen, T., Ward, J., Beuzit, J.-L., Feautrier, P., Magnard, Y., Mella, G., Preis, O., Vallee, P., Wang, S.-y., Lin, C.-J., Hall, D. N., and Hodapp, K. W. (2004). *WIRCam: the infrared wide-field camera for the Canada-France-Hawaii Telescope*, volume 5492 of *Society of Photo-Optical Instrumentation Engineers (SPIE) Conference Series*, pages 978–987.

Rejkuba, M. (2004). The distance to the giant elliptical galaxy NGC 5128. *A&A*, 413:903–

912.

Ren, Y., Jiang, B., Yang, M., Wang, T., Jian, M., and Ren, T. (2021). Red Supergiants in M31 and M33. I. The Complete Sample. *ApJ*, 907(1):18.

Ricker, G. R., Winn, J. N., Vanderspek, R., Latham, D. W., Bakos, G. Á., Bean, J. L., Berta-Thompson, Z. K., Brown, T. M., Buchhave, L., Butler, N. R., Butler, R. P., Chaplin, W. J., Charbonneau, D., Christensen-Dalsgaard, J., Clampin, M., Deming, D., Doty, J., De Lee, N., Dressing, C., Dunham, E. W., Endl, M., Fressin, F., Ge, J., Henning, T., Holman, M. J., Howard, A. W., Ida, S., Jenkins, J., Jernigan, G., Johnson, J. A., Kaltenegger, L., Kawai, N., Kjeldsen, H., Laughlin, G., Levine, A. M., Lin, D., Lissauer, J. J., MacQueen, P., Marcy, G., McCullough, P. R., Morton, T. D., Narita, N., Paegert, M., Palle, E., Pepe, F., Pepper, J., Quirrenbach, A., Rinehart, S. A., Sasselov, D., Sato, B., Seager, S., Sozzetti, A., Stassun, K. G., Sullivan, P., Szentgyorgyi, A., Torres, G., Udry, S., and Villasenor, J. (2014). Transiting Exoplanet Survey Satellite (TESS). In Oschmann, Jacobus M., J., Clampin, M., Fazio, G. G., and MacEwen, H. A., editors, *Space Telescopes and Instrumentation 2014: Optical, Infrared, and Millimeter Wave*, volume 9143 of *Society of Photo-Optical Instrumentation Engineers (SPIE) Conference Series*, page 914320.

Riebel, D., Meixner, M., Fraser, O., Srinivasan, S., Cook, K., and Vijh, U. (2010). Infrared Period-Luminosity Relations of Evolved Variable Stars in the Large Magellanic Cloud. *ApJ*, 723(2):1195–1209.

Riess, A. G., Casertano, S., Yuan, W., Bowers, J. B., Macri, L., Zinn, J. C., and Scolnic, D. (2021a). Cosmic Distances Calibrated to 1% Precision with Gaia EDR3 Parallaxes and Hubble Space Telescope Photometry of 75 Milky Way Cepheids Confirm Tension with ΛCDM. *ApJ*, 908(1):L6.

Riess, A. G., Casertano, S., Yuan, W., Macri, L., Anderson, J., MacKenty, J. W., Bowers, J. B., Clubb, K. I., Filippenko, A. V., Jones, D. O., and Tucker, B. E. (2018a). New Parallaxes of Galactic Cepheids from Spatially Scanning the Hubble Space Telescope: Implications for the Hubble Constant. *ApJ*, 855(2):136.

Riess, A. G., Casertano, S., Yuan, W., Macri, L., Bucciarelli, B., Lattanzi, M. G., MacKenty, J. W., Bowers, J. B., Zheng, W., Filippenko, A. V., Huang, C., and Anderson, R. I. (2018b). Milky Way Cepheid Standards for Measuring Cosmic Distances and Application to Gaia DR2: Implications for the Hubble Constant. *ApJ*, 861(2):126.

Riess, A. G., Casertano, S., Yuan, W., Macri, L., Bucciarelli, B., Lattanzi, M. G., MacKenty, J. W., Bowers, J. B., Zheng, W., Filippenko, A. V., Huang, C., and Anderson, R. I. (2018c). Milky Way Cepheid Standards for Measuring Cosmic Distances and Application to Gaia DR2: Implications for the Hubble Constant. *ApJ*, 861(2):126.

Riess, A. G., Casertano, S., Yuan, W., Macri, L. M., and Scolnic, D. (2019). Large Magellanic Cloud Cepheid Standards Provide a 1% Foundation for the Determination of the Hubble Constant and Stronger Evidence for Physics beyond ΛCDM. *ApJ*, 876(1):85.

Riess, A. G., Macri, L., Casertano, S., Sosey, M., Lampeitl, H., Ferguson, H. C., Filippenko, A. V., Jha, S. W., Li, W., Chornock, R., and Sarkar, D. (2009). A Redetermination of the Hubble Constant with the Hubble Space Telescope from a Differential Distance Ladder. *ApJ*, 699(1):539–563.

Riess, A. G., Macri, L. M., Hoffmann, S. L., Scolnic, D., Casertano, S., Filippenko, A. V., Tucker, B. E., Reid, M. J., Jones, D. O., Silverman, J. M., Chornock, R., Challis, P., Yuan, W., Brown, P. J., and Foley, R. J. (2016). A 2.4% Determination of the Local Value of the Hubble Constant. *ApJ*, 826(1):56.

Riess, A. G., Yuan, W., Casertano, S., Macri, L. M., and Scolnic, D. (2020). The Accuracy of the Hubble Constant Measurement Verified through Cepheid Amplitudes. *ApJ*, 896(2):L43.

Riess, A. G., Yuan, W., Macri, L. M., Scolnic, D., Brout, D., Casertano, S., Jones, D. O., Murakami, Y., Breuval, L., Brink, T. G., Filippenko, A. V., Hoffmann, S., Jha, S. W., Kenworthy, W. D., Mackenty, J., Stahl, B. E., and Zheng, W. (2021b). A Comprehensive Measurement of the Local Value of the Hubble Constant with 1 km/s/Mpc Uncertainty from the Hubble Space Telescope and the SH0ES Team. *arXiv e-prints*, page arXiv:2112.04510.

Riess, A. G., Yuan, W., Macri, L. M., Scolnic, D., Brout, D., Casertano, S., Jones, D. O., Murakami, Y., Breuval, L., Brink, T. G., Filippenko, A. V., Hoffmann, S., Jha, S. W., Kenworthy, W. D., Mackenty, J., Stahl, B. E., and Zheng, W. (2021c). A Comprehensive Measurement of the Local Value of the Hubble Constant with 1 km/s/Mpc Uncertainty from the Hubble Space Telescope and the SH0ES Team. *arXiv e-prints*, page arXiv:2112.04510.

Robertson, B. S. C. and Feast, M. W. (1981). The bolometric, infrared and visual absolute magnitudes of mira variables. *MNRAS*, 196:111–120.

Sarajedini, A. (2021). A differential RR Lyrae line-of-sight distance between M31 and M33. *MNRAS*, 508(2):3035–3044.

Schlafly, E. F. and Finkbeiner, D. P. (2011). Measuring Reddening with Sloan Digital Sky Survey Stellar Spectra and Recalibrating SFD. *ApJ*, 737(2):103.

Singh, S. (2004). *Big bang: The most important scientific discovery of all time and why you need to know about it.* HarperCollins.

Skrutskie, M. F., Cutri, R. M., Stiening, R., Weinberg, M. D., Schneider, S., Carpenter, J. M., Beichman, C., Capps, R., Chester, T., Elias, J., Huchra, J., Liebert, J., Lonsdale, C., Monet, D. G., Price, S., Seitzer, P., Jarrett, T., Kirkpatrick, J. D., Gizis, J. E., Howard, E., Evans, T., Fowler, J., Fullmer, L., Hurt, R., Light, R., Kopan, E. L., Marsh, K. A., McCallon, H. L., Tam, R., Van Dyk, S., and Wheelock, S. (2006). The Two Micron All Sky Survey (2MASS). *AJ*, 131(2):1163–1183.

Soszyński, I., Poleski, R., Udalski, A., Szymańki, M. K., Kubiak, M., Pietrzyński, G., Wyrzykowski, Ł., Szewczyk, O., and Ulaczyk, K. (2008). The Optical Gravitational Lensing Experiment. The OGLE-III Catalog of Variable Stars. I. Classical Cepheids in the Large Magellanic Cloud. *Acta Astron.*, 58:163–185.

Soszyński, I., Udalski, A., Kubiak, M., Szymański, M., Pietrzyński, G., Żebruń, K., Szewczyk, O., and Wyrzykowski, Ł. (2004). The Optical Gravitational Lensing Experiment. Small Amplitude Variable Red Giants in the Magellanic Clouds. *Acta Astron.*, 54:129–152.

Soszyński, I., Udalski, A., Pietrukowicz, P., Szymański, M. K., Kubiak, M., Pietrzyński, G., Wyrzykowski, Ł., Ulaczyk, K., Poleski, R., and Kozłowski, S. (2011a). The Optical Gravitational Lensing Experiment. The OGLE-III Catalog of Variable Stars. XIV. Classical and TypeII Cepheids in the Galactic Bulge. *Acta Astron.*, 61(4):285–301.

Soszyński, I., Udalski, A., Szymański, M. K., Kubiak, M., Pietrzyński, G., Wyrzykowski, Ł., Szewczyk, O., Ulaczyk, K., and Poleski, R. (2009a). The Optical Gravitational Lensing Experiment. The OGLE-III Catalog of Variable Stars. IV. Long-Period Variables in the Large Magellanic Cloud. *Acta Astron.*, 59(3):239–253.

Soszyński, I., Udalski, A., Szymański, M. K., Kubiak, M., Pietrzyński, G., Wyrzykowski, Ł., Szewczyk, O., Ulaczyk, K., and Poleski, R. (2009b). The Optical Gravitational Lensing Experiment. The OGLE-III Catalog of Variable Stars. IV. Long-Period Variables in the Large Magellanic Cloud. *Acta Astron.*, 59:239–253.

Soszyński, I., Udalski, A., Szymański, M. K., Kubiak, M., Pietrzyński, G., Wyrzykowski, Ł., Ulaczyk, K., Poleski, R., Kozłowski, S., and Pietrukowicz, P. (2011b). The Optical Gravitational Lensing Experiment. The OGLE-III Catalog of Variable Stars. XIII. Long-Period Variables in the Small Magellanic Cloud. *Acta Astron.*, 61(3):217–230.

Soszyński, I., Udalski, A., Szymański, M. K., Kubiak, M., Pietrzyński, G., Wyrzykowski, Ł., Ulaczyk, K., Poleski, R., Kozłowski, S., Pietrukowicz, P., and Skowron, J. (2013). The Optical Gravitational Lensing Experiment. The OGLE-III Catalog of Variable Stars. XV. Long-Period Variables in the Galactic Bulge. *Acta Astron.*, 63(1):21–36.

Stassun, K. G., Oelkers, R. J., Pepper, J., Paegert, M., De Lee, N., Torres, G., Latham, D. W., Charpinet, S., Dressing, C. D., Huber, D., Kane, S. R., Lépine, S., Mann, A., Muirhead, P. S., Rojas-Ayala, B., Silvotti, R., Fleming, S. W., Levine, A., and Plavchan, P. (2018). The TESS Input Catalog and Candidate Target List. *AJ*, 156(3):102.

Stetson, P. B. (1987). DAOPHOT: A Computer Program for Crowded-Field Stellar Photometry. *PASP*, 99:191.

Stetson, P. B. (1994). The Center of the Core-Cusp Globular Cluster M15: CFHT and HST

Observations, ALLFRAME Reductions. *PASP*, 106:250.

Stetson, P. B. (1996). On the Automatic Determination of Light-Curve Parameters for Cepheid Variables. *PASP*, 108:851.

Sullivan, P. W., Winn, J. N., Berta-Thompson, Z. K., Charbonneau, D., Deming, D., Dressing, C. D., Latham, D. W., Levine, A. M., McCullough, P. R., Morton, T., Ricker, G. R., Vanderspek, R., and Woods, D. (2015). The Transiting Exoplanet Survey Satellite: Simulations of Planet Detections and Astrophysical False Positives. *ApJ*, 809(1):77.

Szabados, L. and Klagyivik, P. (2012). Observational studies of Cepheid amplitudes. II. Metallicity dependence of pulsation amplitudes. *A&A*, 537:A81.

Tody, D. (1986a). The IRAF Data Reduction and Analysis System. In Crawford, D. L., editor, , volume 627 of *Society of Photo-Optical Instrumentation Engineers (SPIE) Conference Series*, page 733.

Tody, D. (1986b). The IRAF Data Reduction and Analysis System. In Crawford, D. L., editor, *Instrumentation in astronomy VI*, volume 627 of *Society of Photo-Optical Instrumentation Engineers (SPIE) Conference Series*, page 733.

Trabucchi, M., Wood, P. R., Montalbán, J., Marigo, P., Pastorelli, G., and Girardi, L. (2017). A New Interpretation of the Period-Luminosity Sequences of Long-period Variables. *ApJ*, 847(2):139.

Trimble, V. (2013). Anybody but Hubble! *arXiv e-prints*, page arXiv:1307.2289.

Turner, D. G. (1996). The Progenitors of Classical Cepheid Variables. , 90:82.

Turner, D. G. (2012). Classical Cepheids After 228 Years of Study. , 40(1):502.

Weinberg, D. H., Mortonson, M. J., Eisenstein, D. J., Hirata, C., Riess, A. G., and Rozo, E. (2013). Observational probes of cosmic acceleration. *Phys. Rep.*, 530(2):87–255.

Whitelock, P. and Feast, M. (2000). Dust enshrouded AGB variables in the LMC. , 71:601–608.

Whitelock, P. A. (2013). Asymptotic giant branch variables as extragalactic distance indicators. In de Grijs, R., editor, *Advancing the Physics of Cosmic Distances*, volume 289 of

IAU Symposium, pages 209–216.

Whitelock, P. A., Feast, M. W., and Van Leeuwen, F. (2008). AGB variables and the Mira period-luminosity relation. *MNRAS*, 386:313–323.

Whitelock, P. A., Feast, M. W., van Loon, J. T., and Zijlstra, A. A. (2003). Obscured asymptotic giant branch variables in the Large Magellanic Cloud and the period-luminosity relation. *MNRAS*, 342(1):86–104.

Whitelock, P. A., Menzies, J. W., Feast, M. W., Nsengiyumva, F., and Matsunaga, N. (2013). The Local Group galaxy NGC 6822 and its asymptotic giant branch stars. *MNRAS*, 428(3):2216–2231.

Wilk, S. R. (1996). Mythological Evidence for Ancient Observations of Variable Stars. , 24(2):129–133.

Wood, P. R. (2000). Variable Red Giants in the LMC: Pulsating Stars and Binaries? , 17(1):18–21.

Wood, P. R. (2015). The pulsation modes, masses and evolution of luminous red giants. *MNRAS*, 448(4):3829–3843.

Wood, P. R., Alcock, C., Allsman, R. A., Alves, D., Axelrod, T. S., Becker, A. C., Bennett, D. P., Cook, K. H., Drake, A. J., Freeman, K. C., Griest, K., King, L. J., Lehner, M. J., Marshall, S. L., Minniti, D., Peterson, B. A., Pratt, M. R., Quinn, P. J., Stubbs, C. W., Sutherland, W., Tomaney, A., Vandehei, T., and Welch, D. L. (1999). MACHO observations of LMC red giants: Mira and semi-regular pulsators, and contact and semi-detached binaries. In Le Bertre, T., Lebre, A., and Waelkens, C., editors, *Asymptotic Giant Branch Stars*, volume 191, page 151.

Xiong, D. R., Deng, L., and Zhang, C. (2018). Turbulent convection and pulsation stability of stars - III. Non-adiabatic oscillations of red giants. *MNRAS*, 480(2):2698–2703.

Yuan, W. (2017). *Period-Luminosity Relations of Cepheid and Mira Variables and Their Application to the Extragalactic Distance Scale*. PhD dissertation, Texas A&M University.

Yuan, W., He, S., Macri, L. M., Long, J., and Huang, J. Z. (2017a). The M33 Synoptic

Stellar Survey. II. Mira Variables. *AJ*, 153(4):170.

Yuan, W., Macri, L. M., He, S., Huang, J. Z., Kanbur, S. M., and Ngeow, C.-C. (2017b). Large Magellanic Cloud Near-infrared Synoptic Survey. V. Period-Luminosity Relations of Miras. *AJ*, 154(4):149.

Yuan, W., Macri, L. M., Javadi, A., Lin, Z., and Huang, J. Z. (2018). Near-infrared Mira Period-Luminosity Relations in M33. *AJ*, 156(3):112.

Zhevakin, S. A. (1959a). On the Calculation of Nonadiabatic Stellar Pulsations by Use of a Discrete Model. , 3:267.

Zhevakin, S. A. (1959b). On the Pulsational Theory of Stellar Variability. VI. (A Unified Interpretation of Various Types of Variability). , 3:913.

Zhevakin, S. A. (1959c). The Pulsational Theory of Stellar Variability. V. (Multilayer Spherical Discrete Model). , 3:389.

APPENDIX A

A.1 Properties of Recovered Yuan et al. (2017a) Miras

Table A.1 shows the properties of the Yuan et al. (2017a) Miras that were recovered as described in Section 2.3. Only 100 rows are shown here; the full table can be provided on request.

Table A.1. Properties of the recovered Yuan et al. (2017a) Miras.

RA [deg]	Dec	P [day]	σ(P)	g [mag]	$\sigma(g)$	r [mag]	$\sigma(r)$	i [mag]	$\sigma(i)$	J [mag]	$\sigma(J)$	H [mag]	$\sigma(H)$	K_S [mag]	$\sigma(K_S)$	Class[a]
23.168823	30.643129	243.26	...	24.408	0.010	23.826	0.007	21.487	0.004	...	...	17.792	0.029	...	...	FU
23.210930	30.698511	243.81	...	...	...	23.221	0.010	21.545	0.009	...	...	18.149	0.026	...	...	FU
23.214310	30.686665	157.49	...	24.280	0.010	22.777	0.008	20.858	0.004	...	...	17.549	0.028	...	...	FO
23.215345	30.631165	345.92	...	...	...	...	...	20.795	0.004	...	...	16.919	0.020	...	...	FU
23.219294	30.694653	263.17	...	...	...	...	...	21.401	0.004	...	...	17.564	0.055	...	...	FU
23.221277	30.587513	616.05	...	...	...	21.119	0.015	18.816	0.004	...	...	15.287	0.020	...	...	FU
23.229029	30.675070	277.31	...	...	...	...	...	21.656	0.005	...	...	17.708	0.035	...	...	FU
23.241301	30.633043	123.42	...	23.502	0.018	22.209	0.012	21.246	0.004	...	...	18.747	0.093	...	...	FU
23.250774	30.680559	221.88	...	24.993	0.026	22.437	0.006	21.641	0.005	...	...	18.297	0.066	...	...	FU
23.257385	30.601858	758.58	...	...	...	...	...	21.701	0.006	...	...	16.023	0.026	...	...	FU
23.270178	30.707214	306.37	...	...	...	21.762	0.008	20.740	0.005	18.699	0.032	17.448	0.031	...	...	FU
23.270407	30.618895	320.40	...	...	...	...	...	22.016	0.015	...	...	17.499	0.034	...	...	FU
23.271086	30.623915	1071.52	...	...	...	...	...	22.295	0.005	18.621	0.051	17.767	0.056	...	...	UN
23.271423	30.531473	172.23	...	...	...	22.964	0.009	21.464	0.012	19.203	0.146	...	...	...	...	FU
23.272795	30.724215	539.55	...	...	...	...	...	21.244	0.005	17.470	0.035	...	...	...	...	FU
23.272890	30.638735	289.39	...	...	...	...	...	21.574	0.005	18.118	0.033	17.654	0.030	...	...	FU
23.275492	30.546745	197.26	...	...	...	22.399	0.006	21.472	0.004	18.306	0.054	...	...	...	...	FU
23.276791	30.709288	408.54	...	...	...	...	...	21.984	0.005	17.860	0.020	...	...	...	...	FU
23.282499	30.640057	799.63	...	...	...	22.165	0.007	19.892	0.005	16.914	0.010	...	...	...	...	FU
23.283573	30.543936	159.00	...	...	...	21.926	0.006	20.880	0.004	19.006	0.024	...	...	18.071	0.053	FU
23.283962	30.597446	257.46	...	...	...	22.209	0.007	20.711	0.004	18.370	0.019	...	...	17.211	0.027	FU
23.284681	30.712015	174.22	...	...	...	22.231	0.005	21.195	0.004	18.616	0.031	...	...	16.974	0.030	FO

Table A.1 (cont'd)

RA [deg]	Dec	P [day]	σ(P)	g [mag]	$\sigma(g)$	r [mag]	$\sigma(r)$	i [mag]	$\sigma(i)$	J [mag]	$\sigma(J)$	H [mag]	$\sigma(H)$	K_S [mag]	$\sigma(K_S)$	Class[a]
23.285614	30.606012	239.12	...	...	...	24.024	0.007	21.592	0.005	18.708	0.029	...	...	17.546	0.041	FU
23.286800	30.673672	285.73	...	...	...	...	...	22.109	0.007	18.300	0.020	...	...	17.066	0.039	FU
23.287325	30.692095	203.53	...	...	...	22.318	0.009	20.928	0.007	18.736	0.026	...	...	17.615	0.043	FU
23.289383	30.566542	162.85	...	...	...	21.698	0.010	20.737	0.008	18.867	0.031	...	...	17.959	0.046	FU
23.290272	30.783861	216.55	...	...	...	23.200	0.012	21.730	0.007	18.583	0.026	...	...	...	...	FU
23.291279	30.656561	135.84	...	...	...	22.833	0.009	21.589	0.005	19.533	0.021	...	...	...	...	FU
23.292292	30.649733	178.42	...	23.348	0.008	23.036	0.008	21.779	0.005	19.149	0.018	...	...	...	...	FU
23.293238	30.656092	170.66	...	...	...	22.652	0.009	21.276	0.009	19.202	0.076	...	...	...	...	FU
23.293501	30.531691	279.53	...	...	...	...	...	21.150	0.010	18.432	0.015	...	...	17.250	0.029	FU
23.293640	30.630022	110.84	...	...	...	22.659	0.008	21.372	0.004	19.029	0.019	...	...	...	...	FO
23.294172	30.686565	306.75	...	...	...	...	...	21.092	0.006	17.993	0.032	...	...	16.846	0.041	FU
23.294195	30.680706	300.25	...	...	...	22.043	0.013	21.371	0.008	18.980	0.017	...	...	17.228	0.031	FU
23.294630	30.641680	366.23	...	...	...	22.201	0.012	21.053	0.004	18.433	0.013	...	...	...	...	UN
23.295912	30.607677	279.53	...	...	...	22.586	0.006	21.665	0.004	...	...	...	...	17.697	0.038	FU
23.296562	30.597889	146.96	...	22.774	0.006	21.609	0.005	20.737	0.004	19.036	0.034	...	...	18.036	0.042	FU
23.298677	30.593361	296.20	...	...	...	23.354	0.010	21.614	0.006	18.319	0.067	...	...	17.157	0.059	FU
23.301098	30.467188	537.03	...	...	...	...	...	21.035	0.004	17.192	0.013	...	...	...	...	FU
23.301823	30.564779	332.72	...	...	...	21.778	0.006	20.898	0.006	18.508	0.019	...	...	17.099	0.039	FU
23.303270	30.608320	288.99	...	...	...	23.663	0.009	21.721	0.004	18.364	0.018	...	...	17.140	0.021	FU
23.303316	30.691870	309.50	...	...	...	...	...	21.682	0.005	18.048	0.014	...	...	16.867	0.020	FU
23.304335	30.580215	151.25	...	...	...	...	...	21.174	0.004	...	...	...	...	18.177	0.039	FU
23.304342	30.521168	195.37	...	...	...	23.542	0.021	21.515	0.004	18.825	0.024	...	...	17.785	0.032	FU

Table A.1 (cont'd)

RA [deg]	Dec	P [day]	σ(P)	g [mag]	$\sigma(g)$	r [mag]	$\sigma(r)$	i [mag]	$\sigma(i)$	J [mag]	$\sigma(J)$	H [mag]	$\sigma(H)$	K_S [mag]	$\sigma(K_S)$	Class[a]
23.304968	30.684505	225.87	...	...	...	22.690	0.008	21.088	0.006	17.481	0.020	...	...	16.063	0.020	FO
23.305534	30.541119	254.69	...	...	...	24.216	0.014	21.470	0.004	18.339	0.018	...	...	17.149	0.016	FU
23.306238	30.710018	247.01	...	23.433	0.022	22.405	0.020	21.287	0.009	18.535	0.021	...	...	17.480	0.026	FU
23.306908	30.630220	200.68	...	...	...	...	...	21.350	0.008	18.008	0.012	...	...	...	...	FU
23.307396	30.660021	306.32	...	...	...	...	...	21.969	0.017	18.417	0.012	...	...	...	...	FU
23.308285	30.470415	193.32	...	...	...	22.125	0.011	21.043	0.004	18.460	0.024	...	...	...	...	FU
23.308912	30.638899	217.46	4.42	...	...	22.115	0.010	21.380	0.006	18.973	0.025	17.840	0.046	...	...	FU
23.311060	30.677229	226.93	...	23.992	0.013	...	...	21.015	0.005	18.600	0.044	...	...	17.488	0.053	FU
23.311411	30.603722	166.68	...	23.595	0.006	22.145	0.006	20.987	0.004	19.083	0.024	18.089	0.037	18.071	0.068	FU
23.313734	30.697510	194.21	...	...	...	...	...	21.363	0.009	18.761	0.039	...	...	17.510	0.052	FU
23.314201	30.792107	171.27	...	23.686	0.009	21.518	0.005	20.874	0.004	18.769	0.035	...	...	...	...	FU
23.314659	30.709637	250.52	...	...	...	22.141	0.005	21.431	0.004	18.968	0.063	...	...	17.190	0.054	FU
23.314806	30.588570	226.29	...	...	...	23.288	0.007	21.213	0.004	18.671	0.021	17.563	0.037	17.566	0.026	FU
23.315958	30.612650	260.93	...	...	...	23.517	0.012	22.120	0.007	19.078	0.046	18.113	0.049	17.665	0.028	FU
23.316244	30.476873	138.46	...	...	...	...	...	21.389	0.007	18.150	0.028	17.232	0.028	...	...	FO
23.316540	30.488371	241.43	...	...	...	22.941	0.012	21.051	0.007	18.711	0.034	...	...	17.547	0.046	FU
23.317278	30.562895	393.51	3.23	...	...	22.496	0.005	21.460	0.004	19.043	0.032	17.666	0.033	16.962	0.026	FU
23.318661	30.848551	298.61	...	...	...	...	...	21.377	0.011	18.069	0.024	17.513	0.021	...	...	FU
23.319258	30.642550	227.78	...	...	...	21.894	0.006	21.225	0.004	19.011	0.021	18.396	0.039	...	...	FU
23.320625	30.827904	219.28	...	23.062	0.006	22.293	0.005	21.013	0.006	18.770	0.019	18.159	0.029	...	...	FU
23.322546	30.360664	289.23	10.04	...	...	...	...	21.303	0.011	...	...	17.423	0.020	...	...	FU
23.323914	30.557257	163.83	...	23.014	0.007	22.556	0.010	21.589	0.005	19.426	0.026	18.657	0.075	18.233	0.061	FU

Table A.1 (cont'd)

RA [deg]	Dec	P [day]	σ(P)	g [mag]	$\sigma(g)$	r [mag]	$\sigma(r)$	i [mag]	$\sigma(i)$	J [mag]	$\sigma(J)$	H [mag]	$\sigma(H)$	K_S [mag]	$\sigma(K_S)$	Class[a]
23.323938	30.782118	242.41	...	...	...	24.514	0.009	21.837	0.005	18.720	0.027	18.107	0.040	17.529	0.029	FU
23.324026	30.584112	476.59	...	...	...	...	...	20.126	0.005	17.258	0.016	16.159	0.020	15.988	0.022	FU
23.325457	30.617702	632.34	3.51	22.973	0.008	21.863	0.006	19.713	0.007	16.696	0.011	15.717	0.011	15.400	0.016	FU
23.325802	30.660009	256.74	3.24	...	...	23.661	0.013	21.529	0.011	18.545	0.013	17.842	0.020	...	...	FU
23.325895	30.631504	191.28	...	23.272	0.005	21.765	0.005	21.188	0.004	19.047	0.034	18.435	0.039	...	...	FU
23.325962	30.533716	294.74	10.15	23.690	0.013	21.972	0.008	21.188	0.006	18.686	0.024	17.927	0.029	17.207	0.028	FU
23.326473	30.640839	199.59	...	23.764	0.022	22.387	0.005	20.943	0.008	18.717	0.013	18.081	0.026	...	...	FU
23.326529	30.724825	249.33	...	...	...	23.275	0.009	21.454	0.008	18.548	0.055	...	...	17.477	0.051	FU
23.326920	30.389994	334.40	...	...	...	23.631	0.010	21.369	0.004	...	...	17.863	0.032	...	...	FU
23.327114	30.475456	291.99	...	...	...	...	...	21.268	0.010	18.114	0.026	17.306	0.027	...	...	FU
23.327793	30.494240	141.65	...	...	...	22.734	0.006	21.113	0.004	18.819	0.035	17.878	0.034	17.615	0.039	FO
23.327822	30.590763	252.12	...	...	...	22.924	0.008	21.292	0.009	18.514	0.019	17.910	0.031	17.281	0.030	FU
23.329123	30.651060	338.76	...	...	...	23.550	0.015	21.362	0.004	18.134	0.014	17.448	0.015	...	...	FU
23.329384	30.508844	207.25	...	...	...	...	...	20.922	0.004	18.634	0.018	...	...	17.643	0.036	FU
23.330309	30.629229	317.90	...	...	...	...	...	21.843	0.006	18.029	0.012	17.358	0.016	...	...	FU
23.330341	30.641035	193.42	...	...	...	...	...	20.959	0.004	18.917	0.026	18.172	0.027	...	...	FU
23.331022	30.452219	156.46	...	...	...	...	...	21.513	0.004	18.174	0.026	17.189	0.030	...	...	FO
23.332806	30.629951	299.95	...	...	...	...	...	21.616	0.012	18.085	0.013	17.609	0.022	...	...	FU
23.333063	30.646305	244.05	...	...	...	23.464	0.007	21.107	0.004	18.627	0.013	17.840	0.020	...	...	FU
23.333111	30.424931	346.75	...	...	...	21.780	0.005	20.907	0.004	...	...	17.507	0.075	...	...	FU
23.335236	30.703390	175.85	...	23.720	0.006	22.240	0.006	20.924	0.004	18.965	0.023	18.207	0.037	17.958	0.046	FU
23.335514	30.639189	492.20	3.54	...	...	...	...	22.583	0.011	18.651	0.027	17.459	0.044	...	...	UN

Table A.1 (cont'd)

RA [deg]	Dec	P [day]	σ(P)	g [mag]	$\sigma(g)$	r [mag]	$\sigma(r)$	i [mag]	$\sigma(i)$	J [mag]	$\sigma(J)$	H [mag]	$\sigma(H)$	K_S [mag]	$\sigma(K_S)$	Class[a]
23.335653	30.522141	347.59	...	...	...	...	...	22.291	0.005	18.277	0.018	...	...	17.131	0.023	FU
23.336349	30.553444	198.88	...	...	...	23.165	0.014	21.877	0.007	18.961	0.024	18.046	0.056	17.850	0.047	FU
23.337198	30.813656	279.40	...	...	...	...	...	21.344	0.004	18.432	0.020	17.591	0.027	...	...	FU
23.338015	30.691135	176.01	...	...	...	22.645	0.007	21.128	0.004	18.933	0.028	18.297	0.046	17.952	0.027	FU
23.338282	30.617926	246.58	4.26	...	...	...	...	21.414	0.009	18.609	0.017	17.906	0.026	17.443	0.026	FU
23.338634	30.638544	238.86	...	...	...	...	...	21.281	0.004	18.576	0.017	17.792	0.021	...	...	FU
23.338848	30.634369	199.53	...	...	...	22.893	0.011	21.789	0.008	18.942	0.021	18.198	0.041	...	...	FU
23.339848	30.664688	143.85	...	23.416	0.018	21.767	0.015	21.046	0.017	19.138	0.049	18.600	0.052	...	...	FU
23.340143	30.542894	306.24	...	...	...	...	...	21.739	0.005	17.993	0.013	17.373	0.022	16.868	0.026	FU
23.340172	30.783434	154.08	...	...	...	21.481	0.005	21.043	0.004	19.093	0.049	18.250	0.060	17.906	0.056	FU
23.341063	30.592283	301.91	22.14	22.080	0.004	21.450	0.007	20.767	0.017	18.161	0.016	17.432	0.026	16.953	0.021	FU
23.341248	30.791618	307.96	...	...	...	21.316	0.005	20.707	0.004	18.933	0.027	17.326	0.021	17.117	0.027	FU

Note. — (a) "FU": fundamental pulsator. "FO": first overtone pulsator. "UN": unknown.

A.2 Properties of Newly Identified M33 Mira Candidates

Table A.2 shows the properties of the Mira candidates that were identified in Section 2.4. Only 100 rows are shown here; the full table can be provided on request.

Table A.2. Properties of the newly identified M33 Mira candidates.

RA [deg]	Dec	P [day]	σ(P)	g [mag]	$\sigma(g)$	r [mag]	$\sigma(r)$	i [mag]	$\sigma(i)$	J [mag]	$\sigma(J)$	H [mag]	$\sigma(H)$	K_S [mag]	$\sigma(K_S)$	Class[a]
23.105476	30.809076	296.18	...	...	...	...	...	22.817	0.020	...	...	17.972	0.050	...	...	FU
23.116587	30.603506	341.51	...	...	...	22.708	0.009	21.308	0.009	...	...	17.745	0.052	...	...	FU
23.134270	30.693346	361.46	...	...	...	22.586	0.013	21.477	0.004	...	...	17.599	0.024	...	...	FU
23.134766	30.715336	286.70	...	23.795	0.011	21.629	0.007	20.856	0.004	...	...	17.648	0.032	...	...	FU
23.135656	30.635357	272.58	3.98	...	...	21.710	0.007	20.903	0.006	...	...	17.579	0.073	...	...	FU
23.135839	30.683971	330.89	22.48	...	...	21.709	0.017	20.734	0.013	...	...	17.442	0.030	...	...	FU
23.142738	30.681828	323.79	...	...	...	23.272	0.023	21.271	0.010	...	...	17.668	0.023	...	...	FU
23.145725	30.895027	224.58	...	23.578	0.012	22.603	0.006	21.124	0.004	...	...	17.740	0.113	...	...	FU
23.149216	30.634874	444.71	...	...	...	22.875	0.006	21.318	0.006	...	...	17.317	0.022	...	...	FU
23.151039	30.643393	168.58	9.72	...	...	22.067	0.020	20.926	0.008	...	...	18.242	0.067	...	...	FU
23.152111	30.626614	161.01	...	...	...	...	...	21.957	0.007	...	...	17.397	0.022	...	...	FO
23.152840	30.706413	217.26	...	...	...	23.008	0.010	20.974	0.007	...	...	17.384	0.086	...	...	FU
23.154127	30.575884	238.26	...	...	...	23.077	0.009	21.047	0.004	...	...	17.427	0.025	...	...	FU
23.155603	30.716747	168.89	...	...	...	22.616	0.013	21.168	0.007	...	...	18.137	0.050	...	...	FU
23.157061	30.692720	164.77	...	23.157	0.005	21.786	0.005	21.278	0.004	...	...	18.404	0.063	...	...	FU
23.159189	30.761253	363.08	...	...	...	22.283	0.004	21.114	0.004	...	...	17.605	0.025	...	...	FU
23.161072	30.683147	326.48	2.89	...	...	...	...	21.343	0.008	...	...	17.378	0.023	...	...	FU
23.161234	30.620100	156.63	...	...	...	...	...	21.928	0.007	...	...	18.755	0.139	...	...	FU
23.161755	30.655785	286.61	...	...	...	22.173	0.010	21.214	0.008	...	...	17.888	0.030	...	...	FU
23.164215	30.580296	308.98	...	...	...	23.150	0.007	21.048	0.004	...	...	16.993	0.021	...	...	FU
23.165257	30.591999	520.93	...	...	...	22.216	0.005	20.839	0.004	...	...	17.136	0.089	...	...	FU
23.166271	30.647148	270.72	...	...	...	23.035	0.008	22.138	0.005	...	...	18.211	0.051	...	...	FU

Table A.2 (cont'd)

RA [deg]	Dec	P [day]	σ(P)	g [mag]	$\sigma(g)$	r [mag]	$\sigma(r)$	i [mag]	$\sigma(i)$	J [mag]	$\sigma(J)$	H [mag]	$\sigma(H)$	K_S [mag]	$\sigma(K_S)$	Class[a]
23.167461	30.655973	244.06	...	...	...	...	...	21.204	0.004	...	...	17.520	0.021	...	...	FU
23.168055	30.778419	142.00	...	23.330	0.005	22.111	0.005	21.078	0.006	...	...	18.403	0.062	...	...	FU
23.170511	30.676483	302.78	...	...	...	...	...	21.977	0.013	...	...	17.682	0.029	...	...	FU
23.170904	30.632553	234.83	...	...	...	...	...	21.510	0.004	...	...	16.513	0.013	...	...	FO
23.171473	30.673626	178.01	...	...	...	21.932	0.009	20.010	0.009	...	...	16.406	0.012	...	...	FO
23.177704	30.673487	308.75	16.19	...	...	21.797	0.023	20.962	0.013	...	...	17.747	0.084	...	...	FU
23.178934	30.825010	531.17	...	...	...	...	...	21.378	0.005	...	...	16.413	0.012	...	...	FU
23.179823	30.707846	132.86	...	...	...	...	...	22.900	0.013	...	...	18.985	0.213	...	...	FU
23.182446	30.599653	134.92	...	...	...	...	...	21.925	0.008	...	...	18.603	0.049	...	...	FU
23.183191	30.633041	145.48	...	...	...	22.631	0.008	20.869	0.006	...	...	17.358	0.027	...	...	FO
23.183542	30.669952	139.39	...	...	...	...	...	21.008	0.004	...	...	17.335	0.019	...	...	FO
23.183573	30.667723	303.47	...	...	...	22.106	0.006	21.153	0.006	...	...	17.823	0.118	...	...	FU
23.187181	30.781582	215.89	...	...	...	22.618	0.006	20.914	0.004	...	...	17.558	0.023	...	...	FU
23.188379	30.611979	283.66	...	...	...	...	...	21.640	0.004	...	...	17.245	0.018	...	...	FU
23.191626	30.804087	253.86	...	...	...	23.662	0.012	21.236	0.007	...	...	17.519	0.023	...	...	FU
23.192650	30.598125	151.76	...	...	...	21.941	0.006	20.983	0.004	...	...	18.451	0.073	...	...	FU
23.194340	30.815060	227.91	...	...	...	23.126	0.006	20.964	0.004	...	...	17.743	0.023	...	...	FU
23.194559	30.652328	384.94	...	...	...	21.800	0.008	20.811	0.004	...	...	17.339	0.060	...	...	FU
23.195921	30.624527	204.52	...	...	...	22.636	0.008	21.411	0.004	...	...	18.250	0.034	...	...	FU
23.196712	30.831093	369.51	...	...	...	22.284	0.011	20.917	0.010	...	...	17.223	0.020	...	...	FU
23.196812	30.672155	308.36	...	...	...	23.651	0.022	21.253	0.004	...	...	17.309	0.015	...	...	FU
23.198071	30.630030	148.39	...	...	...	22.516	0.006	21.300	0.004	...	...	18.348	0.030	...	...	FU

Table A.2 (cont'd)

RA [deg]	Dec	P [day]	σ(P)	g [mag]	$\sigma(g)$	r [mag]	$\sigma(r)$	i [mag]	$\sigma(i)$	J [mag]	$\sigma(J)$	H [mag]	$\sigma(H)$	K_S [mag]	$\sigma(K_S)$	Class[a]
23.200729	30.845684	333.61	...	...	...	22.611	0.006	21.238	0.006	...	...	17.296	0.022	...	...	FU
23.203114	30.610962	396.25	...	...	...	21.687	0.005	20.762	0.004	...	...	17.479	0.025	...	...	FU
23.203297	30.668604	252.80	...	...	...	...	...	21.964	0.005	...	...	18.297	0.034	...	...	FU
23.204975	30.795135	209.93	...	...	...	22.569	0.008	21.045	0.004	...	...	17.982	0.025	...	...	FU
23.206989	30.615688	190.89	...	22.622	0.005	21.194	0.009	19.530	0.010	...	...	16.256	0.012	...	...	FO
23.207880	30.833960	251.22	...	...	...	23.081	0.011	21.188	0.004	...	...	17.985	0.033	...	...	FU
23.209682	30.684155	149.36	...	...	...	...	...	21.241	0.004	...	...	17.221	0.017	...	...	FO
23.210001	30.582886	286.71	...	...	...	22.617	0.009	20.894	0.006	...	...	17.320	0.027	...	...	FU
23.211493	30.601562	239.82	...	...	...	...	...	23.366	0.011	...	...	17.806	0.031	...	...	FU
23.213240	30.611118	173.34	...	23.459	0.005	22.024	0.005	20.884	0.004	...	...	18.299	0.031	...	...	FU
23.216293	30.656523	145.25	...	...	...	23.406	0.012	21.934	0.005	...	...	18.726	0.058	...	...	FU
23.216900	30.672119	213.20	...	...	...	23.026	0.013	21.308	0.007	...	...	17.114	0.022	...	...	FO
23.218929	30.616386	150.47	...	23.073	0.006	22.049	0.005	21.061	0.004	...	...	18.373	0.030	...	...	FU
23.225769	30.668249	117.45	...	23.201	0.008	21.792	0.005	21.021	0.004	...	...	18.548	0.046	...	...	FO
23.226622	30.623575	291.81	30.30	...	...	23.061	0.017	21.312	0.013	...	...	17.335	0.040	...	...	FU
23.226646	30.844973	208.75	...	23.174	0.009	21.605	0.006	19.609	0.006	...	...	15.937	0.014	...	...	FO
23.227274	30.633194	224.15	...	...	...	...	...	21.507	0.004	...	...	17.662	0.017	...	...	FU
23.227760	30.773397	216.52	...	23.475	0.017	21.819	0.006	21.159	0.006	...	...	18.470	0.089	...	...	FU
23.229542	30.602846	229.14	...	...	...	23.187	0.008	21.106	0.004	...	...	17.456	0.123	...	...	FU
23.231554	30.893587	446.51	...	...	...	...	...	22.253	0.006	...	...	17.217	0.021	...	...	FU
23.232519	30.608002	146.93	...	...	...	23.155	0.010	21.050	0.004	...	...	17.225	0.021	...	...	FO
23.233383	30.643801	331.39	...	...	...	21.711	0.008	20.887	0.008	...	...	17.554	0.018	...	...	FU

Table A.2 (cont'd)

RA [deg]	Dec	P [day]	σ(P)	g [mag]	$\sigma(g)$	r [mag]	$\sigma(r)$	i [mag]	$\sigma(i)$	J [mag]	$\sigma(J)$	H [mag]	$\sigma(H)$	K_S [mag]	$\sigma(K_S)$	Class[a]
23.234322	30.670374	317.24	...	...	...	22.122	0.010	21.192	0.008	...	...	17.784	0.022	...	...	FU
23.234619	30.770432	310.14	...	23.440	0.006	21.597	0.004	20.871	0.004	...	...	17.682	0.032	...	...	FU
23.234875	30.653101	406.80	16.80	...	...	...	...	19.959	0.006	...	...	15.861	0.012	...	...	FU
23.234982	30.579012	138.94	...	...	...	...	...	21.197	0.004	...	...	17.588	0.127	...	...	FO
23.235502	30.588570	311.26	...	...	...	22.312	0.011	21.324	0.011	...	...	17.654	0.106	...	...	FU
23.235518	30.591063	146.62	...	...	...	21.713	0.005	20.991	0.004	...	...	18.542	0.056	...	...	FU
23.244741	30.815519	445.36	...	...	...	22.705	0.006	20.267	0.006	...	...	16.255	0.014	...	...	FU
23.244846	30.685076	331.13	15.72	...	...	21.902	0.012	20.884	0.008	...	...	17.297	0.032	...	...	FU
23.244921	30.676191	277.59	...	...	...	...	...	21.569	0.005	...	...	17.564	0.025	...	...	FU
23.245970	30.791754	217.75	...	...	...	21.735	0.005	20.967	0.004	...	...	18.359	0.043	...	...	FU
23.246042	30.709412	433.90	...	24.200	0.013	21.517	0.004	20.346	0.004	...	...	16.800	0.024	...	...	FU
23.246124	30.895498	211.64	...	21.956	0.006	20.564	0.004	19.189	0.007	...	...	15.874	0.011	...	...	FO
23.247017	30.579840	726.12	...	...	...	...	...	22.583	0.007	...	...	16.417	0.019	...	...	FU
23.248020	30.771650	288.82	...	...	...	21.823	0.010	21.038	0.007	...	...	17.546	0.059	...	...	FU
23.248260	30.881542	142.72	...	23.371	0.006	21.893	0.005	21.022	0.004	...	...	18.310	0.230	...	...	FU
23.250954	30.719206	154.92	...	23.097	0.010	21.783	0.008	20.810	0.004	...	...	18.274	0.044	...	...	FU
23.252567	30.594179	261.60	...	...	...	...	...	21.564	0.011	...	...	17.420	0.022	...	...	FU
23.252577	30.772861	181.17	...	23.247	0.005	22.001	0.005	20.757	0.004	...	...	18.038	0.050	...	...	FU
23.252949	30.676674	211.67	...	...	...	21.959	0.005	21.368	0.004	...	...	18.130	0.049	...	...	FU
23.253187	30.647690	242.57	...	...	...	...	...	21.591	0.004	...	...	17.639	0.048	...	...	FU
23.253222	30.719379	176.44	...	23.967	0.008	22.554	0.006	21.249	0.004	...	...	18.359	0.105	...	...	FU
23.254023	30.699602	142.36	...	...	...	...	...	22.126	0.009	...	...	18.709	0.106	...	...	FU

Table A.2 (cont'd)

RA [deg]	Dec	P [day]	σ(P)	g [mag]	$\sigma(g)$	r [mag]	$\sigma(r)$	i [mag]	$\sigma(i)$	J [mag]	$\sigma(J)$	H [mag]	$\sigma(H)$	K_S [mag]	$\sigma(K_S)$	Class[a]
23.254364	30.621805	322.30	...	...	...	...	...	21.381	0.004	...	...	17.449	0.062	...	...	FU
23.256205	30.783485	202.09	...	...	...	22.173	0.007	20.957	0.004	...	...	17.952	0.104	...	...	FU
23.256912	30.773266	569.18	...	...	...	...	...	22.005	0.007	...	...	17.007	0.016	...	...	FU
23.257402	30.685120	377.79	37.88	...	...	22.460	0.009	21.327	0.012	...	...	17.349	0.023	...	...	FU
23.258057	30.773195	337.38	...	...	...	21.848	0.008	20.803	0.004	...	...	17.189	0.060	...	...	FU
23.258152	30.696062	147.80	...	23.917	0.009	22.467	0.006	21.281	0.007	...	...	18.456	0.088	...	...	FU
23.258947	30.888231	206.32	...	...	...	23.245	0.012	21.869	0.004	...	...	17.169	0.017	...	...	FO
23.261545	30.672253	153.93	...	...	...	23.530	0.011	20.940	0.004	...	...	17.200	0.029	...	...	FO
23.262047	30.766426	222.59	...	23.412	0.009	22.288	0.006	21.571	0.006	...	...	18.226	0.042	...	...	FU
23.262943	30.709087	221.06	...	...	...	24.118	0.034	22.472	0.007	...	...	18.070	0.041	...	...	FU
23.263750	30.679379	407.74	...	...	...	...	...	21.245	0.007	...	...	17.455	0.024	...	...	FU
23.264431	30.693350	408.17	5.53	...	...	21.723	0.007	20.696	0.006	17.783	0.034	16.657	0.033	...	...	FU

Note. — (a) "FU": fundamental pulsator. "FO": first overtone pulsator.

A.3 Milky Way Cepheid Photometry

The complete version of Table 3.3 follows below. For more details, see Section 3.3.

Table A.3. Milky Way Cepheid Photometry

Name	MJD[a]	Phase[b]	H [mag][c]
AP Sgr	8985.4918	0.529	5.024
AP Sgr	8985.4978	0.531	5.019
AP Sgr	8987.4525	0.917	5.090
AP Sgr	8987.4535	0.917	5.081
AP Sgr	8989.5118	0.324	4.942
AP Sgr	8989.5128	0.324	4.958
AP Sgr	8991.4788	0.713	5.131
AP Sgr	8991.4796	0.713	5.151
AP Sgr	8994.4853	0.307	4.943
AP Sgr	8994.4861	0.308	4.953
AP Sgr	9003.4870	0.087	4.946
AP Sgr	9003.4878	0.087	4.947
AP Sgr	9005.4106	0.468	4.985
AP Sgr	9005.4114	0.468	4.993
AP Sgr	9008.4852	0.075	4.978
AP Sgr	9008.4860	0.076	4.934
AP Sgr	9010.4345	0.461	4.971
AP Sgr	9010.4353	0.461	4.980
AP Sgr	9012.4559	0.861	5.129
AP Sgr	9012.4567	0.861	5.162
AP Sgr	9014.4878	0.262	4.945
AP Sgr	9014.4886	0.262	4.936
AP Sgr	9018.5542	0.066	5.026
AP Sgr	9018.5551	0.066	5.034
AP Sgr	9025.3964	0.419	4.963
AP Sgr	9027.4546	0.826	5.166

Table A.3 (cont'd)

Name	MJD[a]	Phase[b]	H [mag][c]
AP Sgr	9027.4555	0.826	5.180
AP Sgr	9029.3637	0.203	4.948
AP Sgr	9029.3645	0.203	4.950
BF Oph	8985.4344	0.197	5.228
BF Oph	8987.4142	0.683	5.379
BF Oph	8987.4150	0.684	5.370
BF Oph	8989.4809	0.192	5.197
BF Oph	8989.4827	0.192	5.200
BF Oph	8991.4752	0.682	5.441
BF Oph	8991.4761	0.682	5.374
BF Oph	9003.4846	0.634	5.380
BF Oph	9003.4854	0.634	5.340
BF Oph	9008.4826	0.863	5.336
BF Oph	9008.4835	0.863	5.340
BF Oph	9010.4323	0.342	5.276
BF Oph	9010.4331	0.343	5.237
BF Oph	9012.4534	0.839	5.422
BF Oph	9012.4542	0.839	5.365
BF Oph	9014.4854	0.339	5.282
BF Oph	9014.4863	0.339	5.222
BF Oph	9025.3988	0.022	5.217
BF Oph	9025.3996	0.022	5.215
BF Oph	9027.4567	0.528	5.297
BF Oph	9027.4575	0.528	5.278
BF Oph	9029.3610	0.996	5.237
BF Oph	9029.3621	0.996	5.232

Table A.3 (cont'd)

Name	MJD[a]	Phase[b]	H [mag][c]
RV Sco	8985.4264	0.516	4.858
RV Sco	8985.4311	0.517	4.827
RV Sco	8987.4163	0.845	4.949
RV Sco	8987.4172	0.845	4.940
RV Sco	8989.4766	0.184	4.754
RV Sco	8991.4731	0.514	4.827
RV Sco	8991.4739	0.514	4.811
RV Sco	8994.4507	0.005	4.794
RV Sco	8994.4516	0.005	4.802
RV Sco	9003.4822	0.495	4.817
RV Sco	9003.4830	0.495	4.794
RV Sco	9010.4304	0.641	4.914
RV Sco	9010.4312	0.642	4.886
RV Sco	9012.4506	0.975	4.854
RV Sco	9012.4514	0.975	4.804
RV Sco	9014.4832	0.310	4.752
RV Sco	9014.4841	0.310	4.755
RV Sco	9025.3944	0.110	4.778
RV Sco	9025.3952	0.110	4.768
RV Sco	9028.3677	0.601	4.890
RV Sco	9028.3685	0.601	4.876
RX Cam	9062.5855	0.665	4.941
RX Cam	9062.5864	0.665	4.967
RX Cam	9064.6361	0.924	4.874
RX Cam	9064.6369	0.924	4.896
RX Cam	9073.6074	0.058	4.815

Table A.3 (cont'd)

Name	MJD[a]	Phase[b]	H [mag][c]
RX Cam	9073.6082	0.058	4.877
RX Cam	9075.5526	0.303	4.768
RX Cam	9075.5535	0.304	4.759
RX Cam	9101.6286	0.599	4.919
RX Cam	9101.6294	0.599	4.929
RX Cam	9104.6268	0.978	4.825
RX Cam	9104.6276	0.978	4.875
RX Cam	9107.5893	0.352	4.834
RX Cam	9107.5901	0.353	4.853
RX Cam	9109.5204	0.597	4.904
RX Cam	9109.5216	0.597	4.866
RX Cam	9112.6027	0.986	4.826
RX Cam	9112.6036	0.986	4.834
RX Cam	9115.5516	0.359	4.729
RX Cam	9115.5526	0.359	4.862
RX Cam	9117.5566	0.612	4.877
RX Cam	9117.5574	0.612	4.928
RX Cam	9119.5352	0.862	4.957
RX Cam	9119.5361	0.862	4.947
RX Cam	9121.5263	0.114	4.805
RX Cam	9121.5271	0.114	4.896
RX Cam	9125.4832	0.614	4.846
RX Cam	9125.4841	0.614	4.831
RX Cam	9128.6297	0.012	4.804
RX Cam	9128.6305	0.012	4.870
RX Cam	9131.5459	0.380	4.835

Table A.3 (cont'd)

Name	MJD[a]	Phase[b]	H [mag][c]
RX Cam	9131.5467	0.380	4.883
RX Cam	9134.5179	0.756	4.975
RX Cam	9134.5187	0.756	4.967
RX Cam	9141.4003	0.626	4.892
RX Cam	9141.4013	0.626	4.861
RX Cam	9144.4167	0.007	4.787
RX Cam	9144.4176	0.007	4.848
RX Cam	9153.4228	0.145	4.785
RX Cam	9153.4244	0.145	4.812
SS Sct	9038.4188	0.805	6.023
SS Sct	9038.4197	0.806	6.008
SS Sct	9040.3778	0.339	5.847
SS Sct	9040.3786	0.339	5.840
SS Sct	9044.5041	0.463	5.892
SS Sct	9044.5053	0.463	5.875
SS Sct	9047.5184	0.284	5.854
SS Sct	9047.5193	0.284	5.854
SS Sct	9054.4150	0.162	5.839
SS Sct	9054.4182	0.163	5.832
SS Sct	9058.2555	0.208	5.846
SS Sct	9058.2563	0.209	5.830
SS Sct	9060.2366	0.748	6.016
SS Sct	9060.2374	0.748	6.005
SS Sct	9064.2795	0.849	6.006
SS Sct	9064.2803	0.850	5.994
SS Sct	9067.3441	0.684	5.954

Table A.3 (cont'd)

Name	MJD[a]	Phase[b]	H [mag][c]
SS Sct	9067.3449	0.684	5.950
SS Sct	9067.3460	0.685	5.959
SS Sct	9067.3469	0.685	5.954
SS Sct	9071.3580	0.777	5.997
SS Sct	9071.3589	0.778	5.991
SS Sct	9073.2440	0.291	5.855
SS Sct	9075.2454	0.836	5.999
SS Sct	9075.2462	0.837	5.989
SS Sct	9101.3020	0.934	5.946
SS Sct	9101.3028	0.934	5.938
SS Sct	9105.2155	0.000	5.878
SS Sct	9105.2163	0.000	5.879
SS Sct	9107.2152	0.544	5.915
SS Sct	9107.2160	0.544	5.910
SS Sct	9109.2539	0.100	5.852
SS Sct	9109.2547	0.100	5.837
SS Sct	9113.2593	0.191	5.861
SS Sct	9113.2604	0.191	5.828
SS Sct	9115.3531	0.761	5.997
SS Sct	9115.3548	0.761	5.995
SS Sct	9118.2069	0.538	5.923
SS Sct	9118.2077	0.538	5.902
SS Sct	9120.2077	0.083	5.864
SS Sct	9120.2088	0.083	5.840
TX Cyg	9038.4533	0.221	4.695
TX Cyg	9038.4541	0.221	4.801

Table A.3 (cont'd)

Name	MJD[a]	Phase[b]	H [mag][c]
TX Cyg	9040.4761	0.358	4.700
TX Cyg	9040.4769	0.358	4.811
TX Cyg	9042.5297	0.498	4.798
TX Cyg	9042.5306	0.498	4.900
TX Cyg	9044.5094	0.632	4.868
TX Cyg	9044.5102	0.632	4.875
TX Cyg	9047.5215	0.837	4.985
TX Cyg	9047.5224	0.837	4.949
TX Cyg	9054.4210	0.306	4.697
TX Cyg	9054.4218	0.306	4.818
TX Cyg	9058.4305	0.579	4.827
TX Cyg	9058.4313	0.579	4.855
TX Cyg	9060.3936	0.712	4.967
TX Cyg	9060.3944	0.712	5.000
TX Cyg	9062.5909	0.862	5.023
TX Cyg	9062.5918	0.862	5.021
TX Cyg	9064.4200	0.986	4.822
TX Cyg	9064.4208	0.986	4.875
TX Cyg	9067.3492	0.185	4.711
TX Cyg	9067.3500	0.185	4.703
TX Cyg	9071.4157	0.461	4.743
TX Cyg	9071.4165	0.462	4.827
TX Cyg	9073.2471	0.586	4.833
TX Cyg	9073.2480	0.586	4.920
TX Cyg	9075.2482	0.722	4.997
TX Cyg	9075.2490	0.722	4.968

Table A.3 (cont'd)

Name	MJD[a]	Phase[b]	H [mag][c]
TX Cyg	9101.3059	0.493	4.783
TX Cyg	9101.3067	0.493	4.904
TX Cyg	9103.2795	0.627	4.934
TX Cyg	9103.2804	0.628	4.963
TX Cyg	9105.3153	0.766	5.010
TX Cyg	9105.3162	0.766	5.009
TX Cyg	9107.2198	0.895	5.019
TX Cyg	9107.2206	0.895	5.014
TX Cyg	9109.2472	0.033	4.801
TX Cyg	9109.2481	0.033	4.829
TX Cyg	9109.2492	0.033	4.799
TX Cyg	9109.2500	0.033	4.821
TX Cyg	9113.2640	0.306	4.688
TX Cyg	9113.2653	0.306	4.726
V0386 Cyg	8985.6038	0.915	5.761
V0386 Cyg	8985.6054	0.915	5.743
V0386 Cyg	8989.6276	0.680	5.769
V0386 Cyg	8989.6285	0.680	5.755
V0386 Cyg	8991.6173	0.059	5.609
V0386 Cyg	8991.6182	0.059	5.576
V0386 Cyg	8994.6202	0.630	5.730
V0386 Cyg	8994.6210	0.630	5.729
V0386 Cyg	8999.6043	0.578	5.712
V0386 Cyg	8999.6051	0.578	5.707
V0386 Cyg	9003.6001	0.338	5.601
V0386 Cyg	9003.6010	0.338	5.589

Table A.3 (cont'd)

Name	MJD[a]	Phase[b]	H [mag][c]
V0386 Cyg	9005.5201	0.703	5.788
V0386 Cyg	9005.5209	0.703	5.781
V0386 Cyg	9007.5619	0.091	5.628
V0386 Cyg	9007.5627	0.092	5.609
V0386 Cyg	9010.5753	0.665	5.749
V0386 Cyg	9010.5765	0.665	5.750
V0386 Cyg	9012.5344	0.037	5.616
V0386 Cyg	9012.5352	0.037	5.587
V0386 Cyg	9014.4911	0.409	5.636
V0386 Cyg	9014.4919	0.409	5.613
V0386 Cyg	9017.6264	0.006	5.620
V0386 Cyg	9017.6273	0.006	5.614
V0386 Cyg	9020.5690	0.565	5.690
V0386 Cyg	9020.5698	0.566	5.685
V0386 Cyg	9027.5858	0.900	5.739
V0386 Cyg	9027.5867	0.900	5.739

Note. — (a) JD−2450000.5. (b) based on the periods listed in Table 3.1 and the phase offsets listed in Table 3.2; the overall systematic uncertainty in this parameter for a given Cepheid is provided in the latter table. (c) DIA magnitude + mean 2MASS magnitude from Table 3.1; a statistical uncertainty of 0.027 mag applies to all lines (see §3.3.3).